



**POLITECNICO**  
MILANO 1863

SCUOLA DI INGEGNERIA INDUSTRIALE  
E DELL'INFORMAZIONE

# Simulation and Validation using HIL technique of the control system of a light train powered by hydrogen fuel cells and batteries

TESI DI LAUREA MAGISTRALE IN  
ELECTRICAL ENGINEERING  
INGEGNERIA ELETTRICA

**Author: Francesco Maggiulli**

Student ID: 967673

Advisor: Giovanni Maria Foglia

Co-advisor: Pietro Tricoli, Nursaid Polater

Academic Year: 2021-2022



## Abstract

In today's international context, one of the most important objectives has become the use of environmentally sustainable resources. Locomotion through fossil fuels such as diesel is still present in the railway world. The aim of this thesis is to study and design an electric propulsion system that can replace existing vehicles that cannot access an electrified network. Therefore, a railway route travelled by a diesel train was taken as a sample, and using hydrogen fuel cells and batteries, an innovative propulsion system was developed. These two sources were chosen on the basis of their main property; in fact, combustion cells possess a high energy density compared to batteries, which, conversely, can provide much more power than hydrogen cells. Therefore, in our project they will be used in a complementary manner, and it is interesting to combine them to obtain high-efficiency locomotives that can travel under different conditions.

A study was therefore conducted on a new electrical setup using a three-phase double motor with permanent magnets as the heart of the project. In such a motor, one three-phase winding is powered by the combustion cells, the other winding by the batteries. These two sources transfer power to the motor in a controlled manner via a FOC-type algorithm and a specially designed logic scheme. The main objective of this thesis was to validate the results obtained using the hardware-in-the-loop technique. This technique, hereinafter referred to as HIL, consists of a simulation in which some components are real, and others remain virtual. In this case, the real part is the microcontroller, i.e. the brain that is responsible for deciding how much power comes from the hydrogen combustion cells and how much from the batteries.

Finally, the complete route where the train will be operational has been simulated. Through the imposition of speed limits and operating conditions, it was confirmed that the setup can be real-life.

**Key-words:** Hydrogen Fuel Cells, Batteries, Double Three-Phase Permanent Magnets



## Abstract in italiano

Nel contesto internazionale attuale, uno degli obiettivi più importanti è diventato l'utilizzo di risorse sostenibili a livello ambientale. In particolare, nel mondo ferroviario è ancora tutt'oggi presente la locomozione attraverso combustibili fossili come il Diesel. Ciò che ci si prefigge in questa tesi è lo studio e la progettazione di un sistema di propulsione elettrica che possa sostituire i veicoli già presenti che non possono accedere ad una rete elettrificata. È stato dunque preso come campione una tratta ferroviaria percorsa da un treno a Diesel e attraverso l'utilizzo di celle a combustibile ad idrogeno e batterie è stato possibile sviluppare un sistema innovativo di propulsione. Queste due sorgenti sono state scelte in base alla loro proprietà principale; infatti, le celle a combustione posseggono un'elevata densità energetica rispetto alle batterie che, viceversa, possono fornire molta più potenza rispetto alle celle ad idrogeno. Quindi, nel nostro progetto verranno impiegate in maniera complementare, e risulta interessante combinarle al fine di ottenere locomotori ad alto rendimento che possono viaggiare in condizioni differenti.

È stato condotto uno studio quindi su un nuovo setup elettrico che prevede l'utilizzo di un motore doppio trifase a magneti permanenti che rappresenta il cuore del progetto. In tale motore, un avvolgimento trifase è alimentato dalle celle a combustione, l'altro avvolgimento dalle batterie. Queste due sorgenti trasferiscono potenza al motore in modo controllato, attraverso un algoritmo di tipo FOC ed uno schema logico appositamente studiato. L'obiettivo principe di questa tesi è stato validare, attraverso la tecnica Hardware-in-the-loop, i risultati ottenuti. Tale tecnica, in seguito indicata con HIL, consiste in una simulazione in cui alcune componenti sono reali ed altre rimangono virtuali. In questo caso, la parte reale è il microcontrollore ovvero il cervello che avrà il compito di decidere quanta potenza proviene dalle celle a combustione ad idrogeno e quanta dalle batterie.

In fine, è stato simulato il percorso completo dove il treno potrà essere operativo. Attraverso l'imposizione di limiti di velocità e delle condizioni di funzionamento, è stato confermato che il setup può avere un riscontro reale.

**Parole chiave:** Celle a Combustione ad Idrogeno, Batterie, Doppio Trifase a Magneti Permanenti









# Contents

<b>Abstract</b> .....	<b>i</b>
<b>Abstract in italiano</b> .....	<b>iii</b>
<b>Contents</b> .....	<b>1</b>
<b>1 Preface and Aims</b> .....	<b>5</b>
1.1. Project.....	5
1.2. Comparison between PC and HIL simulation .....	6
1.3. Path explanation.....	8
<b>2 Introduction</b> .....	<b>11</b>
2.1. General Electric Scheme .....	11
2.2. Fuel Cell and Battery explanation.....	17
2.3. Motor and Its Equations .....	21
2.4. Scheme of control: Field Oriented Control (FOC) .....	30
2.5. PID regulator.....	35
2.6. Microcontroller and Inverter .....	40
2.6.1. PWM and Inverter.....	40
2.6.2. ADC.....	44
2.6.3. Sample Time and Execution Time .....	45
2.6.4. Z-domain and Discretize domain .....	46
<b>3 Open Loop Approach</b> .....	<b>51</b>
3.1. Single Leg Inverter and RL load.....	51
3.2. Three-phase inverter with RL load .....	58
3.3. Three-phase inverter with Induction Motor.....	63
<b>4 PMSM and FOC implementation</b> .....	<b>69</b>
4.1. Three-phase PMSM: Matching Angle .....	69
4.2. Three-phase PMSM: Current Control .....	70
4.3. Double Three-Phase PMSM: Current Control .....	74
4.4. DTPMSM: Speed Control.....	79
<b>5 Power Sharing</b> .....	<b>85</b>
5.1. Introduction and Aims .....	85

5.2.	Power Supply Wiring Diagram.....	87
5.3.	Logical Scheme Diagram Tests.....	89
5.3.1.	Test1(T1) .....	92
5.3.2.	Test 2(T2) .....	94
5.3.3.	Test 3(T3) .....	96
<b>6</b>	<b>Experimental Data of the Complete Setup.....</b>	<b>99</b>
6.1.	Gradient Contribution .....	99
6.2.	PI Tuning .....	100
6.3.	Explanation of the Experimental Data .....	100
<b>7</b>	<b>Conclusion and Future Updates .....</b>	<b>107</b>
	<b>Bibliography .....</b>	<b>111</b>
<b>A</b>	<b>Appendix A.....</b>	<b>113</b>
	<b>List of Figures .....</b>	<b>115</b>
	<b>List of Tables.....</b>	<b>119</b>
	<b>List of Abbreviation .....</b>	<b>121</b>
	<b>List of Algorithms.....</b>	<b>121</b>
	<b>Acknowledgements.....</b>	<b>123</b>





# 1 Preface and Aims

This project was born from the idea of Pietro Tricoli, reader in power electronics and my supervisor at the University of Birmingham, from March to June 2022. I worked alongside Nursaid Polater, PhD student. They allowed and supported me to develop a big part of the project they were working on.

## 1.1. Project

The government's new aim is to reduce the rate of pollution and its environmental problems as much as possible. One of these critical problems is related to the decarbonization of the railway. It's unfair that there are a lot of tracks that work with diesel rolling stock, while all over the world, several nations are trying to move forward to a total electrification system for mobility and massive transportation. Due to the high infrastructure costs, it will be tough that every single track will be converted in electrical system. The researchers are focused on finding a new innovative way to feed the rolling stocks mixing the use of Hydrogen and an electrification part that could be a fixed infrastructure or a battery system.

Moreover, the motors for the traction system should be reviewed to find a more efficient way to replace diesel rolling stocks. In particular, the best solution is related to the Permanent Magnet Synchronous Motor (PMSM) with multi-phase winding system instead the DC motors [1].

The idea is to study an innovative way to feed a train taking care of the previous needs. My colleague Nursaid's project deals with the utilization of a dual-three phase PMSM that allows to manage double sources in a new configuration avoiding the DC-DC converter. Whereas, as far as my work concerned, it deals with the validation of his results using the Hardware-in-the-Loop (HIL) technique. This technique implies that in the whole simulation system, some components are no more simulated, but they are replaced by the real components (hardware). In this thesis, the control system is the real, hardware component, whereas all the rest (power supply, drive, motors) is simulated by "Typhoon HIL" simulator described in the following section.

In the next chapters will be discussed about the step did to develop all the main parts such as inverters, filters and algorithms. What will be focused on detail is related to the translation of the control on a real external hardware reaching the main goal of the report.

## 1.2. Comparison between PC and HIL simulation

In order to validate the way hydrogen is used with the new configuration, it is important to simulate the layout and acquire experimental data from it (currents, voltages, speeds) to confirm the feasibility of the design and also to identify any critical issues that may arise as a result. In this part, the main differences between a PC-only simulation and a HIL simulation will be briefly analysed.

A simulator is a device (with its own software attached) which permits to provide a realistic imitation of a system control. This system will be converted in mathematical equations and will be solved to get the information required.

The University of Birmingham gave me the opportunity to use a Real Time simulator: the company that provide it, is "Typhoon HIL". They built a dedicated hardware and pc software that permits to run any simulation in a real time. This characteristic means that one second in real life corresponds to one second for the simulator. Practically speaking, the powerful hardware makes possible to calculate thousands values each second, and for this reason it is a complex and costly device. The Figure 1.2-1 shows the one used in this report.



Figure 1.2-1 : Typhoon HIL dedicated hardware

In this way we could visualize and analyse the data not only after the simulation but also during the process. Therefore, it's possible to change parameters, modify some controller options and adjust the wanted behaviour. Since it is just simulation, it can be done repeatedly allowing to create different scenarios, with different conditions, without the real part and becoming cheaper for the preliminary study of a setup.

That type of approach is useful for the utilization of the HIL technique in which we can connect a microcontroller to the dedicated hardware by using both digital and analogic IO (Actually also UART, CAN and other peripheral could be used but they will not in this report).

Hardware-In-the-Loop refers to the technique for testing and validating the electronic control unit that is to be inserted into a real working system and then become an embedded system. Using PC software specifically created for dedicated hardware, we

can simulate electrical parts such as motors, inverters, ideal and non-ideal sources, sensors, actuators and more. In the electronic control unit, which will be a microcontroller capable of reading and sending signals, the appropriate algorithms will be inserted to manage all these parts, creating a sequence of actions to be performed in order to have full control over the project. In fact, this algorithm represents the brain of an embedded system that could be used in a real physical application [2].

Typhoon HIL and Texas Instruments collaborated to create an interface board suitable for an external microcontroller connected with the simulator [3] such as the one used in the Figure 1.2-2. The possibility to use a multiple board suitable for the control of enlarge projects can clearly be seen

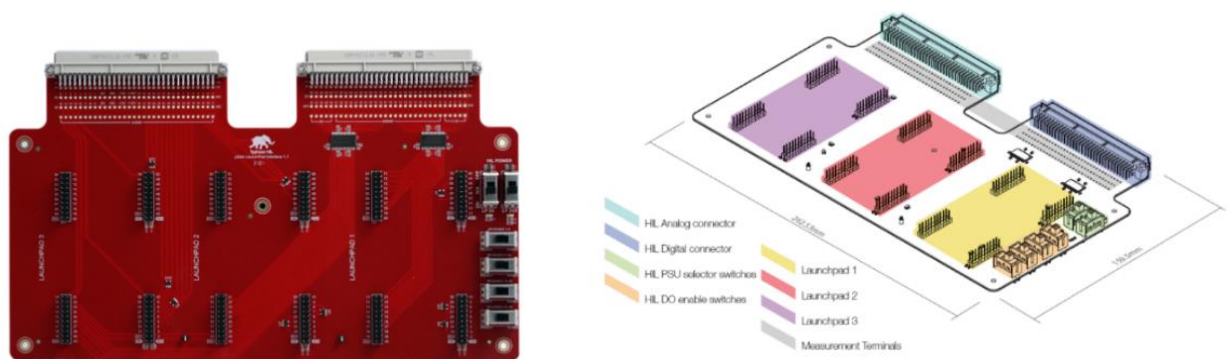


Figure 1.2-2 : HIL TI uGrid Launchpad Interface [2]

The microcontroller will be attached to his spot on the board (the one used is only the yellow one). With this configuration a lot of external inputs/outputs are connected to the simulation on the PC to share PWM and ADC signals.

Since the microcontroller is a real physical device, it works with a computational speed that we could decide, but in real time as Typhoon HIL simulator.

Both could exchange signal data with one another and how this happen will be discussed in the Section 2.6

In conclusion, the powerful difference between only PC (ie Simulink) and HIL simulator (Typhoon HIL) is the capability to run in real time mode allowing to interface a real embedded system and a virtual hardware that replicate a possible physical



Figure 1.2-3 : Complete Setup

hardware that replicate a possible physical

hardware configuration. Moreover, it also eliminates the need to buy a new physical part and gives the possibility of creating complex setups.

### 1.3. Path explanation

The study performed started analysing an existing situation. To sum up, the path will be implemented in the real time simulator. The path that will be considered is St Ives Bay Line Railway, South West of UK. So far, this path is covered by a diesel train, Class150. As far as the path specifications are concerned, the Single Train Simulator (STS), developed by the Birmingham Centre of Rai Research and Education (BCRRE), is used to calculate the energy, traction, curves, braking and more according to the vehicle.

The Class150 has 4 couches, and each has a 213[kW] diesel engine (DE). So, eight electrical motors of 110[kW] each could replace the DE to have the same acceleration required.

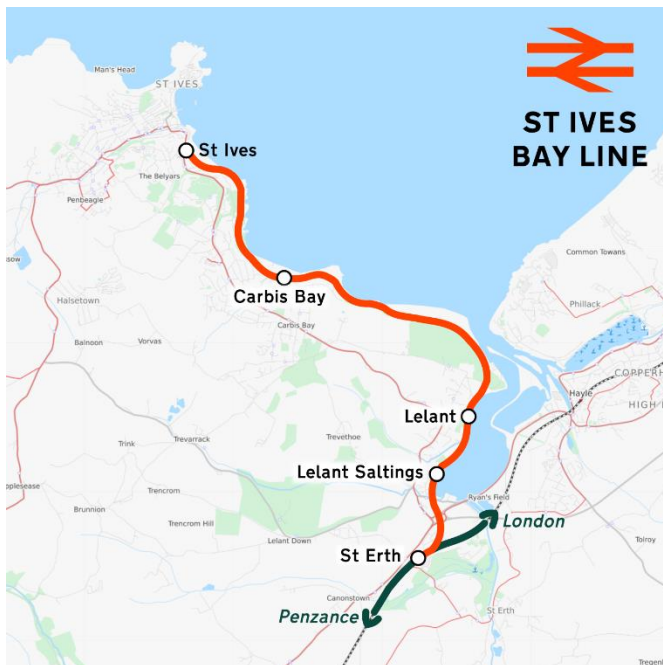


Figure 1.3-1 : St Ives Bay Line branch [4]

There are various points to focus on. The first one is the length, which is equal to 6.7[km]. It contains five stations spaced as shown in the Table 1.3-1. The rolling stock will start from the St Erth station, stops at each of them and return passing again through the five stations. This means that the actual path is the double, 13.4[km]. It is fundamental to consider both the directions since they have different working conditions. In this way, it seems that there's no coming back, but the train continue his run without interruptions up to 24 trips per day with a total distance travelled of 321.6km. The refuel station is not

along the path, so it need to come back every day to his deposit. This part is not considered in the report. The difference between going and coming back is mainly referred to the slope of the railway that impacts a lot on the traction resistance force that the engine should contrast through working under operating conditions.

What will be explained within the report is how to reach this goal, how much precision is possible to get using an embedded system instead of the only PC simulation and will be discussed about the enhancements needed to sort all the problems that comes out.



Table 1.3-1 : Position of stations of St. Ives Bay Line

<b>Station</b>	<b>Distance from begin [m]</b>
<b>St. Erth</b>	0
<b>Lelant Salting</b>	1020
<b>Lelant</b>	1731
<b>Carbis Bay</b>	4820
<b>St. Ives</b>	6700



## 2 Introduction

In this chapter, the main parts of the project will be explained, taking into account all the features necessary to have the most detailed information to understand the work carried out in the following chapters. By going through the circuit diagram, observing the sources and going through the entire project, it will be possible to grasp the behaviour of each individual part.

### 2.1. General Electric Scheme

The Electric Scheme is the main part we need to analyse to really understand what the purpose of the report is. We are referring to rolling stocks that are currently working with a self-propelled such as the diesel one.

As seen before, the project starts from the necessity of decarbonisation of the railway system and to reach this aim it was chosen to substitute the Diesel traction with an alternative one. We will refer to a combination of Hydrogen with an electric system such as batteries. Combining these two elements, good results will be achieved with regard to pollution and a good efficiency will be obtained. In fact, the traditional diesel-engine has problems to achieve a starting constant tractive effort at the beginning and a constant power at higher speeds. Therefore, for diesel systems is required a transmission between motor and wheels reducing the efficiency.

The scheme that will be utilized is completely different from the Diesel one. Now, we are going to look of this latter to understand the parts that could cause problems and see if we could sort them.

Let's look inside the Figure 2.1-1 [5]. The first element is obviously the DE(Diesel-Engine) useful to supply the three-phase generator. The torque generated by the DE depends on the pressure of the fuel injected and therefore the amount of this latter. In this way it is possible to adjust the torque. But neither can the engine be started under load, nor can it reverse the rotation, so a transmission part is needed. This element could increase or decrease the torque at the shaft of the electric three-phase generator.

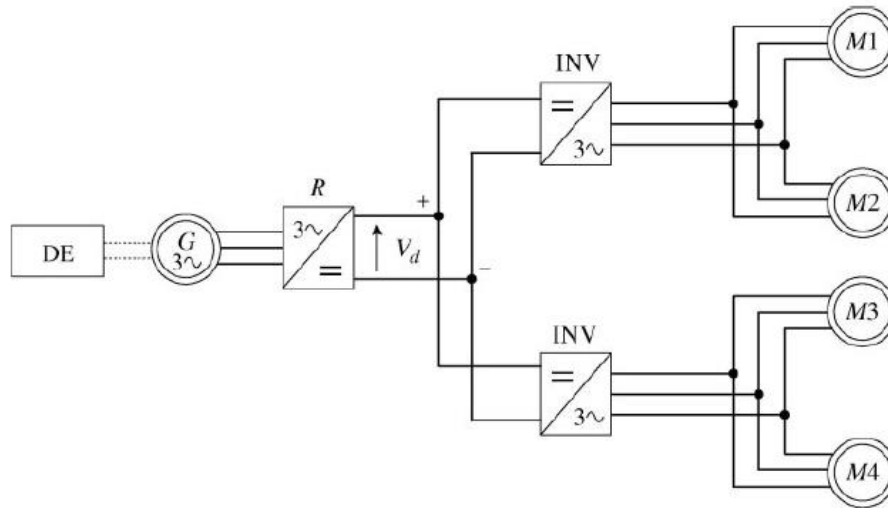


Figure 2.1-1 : Self-Propelled Scheme for AC traction System [5]

The average efficiency of the DE at a specific fuel consumption  $C_s = 0.20 - 0.21 \left[ \frac{kg}{kWh} \right]$  is  $\eta_d \approx 0.41 - 0.43$  [5].

Another interesting part is the AC-DC converter and immediately afterwards the DC-AC inverter which will power the traction motors. This diagram contains only one DE, so it is easy to insert a DC link that executes and connects two different parts. This is extremely useful when thinking about motor control. It is possible to manage their operation independently.

The purpose of a DC link is to connect more diverse sources together with different load as also other systems need to be supplied, for example the air conditioning system, lighting, or auxiliary services. Thus, Self-Propelled Vehicles most likely have more than one DE.

The general configuration of a self-propelled vehicle could be such as the Figure 2.1-2.

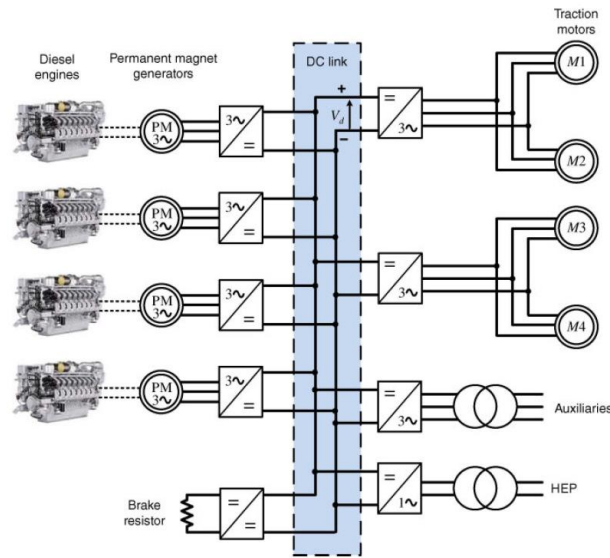


Figure 2.1-2 : Basic diagram of a multi engine diesel locomotive [5]

The DC link becomes more complex and needs more attention. Moreover, is clearly visible that one block represents the brake resistor placed because the energy during the braking cannot be recovered and will be lost.

But we do not want to use diesel engine. We are going to discuss a new solution to perform the same results but using sustainable sources. The one that could be a good substitute of diesel is the Hydrogen Fuel Cell (FC) that will be analysed on detail in the section 2.2.

For now, let's consider the Hydrogen Fuel Cell as a DC electric source which could be able to supply a load using hydrogen as fuel.

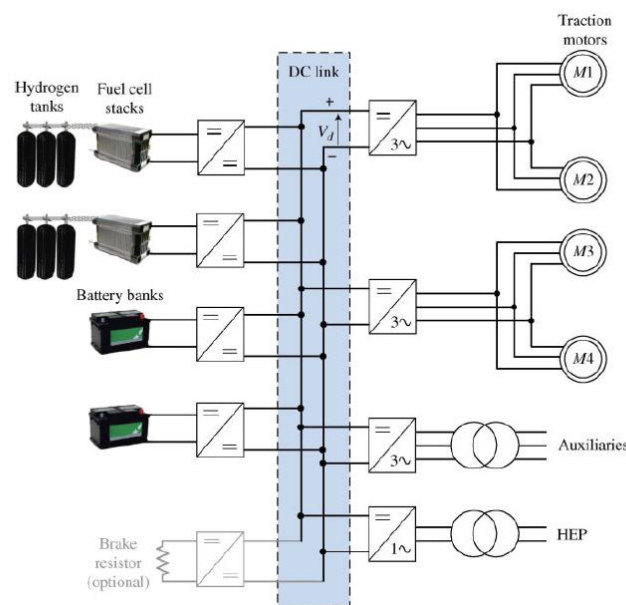


Figure 2.1-3 : Diagram of Fuel Cell locomotive [5]

The right part of the schematic after the DC link is the same as DE system. The substantial difference is how to supply to the DC link. Actually, the FC are non-ideal DC sources, so they do not have a constant voltage at their terminals. They have a low-voltage output characteristic. It becomes relevant to use the DC-DC step-up converter, devices dedicated to fix the voltage constant and equal to all the other components at the interface of the DC link.

Moreover, the batteries must be added because the FCs are not able to provide as much power needed during the acceleration period. They are also useful to store energy during the braking phase increasing the efficiency and avoiding the brake resistor. Following this logic, the FC will be sized to provide only the nominal power at rated speed.

The standard configuration such as in Figure 2.1-3 or [6] would be bulky, inefficient, and costly. Therefore, a boost-inverter is introduced to combine the DC-DC step-up function with the DC-AC of the inverter like in Figure 2.1-4[1].

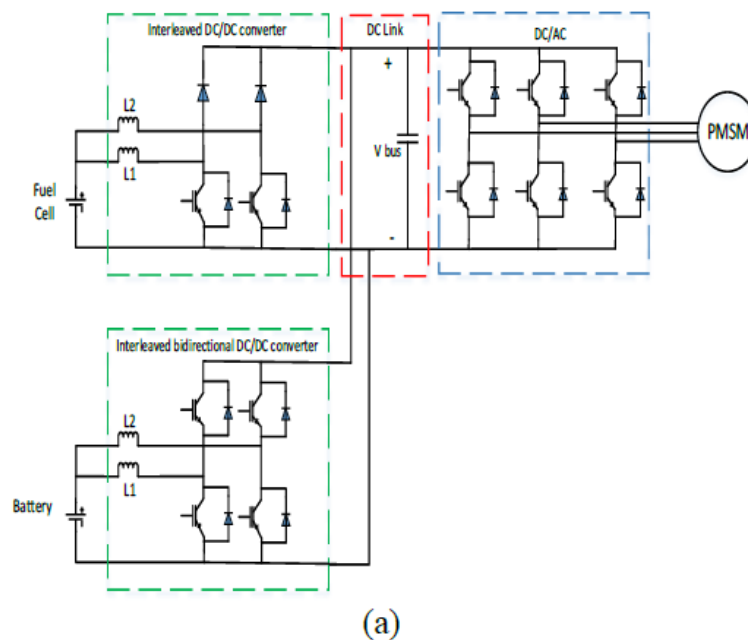


Figure 2.1-4 : Standard configuration of a Hydrogen and Battery Supplied Train [1]

The lower DC-DC attached to the battery must be bidirectional because it allows the battery to be charged and discharged. A good choice will be a Bidirectional Interleaved Converter that is suitable for high-power battery application. Moreover, since it has a higher power with a less per unit volume and weight, it could have a better thermal capability with a reduction of current stresses in the semiconductors. For this reason, by using Interleaving Methods become more efficient for traction vehicles. In this configuration a DC link and an inverter to control the traction motor are necessary.

Instead, the proposed new configuration is different. The target is to reduce weight and size as much as possible without decreasing performance and efficiency.

This preliminary study was carried out by Nursaid Polater [1] from the idea suggested by Pietro Tricoli and we will show the result obtained.

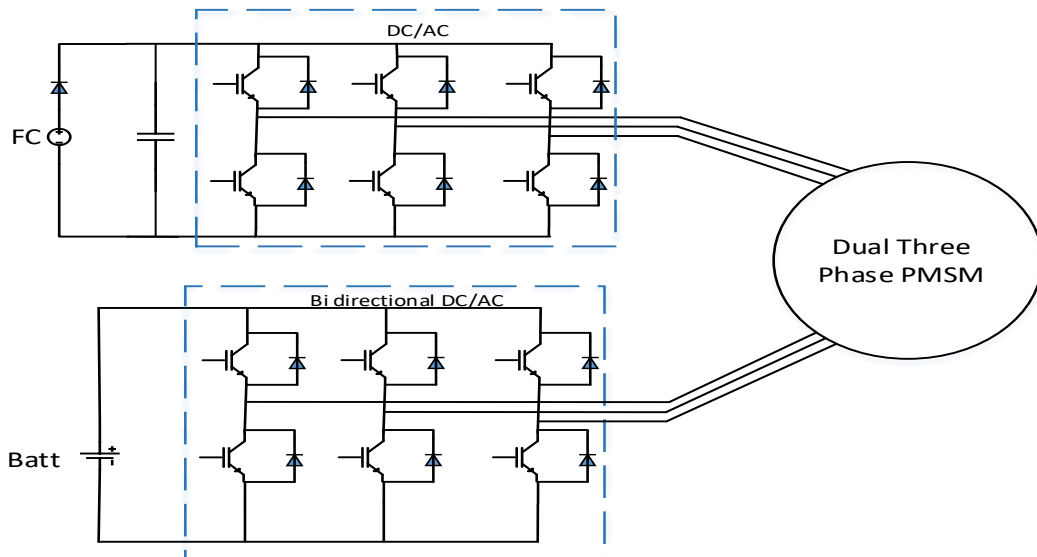


Figure 2.1-5 : New configuration proposed for traction vehicles using hydrogen FC and batteries

The innovative configuration is completely different. The first hypothesis is the use of a Dual-Three Phase Permanent Magnet Synchronous Machine (DTPMSM). As will be clarified in the Section 2.3 , this assumption permits to divide and separate electrically two different circuits and use the effect of each one for the motor traction. Indeed, the motor could be supplied from both the sources independently. Following this suggestion, we could remove both the DC link and the DC converter since it is no longer necessary to fix a common and constant voltage.

Considering our aim to reduce size and weight, we will present the results obtained in the study [1]. With reference to figure 2.1-4 and 2.1-5, it is possible to distinguish:

Table 2.1-1 : Comparison between the two configurations [1]

Component	Standard Configuration	Proposed Configuration
N° of IGBT	12	12
IGBT Rating [kVA]	1042.8	530.4
IGBT Volume[dm <sup>3</sup> ]	1128.5	321
IGBT Weight[kg]	1.819	0.759
IGBT Cost[£]	1433.8	810.98
N° of Diodes	0	1
Diode Rating [kVA]	0	256
Diode Volume[dm <sup>3</sup> ]	0	0.032

Diode Weight[ <i>kg</i> ]	0	0.25
Diode Cost[£]	0	29.71
N° of Capacitor	1	2
Capacitor Energy[ <i>J</i> ]	6.33	3.82
Capacitor Volume [ <i>dm</i> <sup>3</sup> ]	0.088	0.156
Capacitor Weight[ <i>kg</i> ]	0.125	0.044
Capacitor Cost[£]	15.79	13.28
N° of Inductor	4	0
Inductor Energy[ <i>J</i> ]	9.76	0
Inductor Volume[ <i>dm</i> <sup>3</sup> ]	21.24	0
Inductor Weight[ <i>kg</i> ]	94.29	0
Inductor Cost[£]	4920	0

Putting the above values together, the total parameters result as follows:

Table 2.1-2 : Total Parameters of the comparison from Standard and Proposed Configurations

Parameters	Standard Configuration	Proposed Configuration
Total Volume[ <i>dm</i> <sup>3</sup> ]	1.15e3	321
Total Weight[ <i>kg</i> ]	96.23	1.05
Total Energy[ <i>J</i> ]	16.09	3.83
Total Power[ <i>kVA</i> ]	1042.8	786.4
Total Cost [£]	6369.59	853.97

The conclusions of this study are fascinating. The proposed new configuration minimizes the volume and weight occupied by the electrical part and is thus able to improve performance.

It is clearly a valid solution to be studied, but it needs to be validated and this will be done in this report using the HIL technique. Some questions arise concerning the implementation of this project, they will be reported:

- Is it possible to change the standard configuration and remove the DC-DC converter?
- Without the DC-DC converter, could we manage multiple sources for the feeding of a rolling stock?
- Could we translate the control on a real external hardware and get proper results?



## 2.2. Fuel Cell and Battery explanation

Since the two sources for the new configuration are not ideal and mainly the first one has some points to be shown, it is fundamental to focus on them to understand how they work, how could the inverter be supplied and what are the major useful characteristics we need to consider during the simulations.

Remembering that our purpose is to decrease size and weight and substitute trains in tracks covered by DE rolling stocks with a sustainable fuel, is important to focus on different technologies available for the energy storing.

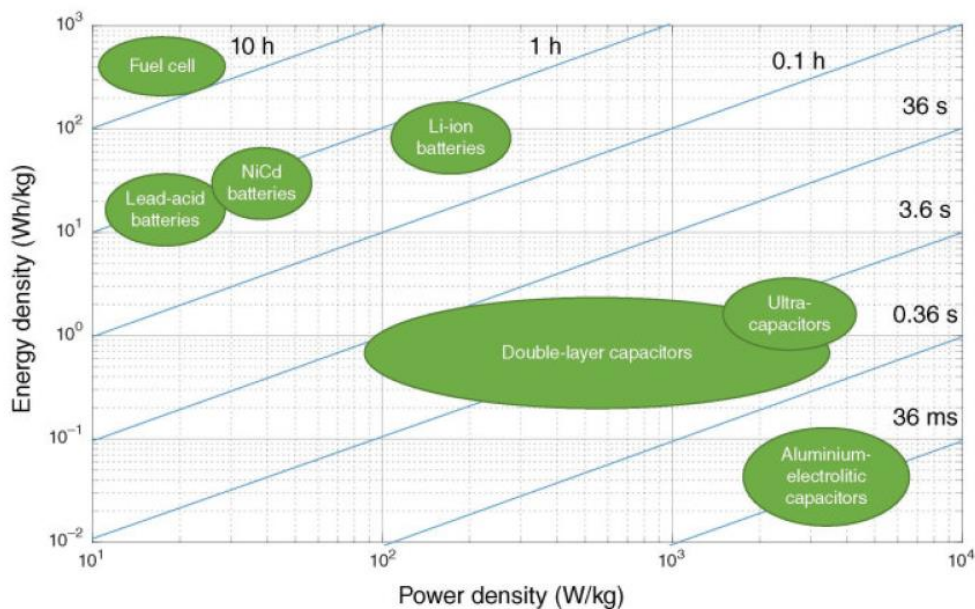


Figure 2.2-1 : Ragone chart for different storage technologies [5]

This chart represents the power and energy density, and it is important to understand why Hydrogen Fuel Cell are a good choice. These data are on a logarithmic graph, on the horizontal axis there is the power density and on the vertical axis there is the energy density. The blue lines divide the chart in different sector labelled with the time at which the technology lasts. If we take a 100[kg] FC is possible to get a device with 20 – 80[kWh] but 1 – 3[kW]. Actually, it is correct to say that FCs have a high energy density, but they are not true storage systems, in fact they are continuously fed by a fuel tank external to them. If we think about the Li-ion battery, different consideration can be drawn. For a 100[kg] we could use 4 – 20[kWh] that is lower than FCs but using a 10 – 30[kW] power, 10 times the FC. These two technologies are opposite, therefore the combination of both is the perfect solution to get high energy and high power to run a rolling stock.

Now let's focus on the two single parts. The Hydrogen Fuel Cell are a particular device which allows to convert molecules of Hydrogen into electrical energy by using a chemical procedure. This method is sustainable since the reaction creates water and heat instead of CO<sub>2</sub> such as DE. We are going to analyse in depth how it works.

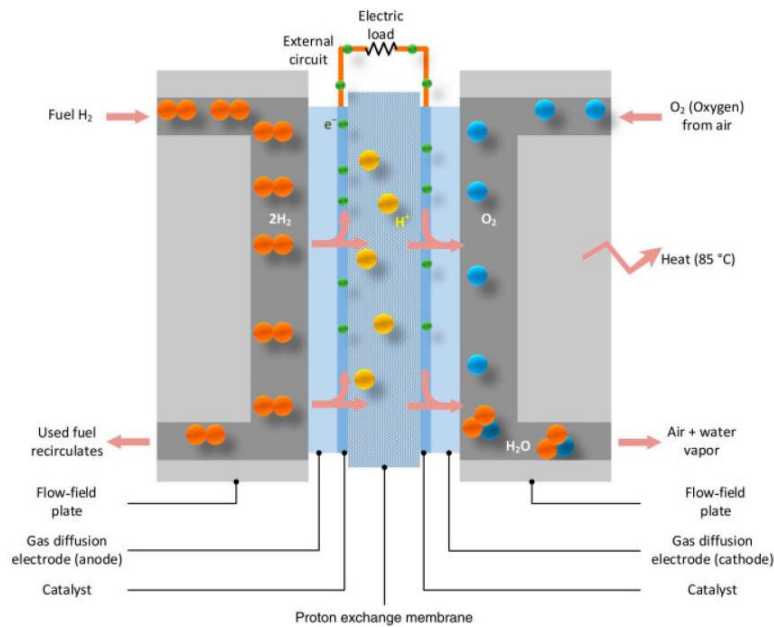
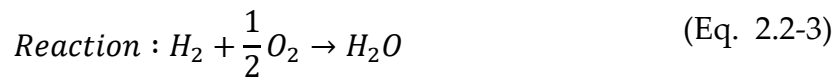
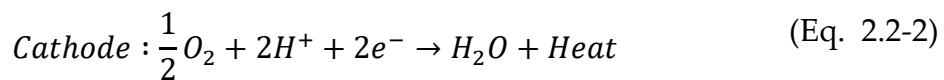


Figure 2.2-2 : Hydrogen Fuel Cell working scheme [5]

The cell consists of two electrodes, anode and cathode, and a proton-exchange membrane, also called Proton-Exchange Membrane Fuel Cell (PEMFC). The presence of the membrane allows to have lower operating temperature (about 50 – 100°C), faster start-up, high-power density, and low corrosion. It has some disadvantages, such as sensitivity to fuel impurities, which requires high-quality hydrogen. Moreover, it is necessary to introduce several devices for the working conditions such as compressors, pump, radiator, and electric control equipment. The reaction that describes the process is a redox and the chemical formulas is [5]:



Hydrogen passes through the anode while Oxygen passes through the cathode. In the anode, the Hydrogen is split into electron and proton (Eq. 2.2-1). The positive particles of hydrogen could pass the membrane, but the negative ones can't. However, admit to equalizing charge and to achieve that electron must be forced through another path, or better pushed into an electrical circuit generating a flow of electrons and heat. In the cathode, water will be generated from the combination of hydrogen and oxygen (Eq. 2.2-2). Since there are only static parts, the Fuel Cell are more reliable.

This is how a single cell works. Every single one can create a voltage from 0.5 – 1[V] that is too low to supply a common load. Several cells are bundled together to create a so-called stack.

As known, the fuel cells are not ideal sources. The characteristic  $v - i$  is shown in the Figure 2.2-3.

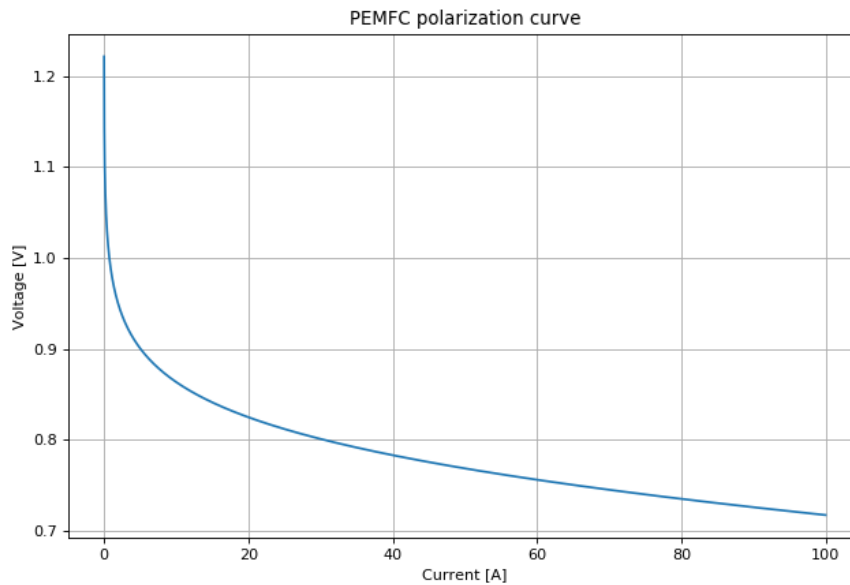


Figure 2.2-3 :  $v - i$  characteristic curve [3]

Since this diagram only concerns one cell, a problem occurs. Depending on the current, the voltage changes, and to obtain the total stack voltage, we multiply it by the number of cells that must be installed to reach the rated voltage. If we consider a controlled motor, it is known that the current varies during the operation, and consequently the voltage will also change. For instance, here are some easy calculations to prove this. Considering a stack composed by 100 cells and rated current of 40[A] in DC. When the current is not required, the no-load voltage is a little more than 1[V]. For 100 cells become an overall voltage about 100[V]. When we reach the rated current, the single cell performs less than 0.8[V] and the overall stack voltage turns less than 80[V]. It means that from the no-load to rated condition we lose about  $\Delta V = 20[V]$ . That is more relevant if a high voltage application is needed. We will need to size the number of cells to get the nominal voltage at nominal current, taking also into account of the isolation that should be designed to maintain the maximum voltages and not the rated one.

In the design, it is assumed that the fuel cells generate about 70[A] at most, so from Figure 2.2-3, each cell could supply about 0.75[V]. Since we need a nominal voltage  $V_n = 750[V]$ , it means that at least 1000 cells are needed. As a drawback, the isolation voltage rises to  $\approx 1 - 1.05[kV]$ .

The ability of batteries is to store chemical energy and convert it into electrical form when needed. Batteries perform many functions in railway systems, such as safety and operations. But, in our case, they play a key role in traction. They are able to power the engines when FC power is insufficient to meet the drag force created by air and ground

conditions. The type used is a lithium-ion battery. As shown above, they are not capable of storing a large amount of energy. Instead, they are useful for the power they could release. Due to these characteristics, the batteries will only be used when necessary, mainly during acceleration phases.

Lithium-ion batteries are made with phosphate as the cathode to be safer. Their safety is also ensured by a combination of prevention, mitigation and shielding systems, moreover, each battery is equipped with electronic protection. For our purpose, this typology provides a valid solution.

Like fuel cells, batteries have a non-ideal behaviour and change their output voltage according to the amount of energy stored.

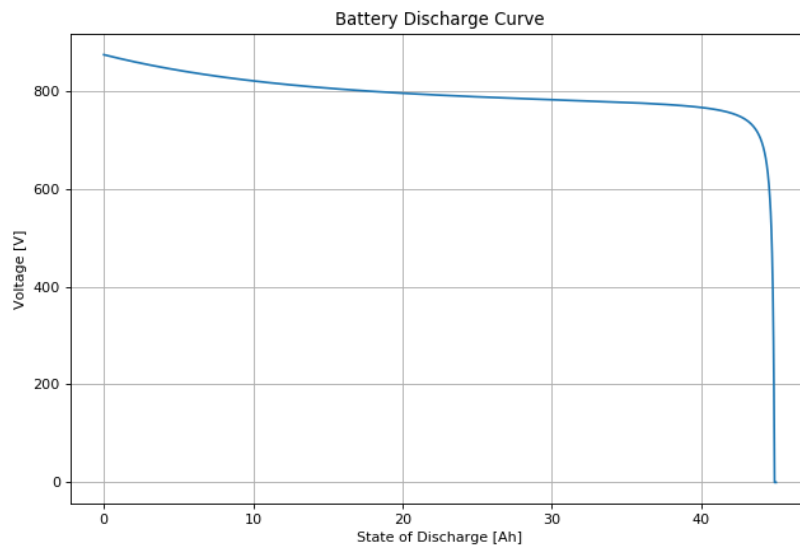


Figure 2.2-4 :  $v - Ah$  chart

The example described by the Figure 2.2-4 is related to a battery stack with a nominal voltage of  $V_n = 750[V]$  and a capacity of  $C = 45[Ah]$ . It is essential to pay attention to the horizontal axis that indicates the state of discharge instead of the state of charge. This means that, however much energy has been consumed, the voltage decreases. Actually, we can see the starting voltage when the battery is fully charged at 0[Ah] which is much higher than the nominal voltage, about 844[V] and reach  $V_n$  at about 45[Ah] before the knee on the right. The fact that both FC and battery change their voltage over time adds a problem to the control, but since the new configuration electrically divides the two parts, it becomes easier to handle this problem.

### 2.3. Motor and Its Equations

The engine plays a key role in the new configuration. It could be said that it is the heart of the project. We will use a Double-Three Phase Permanent Magnet Synchronous Machine (DTPMSM), since it can be powered by two different three-phase circuits (Figure 2.1-5). In addition, a multiphase machine offers reliability, which is crucial in traction systems. There are other advantages, such as the decrease in harmonic distortion and total losses, which result in much higher efficiency and greater fault tolerance. There are also disadvantages, such as stator current harmonics, especially the DC component that does not generate the air gap flux [1]. Six phase machines are designed with different configurations respect to the displacement between each phase of the two windings which could be  $0^\circ$  (dual three-phase),  $30^\circ$  (asymmetrical six-phase), and  $60^\circ$  (symmetrical six-phase) as seen in Figure 2.3-1. In our project, we will refer to the asymmetrical six-phase as DTPMSM. This choice is due to the low torque ripples when a six-step inverter is used. However, with modern high-frequency methods, symmetrical three-phase could also be a good solution [8].

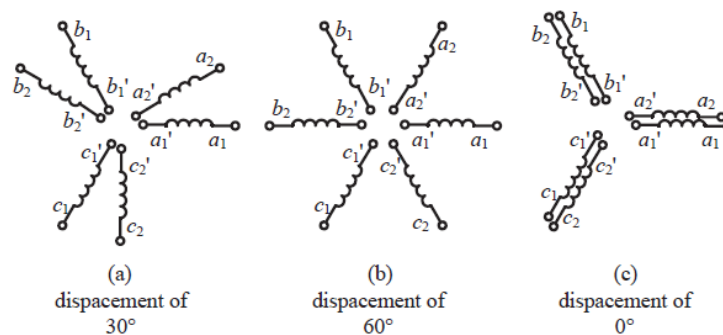


Figure 2.3-1 : Stator winding arrangement for (a) asymmetrical six-phase, (b) symmetrical six-phase, and (c) dual three-phase machines. [7]

Each group of phases has its own neutral point:  $a'_1 - b'_1 - c'_1$  fall at the same point and also  $a'_2 - b'_2 - c'_2$  fall at the same point but different for the first winding. In this way, it could be possible to deal with each circuit as one with a mutual effect on the other.

The two windings are placed on the stator, the permanent magnet on the rotor. The choice is to use an isotropic machine; thus, the PMs are uniformly distributed. Another disadvantage is related to the fault condition. Indeed, at this moment, the motor remains connected to the shaft. Since the PMs create an induced flux, an induced voltage is created in the faulty windings, which causes the motor to overheat and become damaged. For this reason, a clutch should be used to disconnect the motor. This is an old technique. It was therefore thought that applying a method of weakening the field below the base velocity could reduce the effect of the fault [1].

To study his operation, is important to start looking at the disposition of the windings. All the equations are taken by [1].

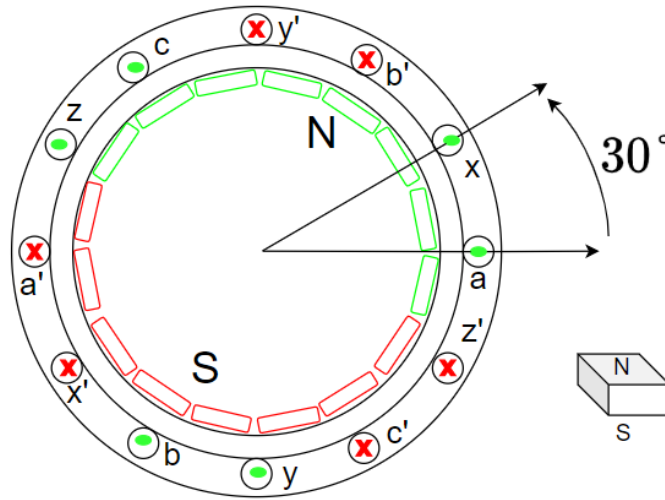


Figure 2.3-2 : Disposition of the stator windings

$$v_s = R_s i_s + p\psi_s \tag{Eq. 2.3-1}$$

$$\psi_s = L_s i_s + \gamma\psi_{pm}$$

Where:

Table 2.3-1 : Motor Equation Symbols

Variable	Description	SI unit
$v_s$	Stator Voltage Vector	$V$
$R_s$	Stator Resistance	$\Omega$
$i_s$	Stator Current Vector	$A$
$\psi_s$	Stator Flux Vector	$Wb$
$\psi_{pm}$	PM Flux	$Wb$
$\gamma$	Phase difference between the two groups	$^\circ - rad$

The vectors that constitute the equations are:

$$\begin{aligned}
 v_s &= [v_a \ v_b \ v_c \ v_x \ v_y \ v_z]^T \\
 i_s &= [i_a \ i_b \ i_c \ i_x \ i_y \ i_z]^T \\
 \psi_s &= [\psi_a \ \psi_b \ \psi_c \ \psi_x \ \psi_y \ \psi_z]^T \\
 R_s &= R_s * I_{6 \times 6} \\
 L_s &= L_{ls} I_{6 \times 6} + \frac{L_a + L_b}{2} T_1 + \frac{L_a - L_b}{2} T_2
 \end{aligned} \tag{Eq. 2.3-2}$$

Table 2.3-2 : Symbols of Inductances

Variable	Description	SI unit
$I_{6 \times 6}$	Identity Matrix	
$L_{ls}$	Leakage inductance	H
$L_a$	Main Self-inductance d-axis	H
$L_b$	Main Self-inductance q-axis	H
$T_1 - T_2$	Transformation Matrix (Appendix A.1-A.2)	

To simplify the study, the Clarke-Park transformation is applied to the variables (Appendix A.3-A.4). In this way, two three-phase systems can be converted into two d-q axes on the rotation frame fixed with the rotor.

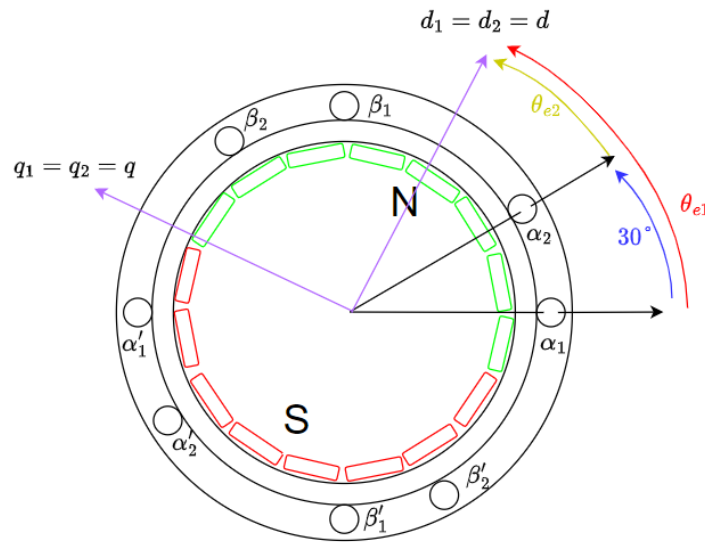


Figure 2.3-3 :  $d - q$  axes on the rotor and  $\alpha - \beta$  axes on the stator respectively from winding  $abc$  and  $xyz$

The matrix equations after Park's transformation are:

$$\begin{bmatrix} v_{d1} \\ v_{q1} \\ v_{d2} \\ v_{q2} \end{bmatrix} = \begin{bmatrix} R_s & 0 & 0 & 0 \\ 0 & R_s & 0 & 0 \\ 0 & 0 & R_s & 0 \\ 0 & 0 & 0 & R_s \end{bmatrix} \begin{bmatrix} i_{d1} \\ i_{q1} \\ i_{d2} \\ i_{q2} \end{bmatrix} + \frac{d}{dt} \begin{bmatrix} \psi_{d1} \\ \psi_{q1} \\ \psi_{d2} \\ \psi_{q2} \end{bmatrix} + \omega \begin{bmatrix} -\psi_{q1} \\ \psi_{d1} \\ -\psi_{q2} \\ \psi_{d2} \end{bmatrix} \quad (\text{Eq. 2.3-3})$$



$$\begin{bmatrix} \psi_{d1} \\ \psi_{q1} \\ \psi_{d2} \\ \psi_{q2} \end{bmatrix} = \begin{bmatrix} L_{d1} & 0 & M_{d21} & 0 \\ 0 & L_{q1} & 0 & M_{q21} \\ M_{d12} & 0 & L_{d2} & 0 \\ 0 & M_{q12} & 0 & L_{q2} \end{bmatrix} \begin{bmatrix} i_{d1} \\ i_{q1} \\ i_{d2} \\ i_{q2} \end{bmatrix} + \begin{bmatrix} \psi_{pm} \\ 0 \\ \psi_{pm} \\ 0 \end{bmatrix} \quad (\text{Eq. 2.3-4})$$

Where  $M_{d12}, M_{d21}, M_{q12}, M_{q21}$  are referred to the magnetic coupling of the two stator windings with the rotor.  $d_1, d_2, q_1, q_2$  quantities are projected on the same  $d - q$  axis (purple on Figure 2.3-3), the difference is only who creates the effect on the rotor frame.  $\omega_e = \frac{d}{dt} \theta_e$  is the electrical rotational speed. To get the mechanical speed is necessary to divide the electrical by the numbers of pair poles  $n_p$ . In the following, the time derivative  $\frac{d}{dt}$  is indicated by  $p$ .

Since our machine is isotropic, or rather a surface mount PM, the following assumptions are made:

$$\begin{array}{llll} L_{d1} = L_{d2} & L_{q1} = L_{q2} & M_{d12} = M_{d21} & M_{q12} = M_{q21} \\ = L_d & = L_q & = M_d & = M_q \end{array} \quad (\text{Eq. 2.3-5})$$

And:

$$\begin{aligned} \psi_{d1} &= L_d i_{d1} + M_d i_{d2} + \psi_{pm} \\ \psi_{q1} &= L_q i_{q1} + M_q i_{q2} \\ \psi_{d2} &= L_d i_{d2} + M_d i_{d1} + \psi_{pm} \\ \psi_{q2} &= L_q i_{q2} + M_q i_{q1} \end{aligned} \quad (\text{Eq. 2.3-6})$$

There is a reciprocal effect in the flux equations for both the first and second windings.

The final stator equations could be expressed as follow:

$$\begin{aligned} v_{d1} &= R_s i_{d1} + L_d p i_{d1} + M_d p i_{d2} - \Omega_m L_q i_{q1} - \Omega_m M_q i_{q2} \\ v_{d2} &= R_s i_{d2} + L_d p i_{d2} + M_d p i_{d1} - \Omega_m L_q i_{q2} - \Omega_m M_q i_{q1} \\ v_{q1} &= R_s i_{q1} + L_q p i_{q1} + M_q p i_{q2} + \Omega_m L_d i_{d1} + \Omega_m M_d i_{d2} + \Omega_m \psi_{pm} \\ v_{q2} &= R_s i_{q2} + L_q p i_{q2} + M_q p i_{q1} + \Omega_m L_d i_{d2} + \Omega_m M_d i_{d1} + \Omega_m \psi_{pm} \end{aligned} \quad (\text{Eq. 2.3-7})$$

It is useful to note that each voltage on the  $dq$  axes has a mutual effect which depends on the currents on the other windings.



What we are more interested in is the power absorbed by the motor. Assuming that  $R_s$  is negligible:

$$\begin{aligned}
 P_{el} &= Re \{ \overline{v_{s1}} i_{s1} + \overline{v_{s2}} i_{s2} \} \\
 P_{el} &= \frac{3}{2} (v_{d1} i_{d1} + v_{q1} i_{q1}) + \frac{3}{2} (v_{d2} i_{d2} + v_{q2} i_{q2}) \\
 P_{el} &= \frac{3}{2} \omega (\psi_{d1} i_{q1} - \psi_{q1} i_{d1}) + \frac{3}{2} \omega (\psi_{d2} i_{q2} - \psi_{q2} i_{d2}) \quad (\text{Eq. 2.3-8}) \\
 T_e &= \frac{P_{el}}{\Omega_m} = \frac{P_{el}}{\left( \frac{\omega}{n_p} \right)}
 \end{aligned}$$

$$\begin{aligned}
 T_e &= \frac{3}{2} n_p (\psi_{d1} i_{q1} - \psi_{q1} i_{d1} + \psi_{d2} i_{q2} - \psi_{q2} i_{d2}) = \\
 &= \frac{3}{2} n_p [\psi_{pm} (i_{q1} + i_{q2}) + (L_d - L_q) (i_{d1} i_{q1} + i_{d2} i_{q2}) + (M_d - M_q) (i_{d1} i_{q2} + i_{d2} i_{q1}) ]
 \end{aligned}$$

Considering the assumption of an isotropic machine, the self and mutual inductances are equal on the  $d$  and  $q$  axes. This means that  $L_d = L_q = L_s$  and  $M_d = M_q = M_s$ .

After a few manipulations, the electrical torque becomes lighter, and the mechanical equation can be performed as follows.

$$\begin{aligned}
 T_e &= \frac{3}{2} n_p \psi_{pm} (i_{q1} + i_{q2}) \\
 T_e - T_r &= J_{eq} * \frac{d}{dt} \Omega_m + \beta \Omega_m \quad (\text{Eq. 2.3-9})
 \end{aligned}$$

In

(Eq. 2.3-9) there are some elements that are constant such as the flux  $\psi_{pm}$  due to the PM inside the rotor, the number of pair poles by construction and the coefficient beside the equation. The interesting part of the electromechanical torque is the sum of the quadrature currents of the two windings. This aspect plays a fundamental role in control. Basically, each machine has its nominal parameters, and one of these is the rated current, which indicates the value of the current allowed without losing the property of the insulation part. Following this definition, since the nominal current is  $i_s = \sqrt{i_d^2 + i_q^2}$  and only the  $i_q$  give a significant contribution to the torque, we could fix  $i_d = 0[A]$  and push the  $i_q$  near to  $i_s$ .

This theory imposes a linear behaviour also at the voltage in

(Eq. 2.3-7). From the beginning, at zero speed the voltage rises linearly until the nominal value  $V_n$ . The value of the speed at this point is called "base speed". In theory, by operating only at the quadrature current, the base speed cannot be exceeded. It is

necessary, after this point, to modify the control in its entirety as described in note [9]. Since this is not necessary for the project, it will not be explained and used. You can also find more information in [1].

Actually, the project does not require a complete study of the train, but only one motor is needed to validate our data. For this reason, with some adjustment is possible to size the overall parameters of the train according to the performance of each engine. Each carriage is composed by two motors, two pack of fuel cell and two pack of battery as in figure shown.

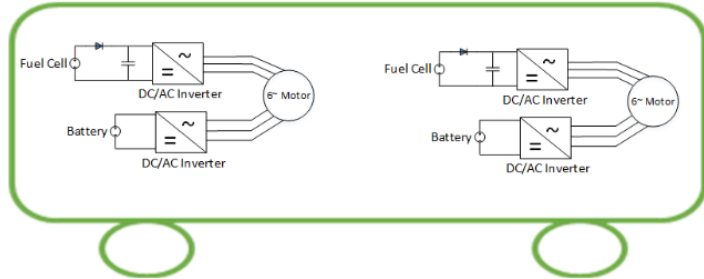


Figure 2.3-4 : Proposed system for each carriage [1]

Therefore, all variables are dimensioned to correspond to the operation of a single motor. We are referring to overall mass, inertia, FC and battery power.

The mass of the train is  $m_{tot} = 150[tons]$ , each carriage has two motors. Each motor could carry  $m_m = \frac{150[tons]}{8} = 18.75[tons]$ .

To choose the right motor for our application, we need another crucial parameter, namely the Nominal Resistant Torque  $T_{rn}$  that the train must oppose under acceleration and in coasting mode. In particular, there is an empirical formula which takes into account all these resistive components and makes it possible to describe the resistance torque that a train undergoes during its journey. This formula is called the Davis equation.

$$R[N] = A + B * v + C * v^2 + m_m * g * grad \quad (\text{Eq. 2.3-10})$$

Where  $R[N]$  is the resistive force,  $v \left[ \frac{m}{s} \right]$  is the speed of the train,  $A = 16.51, B = 1.1e - 3, C = 13.09$  are the Davis coefficients representing the behaviour of the force. Where  $m_m[kg]$  is the mass of the train for a single motor,  $g \left[ \frac{m}{s^2} \right]$  is the acceleration of gravity and  $grad[\%o]$  is the gradient of the earth.

The last contribution of the resistance force is called Grade Resistance  $R_{grad}$ . This term appears if the vehicle is travelling over a surface with positive or negative slope. We can draw the force like in Figure 2.3-5.

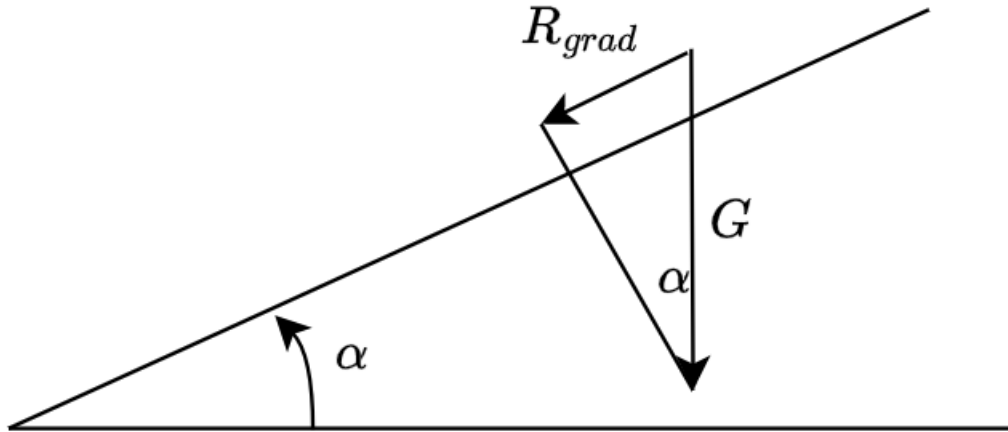


Figure 2.3-5 : Representation of a gradient

The formulae which describe the force is:

$$R_{grad}[N] = m_m * g * \sin(\alpha) \quad (\text{Eq. 2.3-11})$$

Since  $\alpha$  is a very low, then  $\sin(\alpha) \approx \alpha$

$$R_{grad}[N] = m_m * g * \alpha \quad (\text{Eq. 2.3-12})$$

Since we calculate the resistive force, we must convert it into a torque with:

$$T_r[Nm] = R[N] * \frac{d_w/2[m]}{g_r} \quad (\text{Eq. 2.3-13})$$

Where  $d_w = 1[m]$  is the wheel diameter and  $g_r = 6$  is the gear ratio. Figure 2.3-6 shows the behaviour of the resistant torque as the speed increases. It does not take gradient into account.

We assume that the rated speed is  $\Omega_n = 157 \left[ \frac{rad}{s} \right]$ ,  $v_n = \Omega_n * \frac{d_w/2}{g_r} \approx 13.08 \left[ \frac{m}{s} \right] \approx 47.1 \left[ \frac{km}{h} \right]$  which means that the maximum resistant torque at nominal speed is about  $188[Nm]$ . We assume  $T_{rn} = 200[Nm]$ .

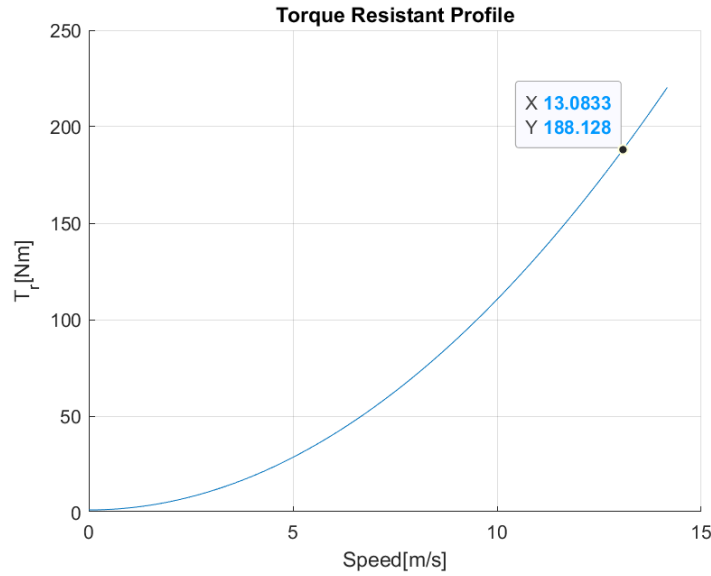


Figure 2.3-6 : Resistant Torque Profile

We need a motor that pushes more than 200[Nm] under the nominal conditions to accelerate the engine. The choice falls on a motor with a nominal electromagnetic torque of  $T_n = 750[Nm]$  and maximum of  $T_{max} = 850[Nm]$  (for 2 minutes).

As far as inertia is concerned, we have to perform some simple calculations using the equivalent mass  $m_e$ . This parameter takes into account the mass of the train itself plus a quantity that considers the inertia of all rotating components on the vehicles. The concept is derived from Konig's Theorem.

$$\begin{aligned}
 m_e &= \delta * m_m \\
 \delta &= 1 + 0.04 + 0.0025 * g_r^2 = 1.13 \\
 m_e &= 21.187[tons] \\
 J_{eq} &= m_e * \left(\frac{d_w/2}{g_r}\right)^2 = 21.187[tons] * \left(\frac{0.5[m]}{6}\right)^2 \\
 &= 147.135[kgm^2]
 \end{aligned}
 \tag{Eq. 2.3-14}$$

By inverting the mechanical equation, we can calculate the acceleration we could achieve:

$$\begin{aligned}
 \frac{d}{dt} \Omega_m &\approx \frac{T_{max} - T_{rn}}{J_{eq}} = \frac{850[Nm] - 200[Nm]}{147.135[kgm^2]} = 4.33 \left[\frac{rad}{s^2}\right] \\
 &\approx 0.36 \left[\frac{m}{s^2}\right]
 \end{aligned}
 \tag{Eq. 2.3-15}$$

This acceleration value allows to increase the velocity also in the worst conditions.

The rated power can be calculated by the rated torque and speed:

$$P_n = T_n * \Omega_n = 750[Nm] * 157 \left[ \frac{rad}{s} \right] \approx 120[kW] \quad (\text{Eq. 2.3-16})$$

The voltage on the motor is imposed by construction and it is  $V_n = 359[V]$  and the  $\cos\varphi = 0.96$ .

Instead, the phase current can be performed by the parameters just calculated:

$$I_{pRMS} = \frac{P_n}{\sqrt{3} * V_n * \cos\varphi} = \frac{120[kW]}{\sqrt{3} * 359[V] * 0.96} = 201[A] \quad (\text{Eq. 2.3-17})$$

Which means that the maximum  $i_s$  (or  $i_q$ ) is:

$$i_{smax} = I_{pRMS} * \sqrt{2} \approx 285[A] \quad (\text{Eq. 2.3-18})$$

The double three-phase machine chosen has these parameters:

Table 2.3-3 : Datasheet of the Proposed PM Machine

Data	Value
$n_p$	2
$T_n$	750[Nm]
$\Omega_n$	157[rad/s]
$P_n$	120[kW]
$T_{max}$	850[Nm] for 2min
$V_n$	359[V]
$\eta$	96.4%
$\cos\varphi$	0.96
$I_{pRMS}$	201[A]
$R_s$	0.0088[Ω]
$L_a = L_b$	0.897[mH]
$L_{ls}$	0.207[mH]
$J_M$	1.065[kgm <sup>2</sup> ]
$J_{eq}$	147.135[kgm <sup>2</sup> ]
$\beta$	0.094 $\left[ \frac{kgm^2}{s} \right]$
$\psi_{pm}$	0.97[Wb]
N° of Carriage	4
N° of motor in each Carriage	2
Gear Ratio $g_r$	6
Wheel diameter $d_w$	1[m]

From the above parameters, it is possible to calculate  $L_d, L_q, M_d, M_q$ .

Data	Value
$L_d = L_q = L_s$	5.175[mH]
$M_d = M_q = M_s$	2.691[mH]

Since hydrogen fuel cells are the main source of our light train, we could size it using engine power. We want to use the fuel cell at nominal speed and nominal resistant torque. In other cases, the battery will help the fuel cell achieve the required torque or break the train regeneratively.

The power required by the fuel cell is derived from the resistant torque equal to 200[Nm]. Thus far, it is possible to calculate the power to size the fuel cell:

$$P_{FC} = T_{rn} * \Omega_n \approx 31.4[kW] \quad (\text{Eq. 2.3-19})$$

Consequently, the power of the battery will be at least:

$$P_{batt} = P_n - P_{FCn} = 120[kW] - 31.4[kW] = 88.6[kW] \quad (\text{Eq. 2.3-20})$$

Actually, we decided to oversize the battery until 90[kW] in order to have enough power for each situation.

## 2.4. Scheme of control: Field Oriented Control (FOC)

In this section we will analyse the equation of the DTPMSM to learn how to use it, how to supply it and in which way we can push or recover power. This study could be interesting but at the same time difficult to manage. For this reason, some assumptions are needed to understand what happens in the machine during its running. All the next calculation are made using  $d - q$  axes frame as reference.

The first hypothesis is that the two circuits are considered separately. We will focus our study on the first winding.

As already mentioned, the direct current does not affect the electric torque and can be set to zero. In this way, the quadrature current should reach the value of the rated current and deliver the maximum torque. Furthermore, it is possible to interrupt the power flowing in the second winding because we want to concentrate on the first winding only. For this purpose, the second quadrature current must also be set equal to zero. Another simplification is neglect the dissipative terms  $R_s$ . Finally. The following calculations will be done in steady state conditions, which means the derivative terms are zero. To sum up:

$$i_{q1} \neq 0, i_{q2} = 0, i_{d1} = 0, i_{d2} = 0, R_s = 0 \quad (\text{Eq. 2.4-1})$$

Applying these hypotheses to the (Eq. 2.3-7) we get:

$$\begin{aligned}
 v_{d1} &= -\omega L_q i_{q1} \\
 v_{d2} &= -\omega M_q i_{q1} \\
 v_{q1} &= +\omega \psi_{pm} \\
 v_{q2} &= +\omega \psi_{pm}
 \end{aligned}
 \tag{Eq. 2.4-2}$$

Drawing  $v_{d1}, v_{q1}$  in a d-q axes chart:

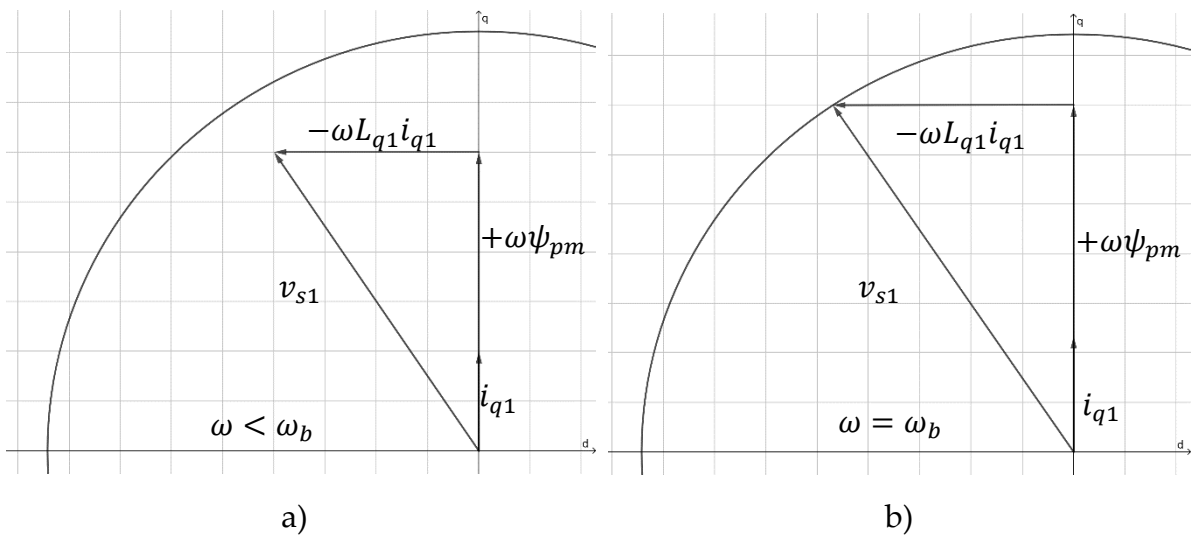


Figure 2.4-1 : Vector Diagram of the position for the voltage of the First Winding below the Base Speed (a) and at the Base Speed(b)

The Figure 2.4-1 show the evolution of electrical parameters during different stages. The quadrature current  $i_{q1}$  is constant and equal to the nominal  $i_{s1}$  since we want to operate with constant torque (below  $\omega_b$ ). Only the first winding creates torque, which drives the motor, the back-emf vector  $E = +\omega \psi_{pm}$  and  $v_{d1} = -\omega L_{q1} i_{q1}$  increase linearly until the maximum of  $v_{s1} = v_{d1} + jv_{q1}$ . After  $V_{max}$  is no more possible to increase the speed by using this technique. For more details, please refer to the field weakening in [1]. Combining this information, we can create a graph of the electrical parameters in function of the speed.

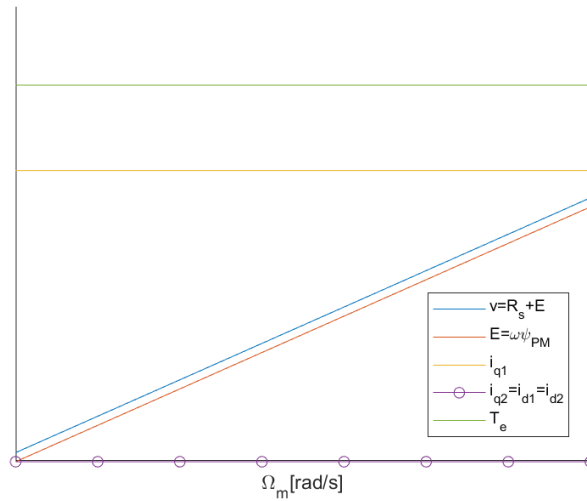


Figure 2.4-2 : Operating region of DTPMSM for only one winding

The graph confirms the previous explanation. Looking at the formulae, the back-emf starts from zero and increases linearly with speed. The same happens to  $v_s$  which at zero speed has a non-zero initial value due to the resistive part  $R_s$ . It increases like the back-emf but at some point, at base speed, it has to stop because the rated voltage is reached. Torque, on the other hand, has a constant behaviour due to the constant value of  $i_{q1}$ . In the figure, the only contribution to torque comes from the first winding since  $i_{q2} = 0$ . In reality, what happens in our design is somewhat different. As mechanical equation (Eq. 2.3-9) says, the way to control speed is to match the electromagnetic torque to the resistant torque, in particular the difference between the two creates motor acceleration. Therefore, it is not necessary to have the maximum  $T_e$  for each speed, but it is necessary to manage it and match the resistant torque to obtain the desired speed. This is the approach to control each winding separately. By using the overlap between the two windings, the effects can be combined to achieve a more powerful and controllable approach. The type of control used is Field Oriented Control (FOC) in Figure 2.4-3.



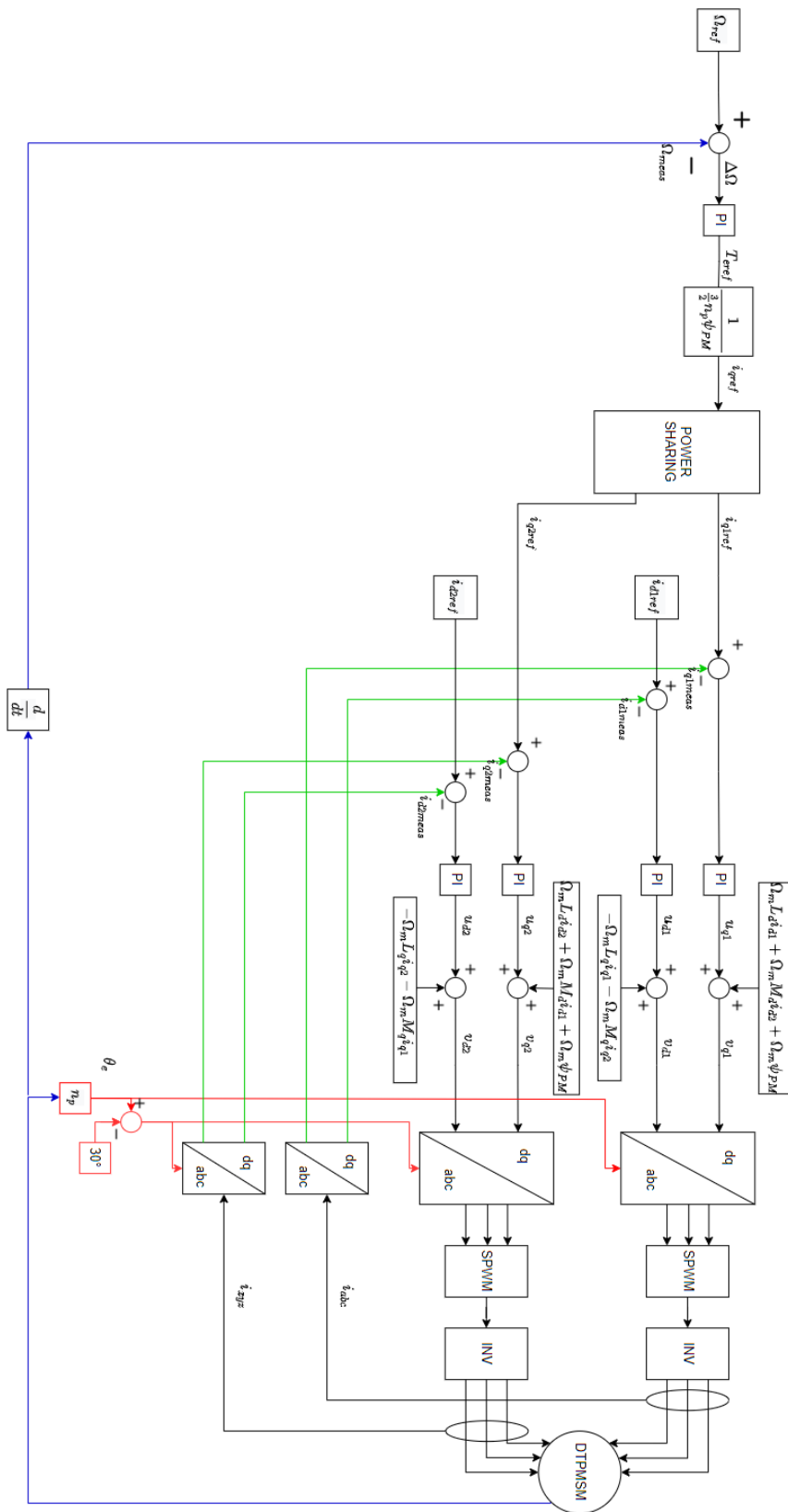


Figure 2.4-3 : FOC scheme of a DTPMSM with a displacement of 30°

There are several parts represented by blocks. The inverter one (INV) will be discussed in detail in the Section 2.6.1, up to now we can consider it as the power unit which converts the reference signals in power signals.

The control scheme can be divided into two main loops, an inner and an outer loop. The inner loop starts from the imposition of currents after the  $T_{eref}$  until the creation of the voltage signal on the power converter. The current controller is a single-input, single-output (SISO) PI controller. The outer instead begins from the speed reference, includes is slower from the inner loop.

The inner loop works by using an error as input on the currents, which is the difference between the reference values to be had on the machine and the actual measured currents values. This method is applied to  $i_{d1}, i_{q1}, i_{d2}, i_{q2}$  singularly and since they have the same electrical parameters, the calculations will be faster. The output of the controller is  $u_{d1}, u_{q1}, u_{d2}, u_{q2}$  respectively, which models just the voltage drop across the motor impedance  $u_s$  : it does not take into account the effects of mutual and back-emf, which are then added after the PI controller to compensate for the input value. Each voltage has its own mutual variables.

Thus, the system (electrical part of the motor) is modelled by

$$u_s = R_s i_s + L_s p i_s \quad (\text{Eq. 2.4-3})$$

Using the Laplace transformation, the transfer function becomes:

$$G_i(s) = \frac{1}{L_s s + R_s} \quad (\text{Eq. 2.4-4})$$

The outer loop, on the other hand, is used to tell how much current we need to feed into the machine to reach a reference speed. As in the inner loop, there is a PI controller. Its input is the speed error, and its output is the required torque. The equation followed by the system (mechanical part of the motor) is (Eq. 2.3-9). In the Laplace domain, the transfer function is:

$$G_m(s) = \frac{1}{J_{eq} s + \beta} \quad (\text{Eq. 2.4-5})$$

The torque on the output is proportional to the sum of  $i_{q1}$  and  $i_{q2}$ , which becomes  $i_{qref}$  the reference for the inner loop. But a question comes up.

How much current should be driven in each winding? Which is the decisive parameter? Is too early to answer and it will be discussed in the power sharing chapter (5). For the first tests, we consider the power sharing block as a 50-50% share. That means

$$i_{q1ref} = i_{q2ref} = \frac{i_{qref}}{2}$$

Practically speaking, this control scheme will be the algorithm implemented in the microcontroller. The PI operation is analysed better in the next chapter 2.5, which presents PID regulators

## 2.5. PID regulator

As seen in the FOC diagram, there are certain blocks called 'PID' that play a key role in the stability, efficiency, and simplicity of the algorithm since they are linear regulator. Moreover, over time, calibration methods suited for this typology of regulator have been developed using simple rules. The PID controller continuously applies a correction based on the input error from the desired setpoint and the actual value of a variable. This means that every time a discrepancy occurs with respect to the expected behaviour, the PID controller intervenes by modifying the variables and attempting to compensate for the differences in a predefined time.

But why is it called PID?

This name is due to how the error is handled. In particular, three different actions take place. "P" term is the proportional, "I" stands for the integrative and finally "D" for the derivative. By schematising a 'PID' in blocks, the terms can be seen individually [10].

- "P" term: it literally multiplies the input error by using a gain value  $k_p$
- "I" term: it is proportional by a gain  $k_i$  to the integral of the error which is its average value. It is required to impose that the error cancels asymptotically in presence of constant additive disturbance.
- "D" term: it is proportional by a gain  $k_d$  to the derivative of the error. The derivative function has the purpose of trying to anticipate the error in future instants.

The mathematical connection from the error and the output is [10]:

$$u(t) = k_p e(t) + k_i \int_{t_0}^t e(\tau) d\tau + k_d \frac{de(t)}{dt} \quad (\text{Eq. 2.5-1})$$

$$k_p, k_i, k_d \geq 0$$

The PID are SISO, linear and stationary systems. Applying the Laplace's transform, the PID are described with the transfer function [10]:

$$R_{PID}(s) = k_p + \frac{k_i}{s} + K_D s \quad (\text{Eq. 2.5-2})$$

$$R_{PID}(s) = k_p \left( 1 + \frac{1}{T_I s} + T_D s \right)$$

$$T_I = \frac{k_p}{k_i} \rightarrow \text{integral time} \quad T_D = \frac{K_D}{k_p} \rightarrow \text{derivative time}$$

The controller used in the FOC is only a 'PI'. The derivative gain term is set to zero. This type is used in systems where integral action is required to have static performance and the presence of a zero in the transfer function to have a wider bandwidth than the integral controller only. Moreover, they are also easier to calibrate than 'PID'. Their transfer function is:

$$R_{PI}(s) = k_p + \frac{k_i}{s} = \frac{k_p(1 + T_I s)}{T_I s} \quad (\text{Eq. 2.5-3})$$

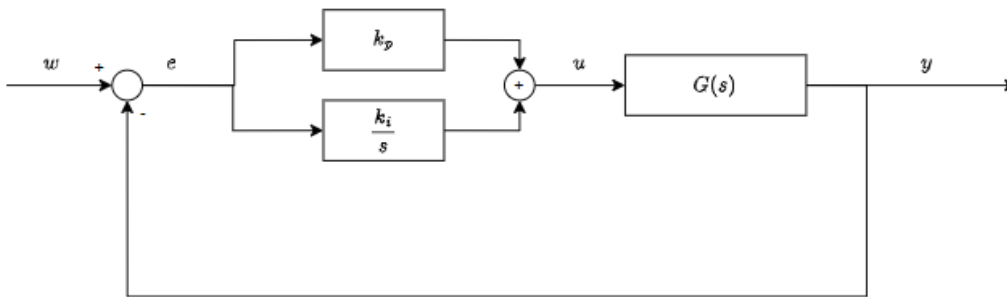


Figure 2.5-1 : PI controller basic scheme

As already mentioned, there are many useful and simple ways to configure the controller. It is essential to understand which one is used in the project and how. In particular, we have five PI controllers: one for the speed and the other four for the direct and quadrature currents. The scheme of a general control is shown in the Figure 2.5-2.

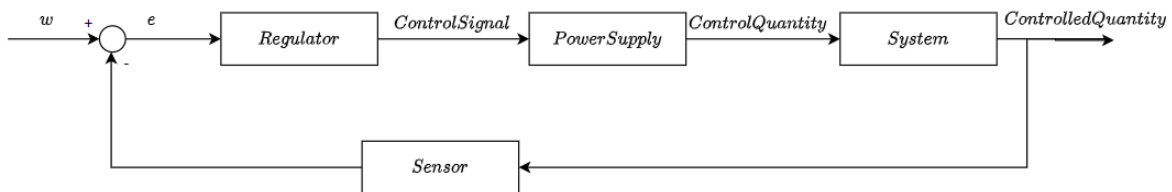


Figure 2.5-2 : General control scheme of a simple system [11]

Since the power supply and sensors are assumed to be ideal, they have a unitary transfer function. The diagram then becomes simpler:

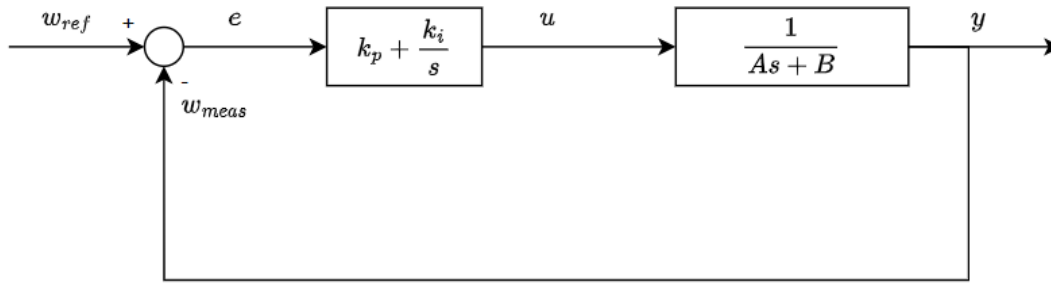


Figure 2.5-3 : Considered scheme control [11]

Calibrating the regulators means adjusting the  $k_p$  and  $k_i$  values. Since the transfer functions (Eq. 2.4-4) and (Eq. 2.4-5) have the same form but different values, they will be written in the manner:

$$G(s) = \frac{1}{As + B} \quad (\text{Eq. 2.5-4})$$

This allows a single algorithm to be created for the five PI controllers.

First of all, the bandwidth of the closed-loop system must be chosen. By definition, the bandwidth is the pulsation  $\omega_{bw}$  where the closed-loop transfer function equals -3dB. This assumption is fundamental since it will be the basis for performing our calibration. There are some basic rules to choose the  $\omega_{bw}$  [10]:

- The controlled variable must be, at least ten times, faster than the change in the reference. In particular, for sinusoidal reference  $\omega_{bw} = 10 * 2\pi f_{ref}$ . For a square wave reference, the rated value is reached in  $5\tau$  where  $\tau = \frac{A}{B}$ . To get a ten-time faster response the rated value should be reached  $\frac{5\tau}{10}$  so the  $\omega_{bw} = \frac{2\pi}{\frac{5\tau}{10}}$ .
- The inner loop variable should be at least ten times faster than the outer one. Furthermore, this assumption introduces a further simplification in the calibration of the PI, since the inner loop could be seen as a unit transfer function from the outer one. Thus, it is possible to calibrate both separately.
- It should be suitable for the dynamic of the system which means comparable to the derivative of the variables.

Once you have chosen the bandwidth, you can use the definition and perform the calculation in proximity to it.

By using the mathematical form, the definition says [11]:

$$\|F(j\omega_{bw})\| = -3dB = 10^{-\frac{3}{20}} \approx \frac{1}{\sqrt{2}}$$

$$\|F(j\omega_{bw})\|^2 = \frac{1}{2} \quad (\text{Eq. 2.5-5})$$

Where:

$$s = j\omega$$

$$F(s) = \frac{L(s)}{1 + L(s)}$$

$$L(s) = R_{PI}(s) * G(s) = \left(k_p + \frac{k_i}{s}\right) * \left(\frac{1}{As + B}\right)$$

$$F(j\omega) = \frac{\left(k_p + \frac{k_i}{s}\right) \left(\frac{1}{j\omega A + B}\right)}{1 + \left(k_p + \frac{k_i}{s}\right) \left(\frac{1}{j\omega A + B}\right)} = \frac{j\omega k_p + k_i}{j\omega(k_p + B) + k_i - \omega^2 A} \quad (\text{Eq. 2.5-6})$$

Applying equality between the square module of the first member and  $\frac{1}{2}$ :

$$2k_i^2 + 2\omega^2 k_p^2 = \omega^2(k_p + B)^2 + (k_i - \omega^2 A)^2$$

$$2k_i^2 + 2\omega^2 k_p^2 = \omega^2 k_p^2 + \omega^2 B^2 + 2\omega^2 + k_i^2 - 2\omega^2 k_i A + \omega^4 B^2$$

$$k_i^2 + 2\omega^2 k_i B + \omega^2 k_p^2 - \omega^2(B^2 + 2k_p B) - \omega^4 B^2 = 0$$

$$k_{i1,2} = -\omega^2 A \pm \sqrt{\omega^4 A^2 + \omega^2(B^2 + 2k_p B - k_p^2) + \omega^4 A^2}$$

$$k_{i1,2} = -\omega^2 A \pm \omega \sqrt{2\omega^2 A^2 - B^2 + 2k_p B - k_p^2}$$

$$k_i \in \text{Re} \rightarrow k_{i1,2} = -\omega^2 A + \omega \sqrt{2\omega^2 A^2 - B^2 + 2k_p B - k_p^2}$$

$$k_i > 0 \rightarrow 2\omega^2 A^2 - k_p^2 + B^2 + 2k_p B > \omega^2 A^2$$

$$\omega^2 A^2 - k_p^2 + B^2 + 2k_p B > 0$$

$$k_{p1,2} = B \pm \sqrt{2B^2 + \omega^2 A^2}$$

$$k_{pmin} = B - \sqrt{2B^2 + \omega^2 A^2} < k_p < k_{pmax} = B + \sqrt{2B^2 + \omega^2 A^2} \quad (\text{Eq. 2.5-7})$$

Since  $k_p$  must be positive than  $k_{pmin} > 0$  and if all assumptions are met, the higher the value of  $k_p$ , the greater the phase margin  $\phi_c$ . This means greater stability of the system.

These equations provide an understanding of one of the different ways to calibrate a PI controller. A MATLAB file was created in which there is an algorithm that follows the previous equations. From the bandwidth, it calculates a few different values between the minimum and maximum  $k_p$  and for each the corresponding  $k_i$ . These are entered into the closed-loop Laplace equation  $F(s)$ . Using the Bode and Nyquist graphs, the best gain values to use in the PI are chosen. It is worth mentioning that the four current regulators have the same parameters, so the calculation is only performed once for each of them.

There is a problem with the PI controller that only concerns the I term. In a case where the integral action combined with the limitation due to the actuator could drastically

reduce the performance of the controller. This phenomenon is called “windup”. In the next scheme, we use as an example a pure integrator with the actuator which limits the integral output between  $-u_M$  and  $+u_M$ [10].

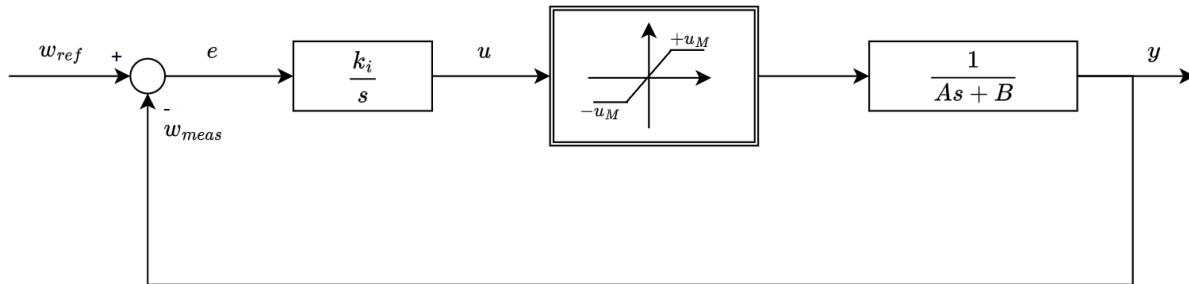


Figure 2.5-4 : Integrator and Actuator

It occurs when the input error has the same sign for a certain period of time. In this process, the state of the integrator increases continuously even though it is limited by the actuator. But when the error changes sign, it is necessary to wait until the state reaches a value below the actuator limit. In practice, the integrator action must be unloading, and it will be done by an anti-windup system. Several schemes exist to limit this problem. The one adopted in this project was chosen because it is easy to implement in the microcontroller[11] and due to this will be seen in detail in the Chapter 2.6.

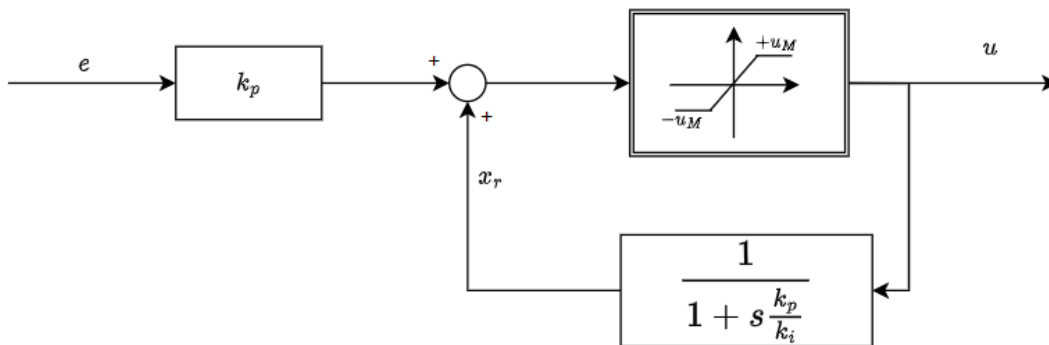


Figure 2.5-5 : Block scheme of the anti-windup system

## 2.6. Microcontroller and Inverter

The key part of the project is the microcontroller. It will become the brain which is able to decide how to run the motor and the current according to the need. The one used is the Texas Instrument F28379D. The choice is slightly forced since Typhoon HIL has a connection board designed for a limited number of devices. But it is one of Texas Instrument's

best microcontrollers. There are several features that must be studied to be an expert on the subject. One of the board's strengths is the number of pinouts available. There are twelve exposed ePWM pins to control the two inverters. Nine ADC pins are available to read

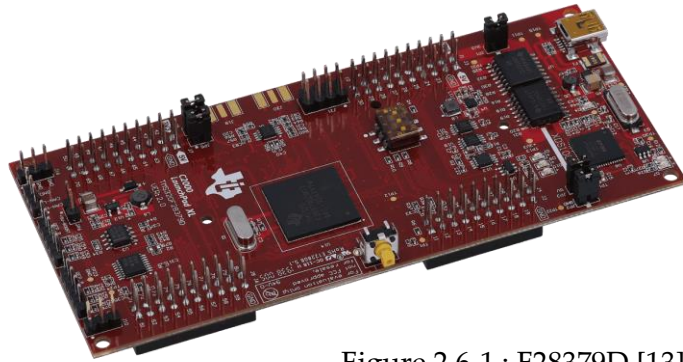


Figure 2.6-1 : F28379D [13]

a good number of variables. In the end, it is essential

to say that the performance of it is very powerful, in particular it has a clock of 200 MHz which is much higher than we need. It could be exploited in a future project. In this subsection, we will focus on these peripherals to learn how the interface between the motor and the controller works.

### 2.6.1. PWM and Inverter

PWM (Pulse Width Modulation) is a useful technique for managing the gates of IGBTs into an inverter. The peripheral inside the microcontroller creates a digital signal (0 or 1, corresponding to 0[V] and 3.3[V]) on the output pins that changes at a certain frequency over a certain period. In addition, it is possible to modify the time at which the change occurs and control it using a reference signal. What is the switching point and how to find it? The theoretical method consists of using a triangular signal ranging from [-1,1] called the carrier and a reference signal called the fundamental. The carrier forms a bounded period between two consecutive values of -1. At the point where the carrier and fundamental intersect, the PWM is commanded to switch. In this way is possible to open or close the IGBTs and control the voltage at the load. To discuss in detail what the input/output of an inverter is, we will refer to a single leg inverter [13].



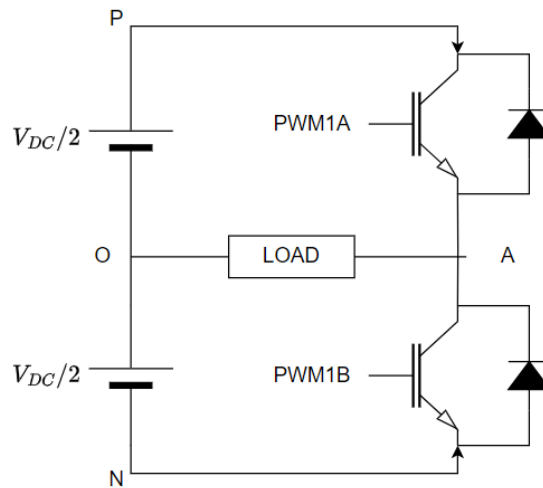


Figure 2.6-2 : Single Leg Inverter [13]

The method to control the IGBTs state depends by the position between the fundamental and the carrier signals. Moreover, the IGBTs must be at different status because if they are both close, a short circuit occurs. Instead, if they are both open, we cannot know which is the voltage of the point A.

The main rules are:

$$v_{AO} = v_{AN} - \frac{V_{DC}}{2}$$

$$\text{When } v_{fund} \geq v_{carr} \rightarrow \begin{matrix} PWM1A \text{ is ON} \\ PWM1B \text{ is OFF} \end{matrix} \rightarrow v_{AN} = V_{DC} \rightarrow v_{AO} = \frac{V_{DC}}{2} \quad (\text{Eq. 2.6-1})$$

$$\text{When } v_{fund} < v_{carr} \rightarrow \begin{matrix} PWM1A \text{ is OFF} \\ PWM1B \text{ is ON} \end{matrix} \rightarrow v_{AN} = 0 \rightarrow v_{AO} = -\frac{V_{DC}}{2}$$

The next figures show how the microcontroller makes its decisions based on the principal rules.

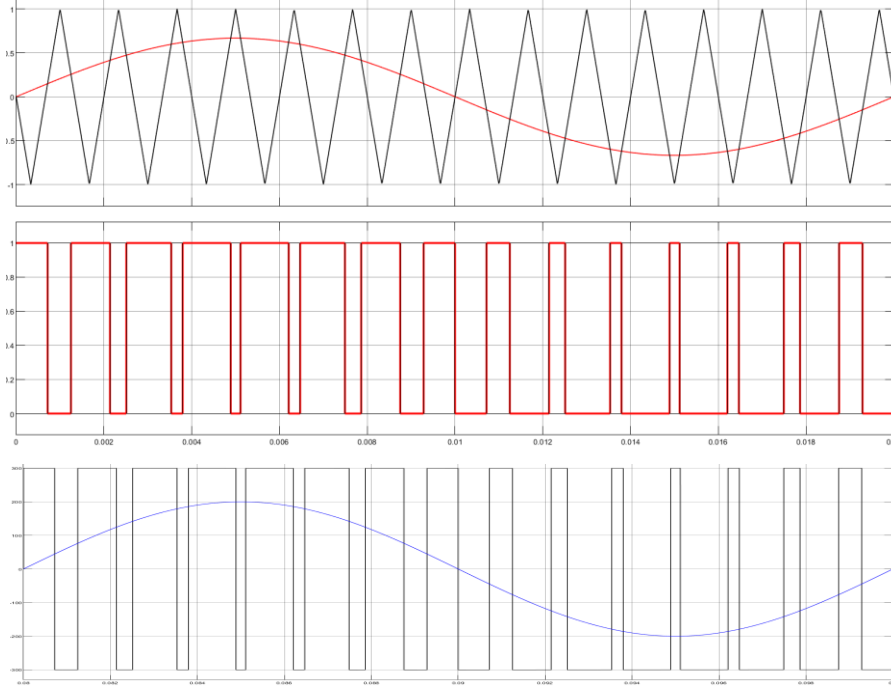


Figure 2.6-3 : Fundamental and Carrier signals(up), PWM1A and PWM1B (middle),  $v_{A0}$  and  $v_{A01}$ ( down) [13]

In reality, as can be seen in the figure above, the fundamental does not reach the maximum value of the carrier. This is reflected in  $v_{A01}$ , which is the fundamental harmonic of  $v_{A0}$ . It is the main feature to control the inverter and the output voltage. Practically speaking, if we can modify the amplitude of the fundamental signal, we can control the amplitude of the first harmonic. This is done using a coefficient called the modulation ratio:

$$m_a = \frac{\widehat{V_{fund}}}{V_{carr}} \leq 1$$

And from [13]:

$$v_{A01}(t) = \frac{V_{DC}}{2} * \frac{v_{fund}(t)}{\widehat{V_{carr}}} \quad (\text{Eq. 2.6-2})$$

Moreover, there is also a frequency modulation ratio:

$$m_f = \frac{f_{carr}}{f_{fund}} \quad (\text{Eq. 2.6-3})$$

The  $f_{carr}$  is equal to the switching frequency  $f_{sw}$  which activate IGBTs.  $m_f$  is useful to find the harmonics created with PWM method. They are concentrated in [13]:

$$f_h = j * f_{sw} \pm k * f_1 = (j * m_f \pm k) * f_1 \quad (\text{Eq. 2.6-4})$$

How does PWM work in practice inside the microcontroller? The PWM peripheral has a counter inside which starts from zero and counts up to its maximum value at each

clock strike. When it reaches the limit value, the counter drops to zero counting backwards and starts again. If we plot this count as a function of time, we can create a triangular waveform formed by steps as in Figure 2.6-4. What we want is a triangular waveform as close as possible to the theoretical one. The problem introduced is that the counter cannot use negative values. For this reason, the fundamental signal used to create the reference waveforms must be scaled and shifted to meet this constraint.

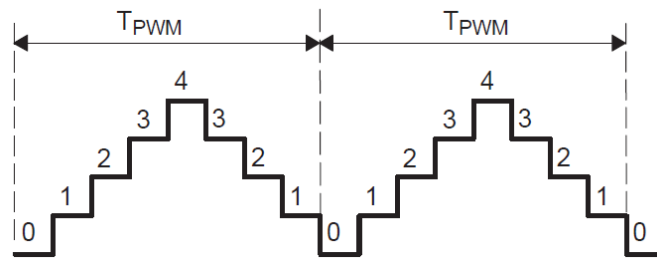


Figure 2.6-4 : Up-Down count inside the PWM peripheral [12]

Using some simple formulas described in the technical data of the F28379D [12], it is possible to set all the parameters within the PWM peripheral to create the waveform with the desired characteristics, such as switching frequency and duty cycle. In the Figure 2.6-5 there is an example of what happens on the PWM pins output by setting as reference a different value of the register CMPA. Actually, the duty cycle in our project is not constant but change dynamically as seen in the Figure 2.6-3. For this reason, it is necessary to handle this peripheral carefully, especially when the inverter is working with high voltages, in order to avoid any faults and damage to the devices.

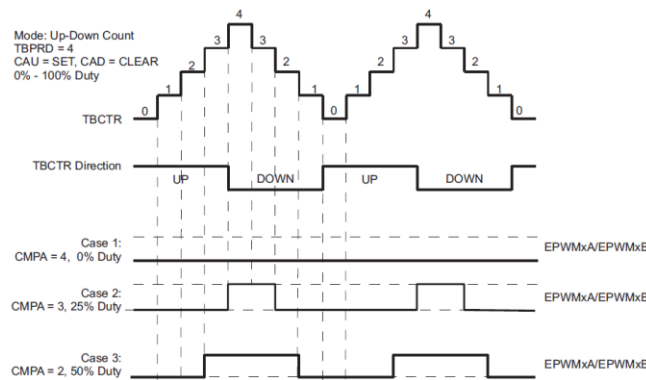


Figure 2.6-5 : Duty Cycle [12]

It is crucial to remember that IGBTs cannot switch off instantaneously. For this reason, it is necessary to wait a period called “death time” between the switching off of one IGBT in the leg and the switching on of the other to avoid a short circuit. The value of this time for an IGBT is about a couple of microseconds, but by changing a register within the microcontroller it is possible to manage and change it while it is running. In our project it will be set to  $2\mu s$ .

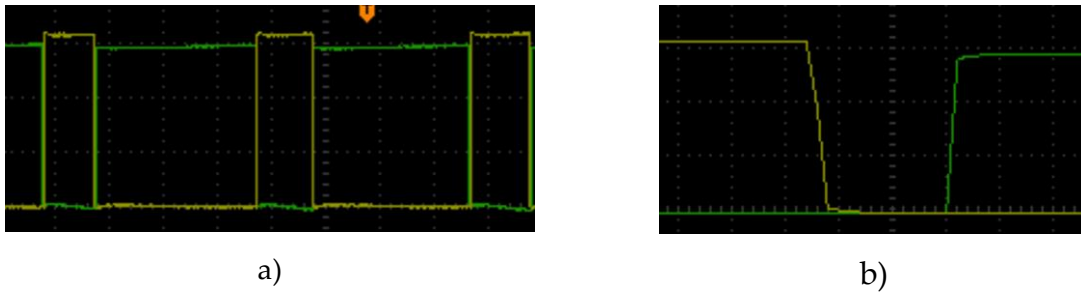


Figure 2.6-6 : PWM signal (a) and Death Time of 2us(b)

### 2.6.2. ADC

The acronym ADC stands for analogue-to-digital converter. Its function is the conversion of an analogue signal to a digital value within the microcontroller. The F28379D could read signal between 0[V] to a maximum of 3.3[V], but the datasheet [12] suggests to don't overcome 3[V]. This data comes directly from the Typhoon HIL hardware via dedicated pins. Within this, the variables could have very different values than the range imposed on the microcontroller, for example the current should reach a maximum of 200[A]. For this reason, all data must be converted using a divider and an offset. The divider allows the actual value to be scaled to a very small value. The offset, on the other hand, allows negative values to be read in. In the end, the controller must convert in the opposite way and reconstruct the real one. There are some crucial parameters to be read and they are shown in the Figure 2.4-3, such as the currents, the angle value, and the voltages on the sources.

The formula followed by Typhoon HIL is:

$$x = \frac{X}{divisor} + offset \quad x \in [0,3] \quad (\text{Eq. 2.6-5})$$

Where  $X$  is the real value, and  $x$  is the scaled one

For example, the current  $i_{d2}$  has a maximum value of  $\pm 200$ [A] since is sinusoidal. The next equations are useful to evaluate the value of the divider and the offset.

$$\begin{aligned} 0 &= \frac{-200}{divisor} + offset \\ 3 &= \frac{200}{divisor} + offset \end{aligned} \quad (\text{Eq. 2.6-6})$$

$$\begin{cases} divisor = 133 \\ offset = 1.5 \end{cases}$$

In reality, the actual divisor is higher than the calculated one, about 30% higher, as there could be a lot of disturbances and also some unwanted peaks. It loses precision but is more effective in seeing the real behaviour of the variable.

### 2.6.3. Sample Time and Execution Time

Like a real brain, the inputs and outputs received by the microcontroller must be organised and executed in a certain order. The code within it has been modified in the course of the project. It is crucial to focus on the time in which actions are performed, as a correct and harmonious flow of functions could increase the power and optimisation of the process. For this reason, the sample time becomes a crucial part suited to reach our aims.

Our microcontroller is one of the best around as it can operate at 200[MHz]. This means that each line of code can be executed in 5ns, a very short time but useful for a future implementation. We set the clock to 100[MHz] and, using a timer, created a cycle in which all actions are executed. This time is directly related to the sampling time, the period in which data can be read from the outputs of the HIL hardware. It was decided that the sampling rate is 10[kHz], so 100us for each reading. Therefore, it was possible to run  $100[\text{MHz}]/10[\text{kHz}] = 10,000$  clock shot. At the beginning of the project, this seemed a very high amount, but it became a bit tight. In actual fact, studying the datasheet, a function was discovered within the microcontroller that should be activated by the settings. This fantastic parameter makes it possible to reduce the weight of the code during compilation. Eventually, the clock number for cycle execution becomes between 2 and 3 thousand.

What really happens in the microcontroller is a cycle in which the actions of the control scheme are performed:

- The sensors measure all the variables such as currents voltages and mechanical angle
- The speed reference is set
- The measured phase currents are converted by using Clark and Park to the direct and quadrature currents for each winding
- The PI controller of the speed calculates the torque reference  $T_e$
- The power sharing algorithm decides how much quadrature current should be send to the motor
- All the four PI controllers of the currents are performed until the voltages on direct and quadrature axes for each winding are calculated
- The  $d - q$  voltages are converted again into the phase reference voltages
- By using the voltage references, the PWM are controlled to act on the inverters
- The cycle repeats every  $0.1\text{ms}$

In summary, there are two different peripherals that have to work together. The algorithm within the microcontroller is the brain that decides, depending on the speed reference, how to power the DTPMSM both as a motor and a generator.

### 2.6.4. Z-domain and Discretize domain

As mentioned before, the microcontroller restarts its cycle every  $0.1[ms]$ . This, combined with the fact that precision is not infinite, implies that mathematical operations cannot be performed in continuous time but must be done by discretising. This term denotes the process of transforming variables from continuous to discrete, that is taking values at regular intervals. It denotes the working principle of a real regulator.

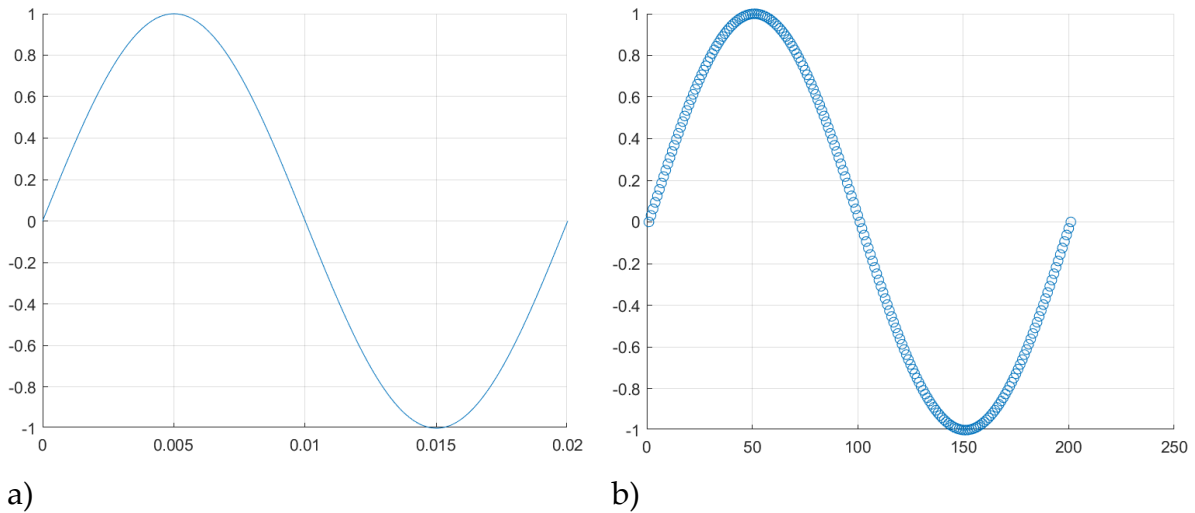


Figure 2.6-7 : Sinusoidal waveform in Continuous Time(a) and in Discrete Time(b) after sampling

Figure 2.6-7 shows the main difference between a continuous-time waveform and a discretised one. The latter is mainly created by a sequence of samples taken every fixed time. This time can be chosen according to the performance of the microcontroller, for example in our project the sampling time is  $T_s = \frac{1}{f_s} = \frac{1}{10[kHz]} = 0.1[ms]$  which means that each  $T_s$  we acquire a sample of the variables we want to manage. With this sequence of samples, it is possible to analyse and handle the data, for instance perform a Fourier transform and analyse the frequencies or even detect the phase angle of an electrical system.

From a mathematical point of view, the transformation of the continuous-time functions to discrete-time function is carried out using the Z-transform, which makes it possible to move from the Laplace domain to the realisation of a digital model. The theoretical explanation is described into [11]. The interesting point is the transformation from the Laplace domain to the discretised one. By using the Tustin's method, the  $s$  variable is defined as:

$$s = \frac{2z - 1}{T_s z + 1} \quad (\text{Eq. 2.6-7})$$

For example, a normal integrator in Laplace  $y(s) = \frac{1}{s} * u(s)$  becomes

$$y = \frac{T_s z + 1}{2 z - 1} u$$

$$2(z - 1)y = T_s(z + 1)u \tag{Eq. 2.6-8}$$

$$2zy - 2y = T_s zu + T_s u$$

Dividing both the member by  $z$

$$y = \frac{T_s}{2} u(1 + z^{-1}) + yz^{-1} \tag{Eq. 2.6-9}$$

By using the sample

$$y_n = \frac{T_s}{2} (u_n + u_{n-1}) + y_{n-1} \tag{Eq. 2.6-10}$$

This last equation means that the output of an integral equation at a given time depends on the sampling time  $T_s$ , the average value between the instantaneous input sample and the previous one, and the previous output. This example encapsulates the essence of what is essential to know about the transformation.

What we are interested in, it is the discretized equation and the sample signal for the PI controller with the anti-windup function. Considering the Figure 2.5-5, the integrator block is [11]:

$$R_I(s) = \frac{1}{1 + s \frac{k_i}{k_p}} \tag{Eq. 2.6-11}$$

Applying the Tustin transformation:

$$R_I(z) = \frac{1}{1 + \frac{2}{T_s} \frac{z - 1}{z + 1} \frac{k_i}{k_p}} = \frac{(1 - b) \left( \frac{1}{2} z + \frac{1}{2} \right)}{z - b} \tag{Eq. 2.6-12}$$

$$b = 1 - \frac{k_i T_s}{\frac{1}{2} k_i T_s + k_p} \tag{Eq. 2.6-13}$$

Moreover:

$$g = \frac{1}{2} (1 - b) \text{ and } h = \left( 1 - \frac{1}{2} (1 - b) \right) (1 - b) \tag{Eq. 2.6-14}$$

To sum up:

$$R_I(z) = g + \frac{h}{z - b} \tag{Eq. 2.6-15}$$

The new block scheme of the PI becomes different from the previous. The positive retroactive splits into two new blocks.

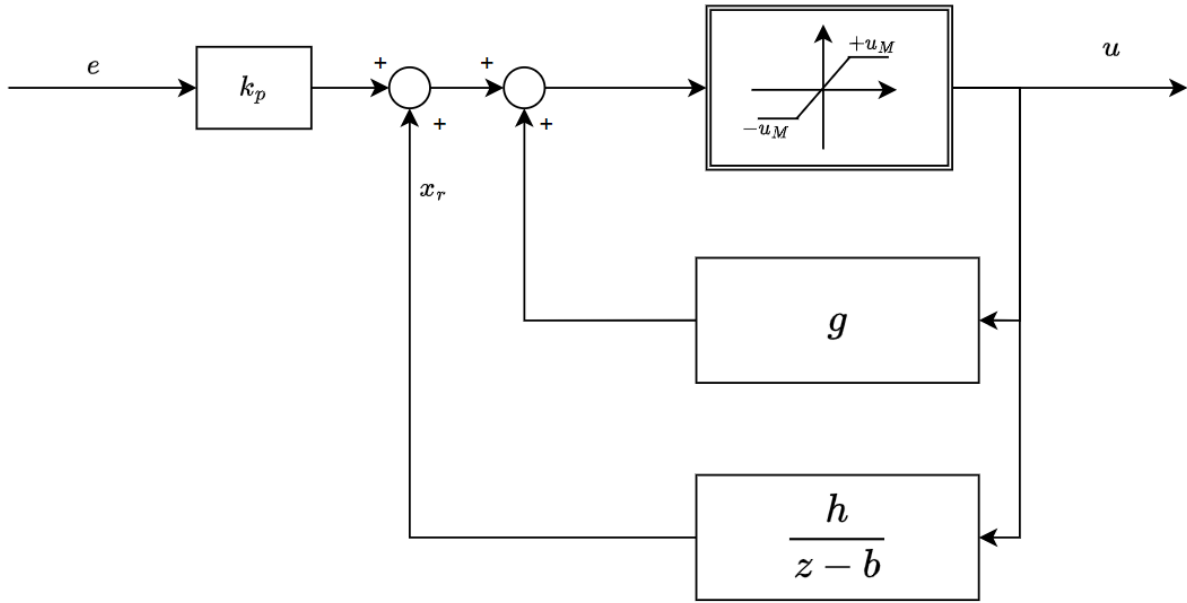


Figure 2.6-8 : Split  $R_I(z)$

By performing a few manipulations of the diagram, it changes again to the diagram in the Figure 2.6-9.

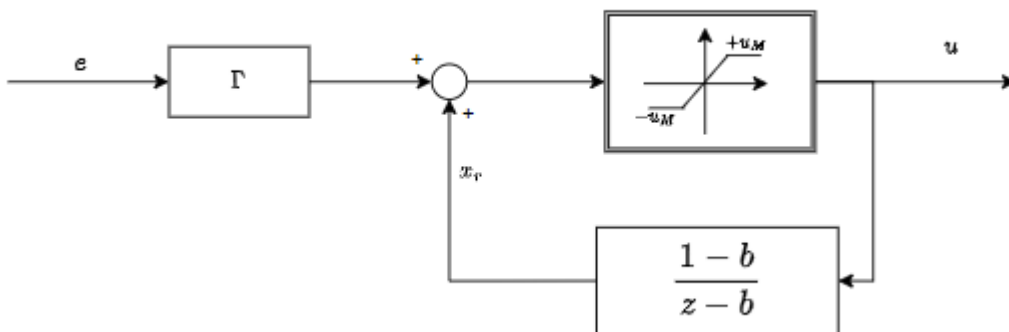


Figure 2.6-9 : Final configuration of PI with Anti-Windup

Where:

$$\Gamma = \frac{1}{2}T_s k_i + k_p \tag{Eq. 2.6-16}$$

After some calculation following the transformation from Laplace to discrete time domain, we obtain:



$$x_r(z) = \frac{1-b}{z-b} u(z) \quad (\text{Eq. 2.6-17})$$

That means:

$$x_{r_n} = bx_{r_{n-1}} + (1-b)u_{n-1} \quad (\text{Eq. 2.6-18})$$

The implementation of this block diagram in the microcontroller is simple. The only problem is how to write the actuator return function taking feedback into account.

The algorithm is described as follows.

---

Algorithm 1: PI with anti-windup

---

- 1: Calculation of  $\Gamma$  and  $b$
  - 2: Computation of  $x_{rn}$  for every sample
  - 3: Application of the actuator limits
  - 4: Sum of  $\Gamma$  to  $x_{rn}$
  - 5: Application of the actuator limits again
  - 6: Repeat every  $T_s$
-



## 3 Open Loop Approach

This chapter is the first that covers what we did to build our project. It represents the fundamental point to start analysing all the necessary features. From here, we will put together a series of information needed to understand how each block of the new configuration works. In particular, we will discuss the difference between PC simulation alone and the hardware-in-the-loop technique. The process will allow us to study each individual element that makes up the final configuration. It is therefore a good idea to start with the simplest one and gradually progress to the most recent and complete one.

### 3.1. Single Leg Inverter and RL load

We have just seen the theory of this part in section 2.6. As a first step, it is useful not only to understand how an inverter works, but also what is the crucial part to focus on and improve as much as possible.

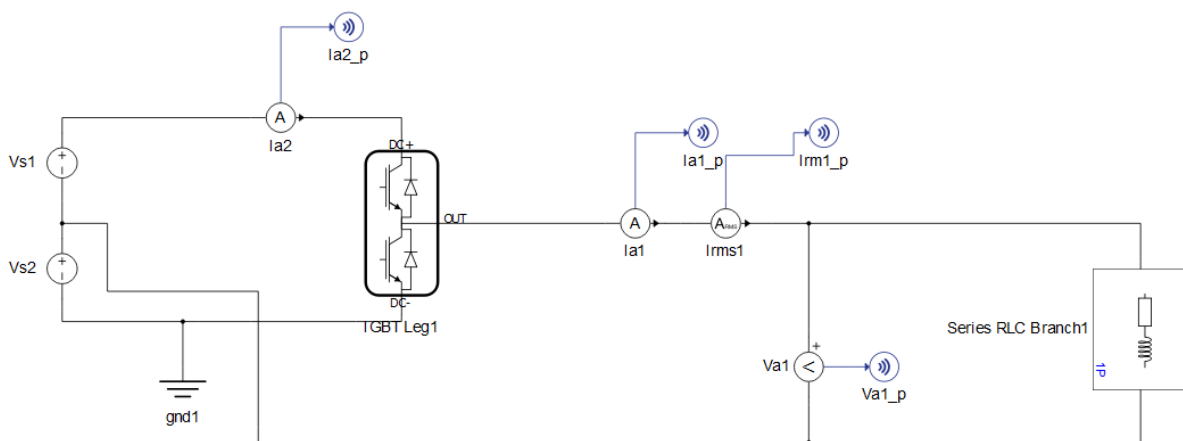


Figure 3.1-1 : Typhoon HIL Electric Scheme Single Leg Inverter

The actual complete configuration has two non-ideal DC sources. At this point, however, the sources must be ideal, as the main objective of this part is to analyse the inverter output for a generic RL load. ( $R_s = 10 [\Omega]$ ,  $L_s = 10[mH]$ ,  $V_{s1} = V_{s2} = 750 [V]$ ).

In addition, the inverter's IGBT switching frequency is set to  $f_{sw} = 5[kHz]$  for all tests. A higher switching frequency is not necessary for our purpose, since  $5[kHz]$  sufficient for good results.

In general, a higher switching frequency helps filter out harmonics. The limit in increasing the  $f_{sw}$  is related to the power of the system: the higher the power, the lower the switching frequency must be. This is because the current increases as a function of power and the value of the current ripple  $I_{pp}$  also increases. In fact, the current ripple is due to the inductance and  $v_L = L \frac{\Delta}{\Delta t} i = L \frac{I_{pp}}{\Delta t}$ ;  $v_L$  is related to the source voltage, which does not change (for a certain power range). If  $I_{pp}$  increases, then  $\Delta t$  also increases and the period of the current ripple increases accordingly. Thus, under steady-state conditions, the period  $\Delta t$  corresponds to the switching period  $T_{sw}$ . If  $T_{sw}$  increases,  $f_{sw} = \frac{1}{T_{sw}}$  must decrease. Furthermore, if the switching frequency increases, losses increase in proportion to  $f_{sw}$ . These problems, especially the last one, could limit the switching frequency.

Based on these assumptions, an approach is made to obtain a sine wave with a fundamental frequency of 50[Hz] using the PWM method.

Since we are using a Voltage Source Inverter (VSI) it is important to look at the voltage on the load and its harmonics. In the next, "HIL" will indicate results taken from the HIL technique and "SIM" will declare the simulation only. They are both performed by Typhoon and all the data are extracted and managed by MATLAB.

There are many passages to focus on, we are starting from the reference signals.

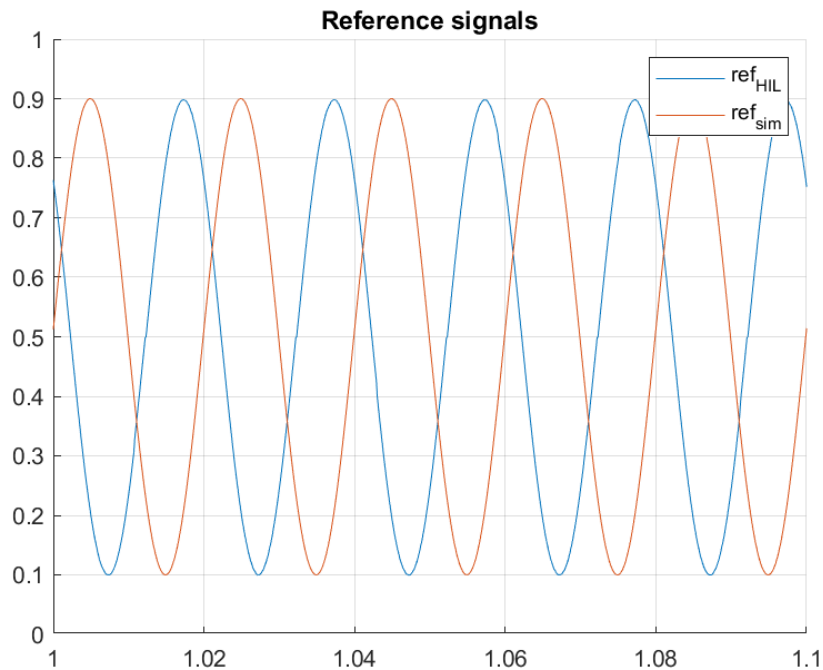


Figure 3.1-2 : Reference Signals Single Leg HIL vs SIM

Figure 3.1-2 shows the reference signals representing the behaviour of the voltages in the HIL and SIM modes. They do not coincide but are shifted by an undefined value because we want to highlight the differences and it is not necessary for the two signals to overlap. What is crucial to understand is the frequency and amplitude of both. They have a period  $T = 20[ms]$  which means a fundamental frequency  $f_1 = 50[Hz]$ .

Furthermore, their amplitude is between 0.1 and 0.9. This test is carried out with a modulation factor  $m_a = 0.8$ , but since our reference must be contained within a range [0-1], the references are shifted and scaled according to the theory. The formula that handles the two sinusoidal waveforms is the same:

$$ref = \frac{m_a * \sin(\omega t) + 1}{2} \tag{Eq. 3.1-1}$$

The latter formula, intersected with the triangular carrier wave, creates the PWM signal required to produce a voltage that follows the wanted sinusoidal reference. However, the voltage we see in Figure 3.1-3 does not have the desired shape of the reference signals, but rather resembles a square wave that varies in time (such as a variable duty cycle). This is what is actually expected from the theory

(Eq. 2.6-1 ). The voltage fluctuates between  $\pm 750[V]$  for each step due to the position of the load between the midpoint of the leg and the midpoint of the source junction. The figure is taken from the simulation result and only takes into account 100 commutations (20[ms] simulation interval with  $f_{sw} = 5[kHz]$ ).

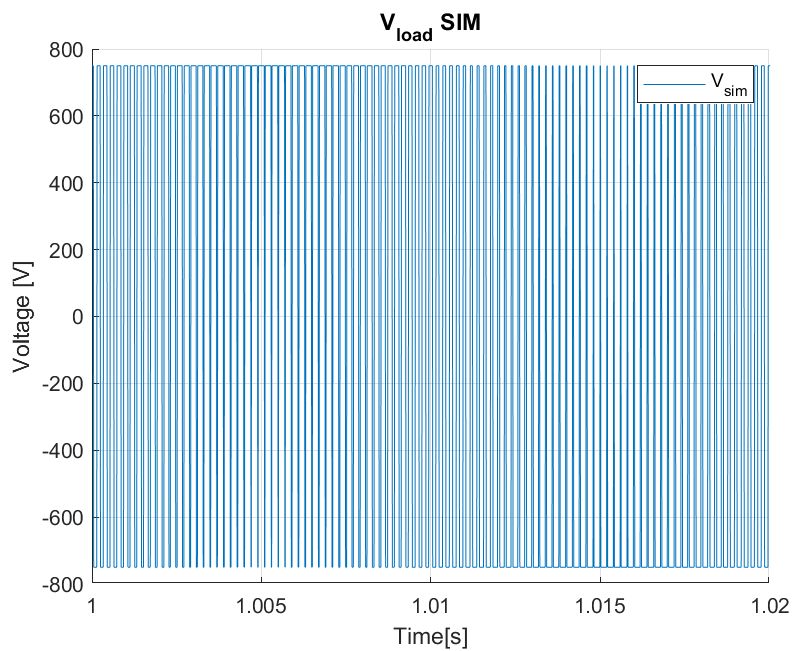


Figure 3.1-3 : SIM Voltage on RL load

To better understand what is going on, however, it is correct to check the harmonics within this square wave. Using the Fast Fourier Transform (FFT), it will be possible to extract the full harmonic content of the square wave.

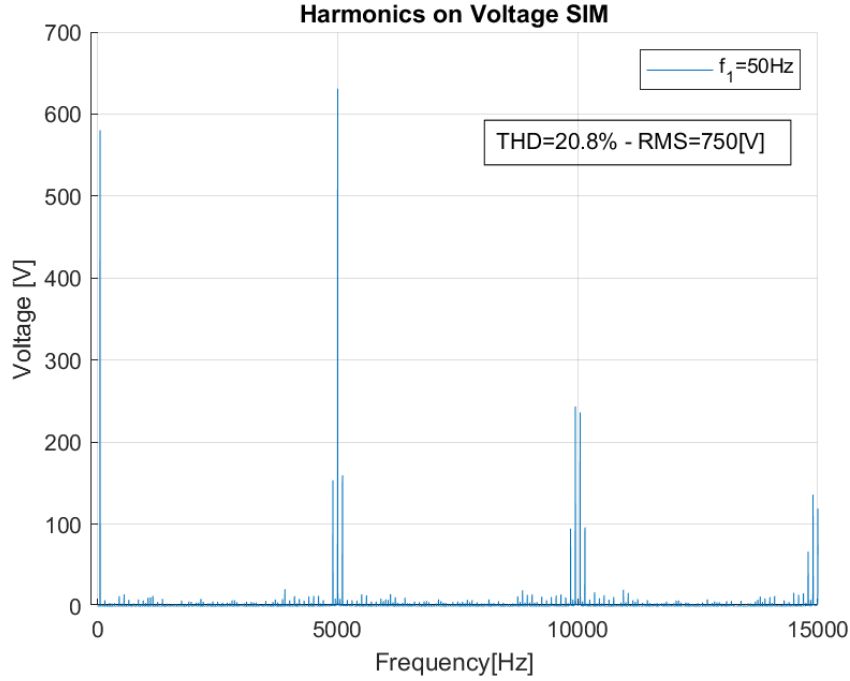


Figure 3.1-4 : Harmonics content in the SIM voltage

From Figure 3.1-4, several information could be extracted. The harmonics content follows the (Eq. 2.6-4 ) in which the first harmonic is on the fundamental frequency  $f_1 = 50[Hz]$ . Instead, the other are positioned at multiple of  $m_f$  surrounded by minor harmonics. For instance, since  $f_{sw} = 5[kHz]$ , the first harmonics set is on  $5[kHz]$  the second at  $10[kHz]$  . Furthermore, since the harmonic content makes a crucial contribution to the first, as the voltage is not sinusoidal, it becomes essential to calculate the RMS and THD values.

The RMS (Root Mean Square) can be defined as the value of DC variables which produces the same power in a resistive load or the measure of imperfection taking in care all the harmonics. It represents a value for comparing different waveforms. It can be calculated by:

$$x_{RMS} = \sqrt{\frac{1}{N} \sum_{n=1}^N |x_n|^2} \quad (\text{Eq. 3.1-2})$$

The THD (Total Harmonic Distortion), on the other hand, indicates how much harmonics affect the fundamental. It can be calculated using:

$$THD = \frac{\sqrt{\sum_{n=2}^N |x_{nRMS}|^2}}{x_{1RMS}} \quad (\text{Eq. 3.1-3})$$

From the harmonics content, the THD of the voltage in the SIM is about 20% and the RMS is 750[V]. These values are interesting as the THD is not so low and the RMS is

close to the DC voltage sources. Attention must be paid to the fact that this is not a sine or square waveform, in fact the amplitude of the first harmonic is 582[V].

Another fundamental piece of information is the amplitude and phase of the first harmonic of the voltage. To obtain this waveform, a low-pass filter must be applied to the wave Figure 3.1-3.

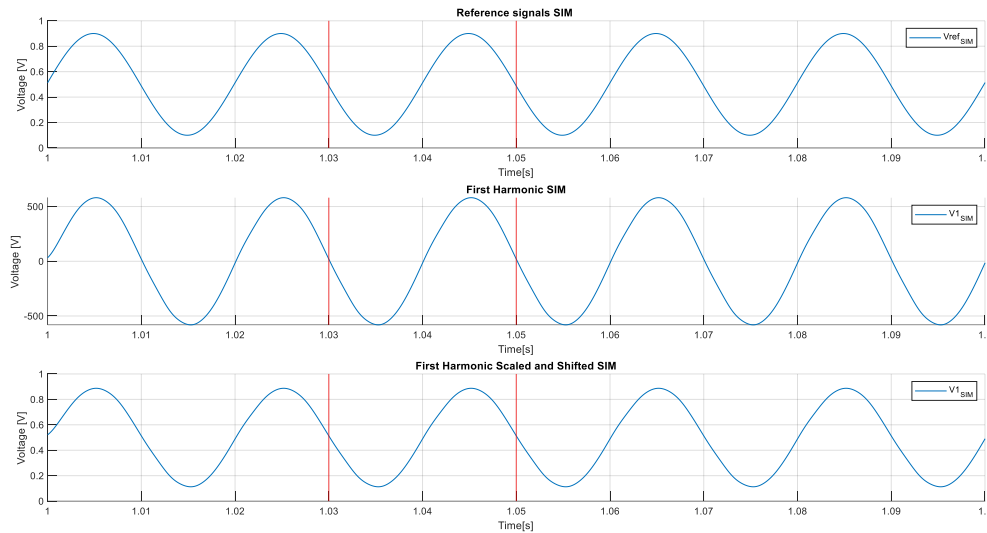


Figure 3.1-5 : Reference signal, first harmonic, first harmonic scaled and shifted

In the Figure 3.1-5, the reference signal and the low-pass filter of the square wave are plotted. It is evident that they are in phase. The red brackets delimit a period, and it is clear that the amplitude value is the same for each plot. The last chart represents the low pass filtered voltage but scaled by 750[V] and shifted by 1. It has the same behaviour as the reference signal.

The actual voltage at the load  $v_{AO}$  is a stepped waveform, not a sinusoidal one. How can we say that the inverter obtains sinusoidal AC? Actually, in a voltage source inverter (VSI) what is sinusoidal is the current, not the voltage. In fact, they are used with inductive loads and the inductance applies a filtering effect which causes a sinusoidal shape to the current. This is why a filter could be required at the output of the inverter, usually the motor could perform such as an inductive filter. We can try to give a look to the current waveform.

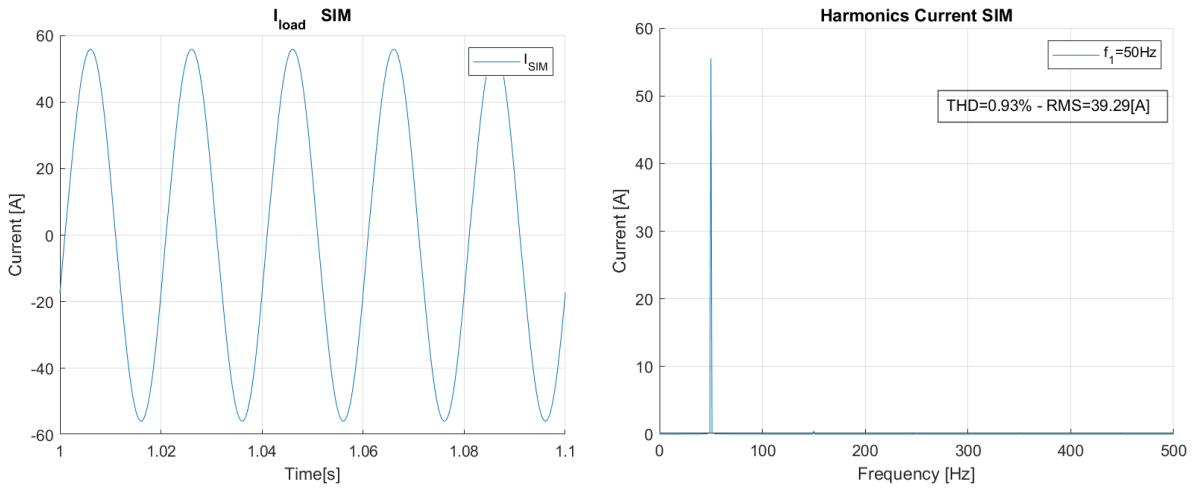


Figure 3.1-6 : Current in the load SIM and its harmonic content

This current appears surprisingly regular and sinusoidal, as it respects exactly 5 periods in 0.1[s]. This is also confirmed by the harmonic content, where the fundamental is at 50[Hz]. However, other harmonics appear with a very low amplitude. Since it is a single leg, odd harmonics such as the 3rd, 5th and 7th are present. The THD is very low, indicating that the odd harmonics do not have a strong contribution. Furthermore, by performing some calculations, a relationship between the first harmonic of voltage and current can be seen.

$$\begin{aligned}
 I_1 &= \frac{V_1}{Z_l} = \frac{\frac{582[V]}{\sqrt{2}}}{\sqrt{10^2 + (2\pi f_1 * 10 * 10^{-3})^2}} \approx 39.26[A] \approx \\
 &\approx \frac{I_{1max}}{\sqrt{2}} = \frac{55.4896[A]}{\sqrt{2}} \approx 39.24[A]
 \end{aligned}
 \tag{Eq. 3.1-4}$$

That correspond to about the RMS value of the first harmonic.

Using the HIL technique, we want to obtain a voltage with the first harmonic with the same amplitude and frequency as the SIM simulation. We also expect the presence of the odd harmonics on the current.



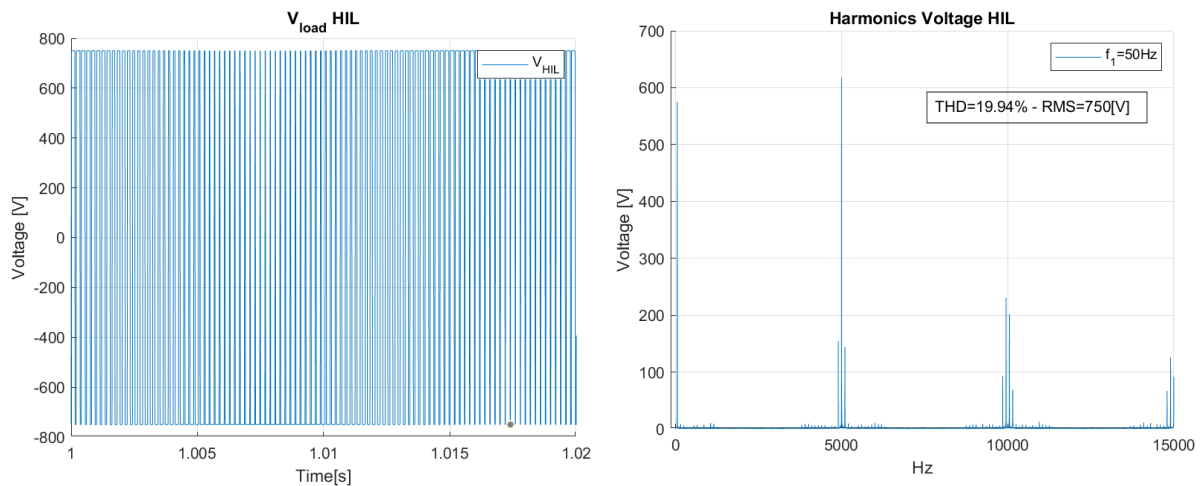


Figure 3.1-7 : Voltage on the Load and its harmonic content HIL

There are several points to focus on. The first concerns the THD, which is a little bit lower than in SIM mode, but in the same range. It means that harmonics contribute 20% of the maximum value of the fundamental. The RMS is the same as before.

The most interesting aspect to study is the amplitude of the first harmonic and the order of the others. Since we are using a synchronous PWM ( $m_f \in Integer$ ), we expect the first-order harmonics to be exactly 5[kHz]. According to the theory in (Eq. 2.6-4), for odd values of  $j$ , harmonics only exist for even values of  $k$ . For even values of  $j$ , harmonics only exist for odd values of  $k$ . [13]

Another crucial aspect is the position of the first harmonic respect to the reference signals. Figure 3.1-8 shows that the first harmonic follows the reference signal, with the same imposed frequency  $f_1$ .

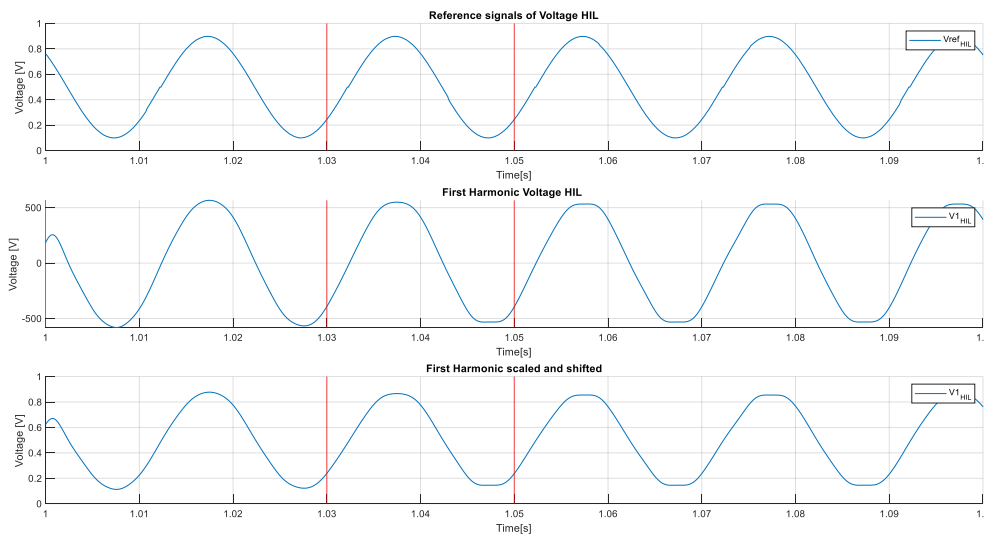


Figure 3.1-8 : Reference Signals, First Harmonic and First Harmonic Scaled and Shifted

It is even essential to observe the current in the load. Figure 3.1-9 shows that it looks like a perfect sine waveform at 50[Hz]. It has a very low THD, 0.4% higher than the HIL mode, which indicates that the presence of harmonics is roughly negligible.

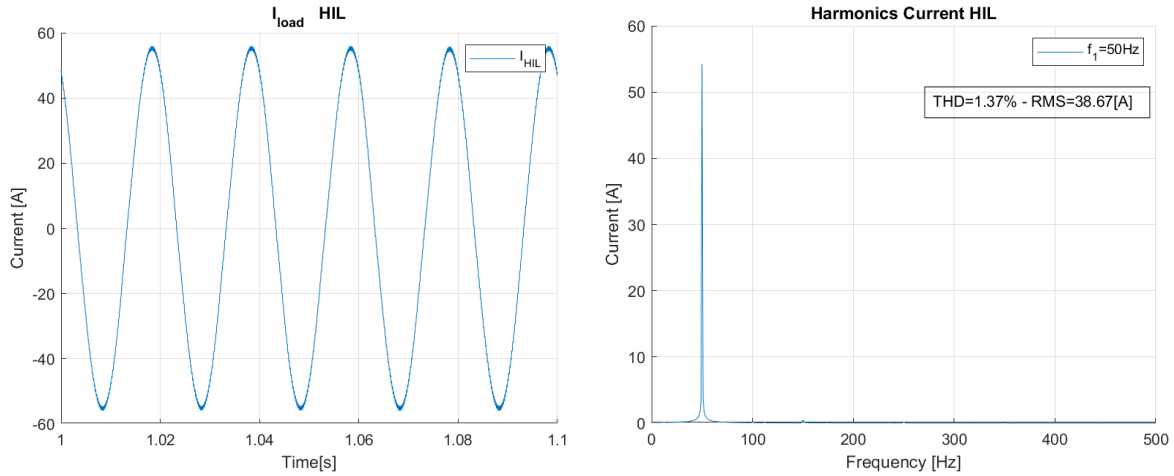


Figure 3.1-9 : Current on RL load and Harmonic content

In conclusion, we can say that the PWM method of the HIL works well, and it is possible to obtain a good approximation to simulation. This is what we are trying to achieve in order to validate our results. The first test with an RL load was carried out with a single-leg inverter that does not correspond to our final configuration, but only covers one third of it. but what we can deduce is that an entire inverter could work optimally, and this is what we will analyse in the next sections.

## 3.2. Three-phase inverter with RL load

The next step in understanding each stage is the analysis of a three-phase inverter with an RL load. This is a fundamental part of the project, as the purpose of this test is to see if the microcontroller can also handle a more complex condition in which better microcontroller performance is required. Just consider that the final configuration requires the use of two inverters with nice performance. The setup is not so different respect the single leg inverter. The three-phase inverter can be considered as a combination of three single-phase inverters. The load is in a star configuration and the centre point of the legs is connected to it. The configuration used for this test is reported in the Figure 3.2-1. It is the simplest scheme available for performing the simulation and acquiring the measurement to be studied.

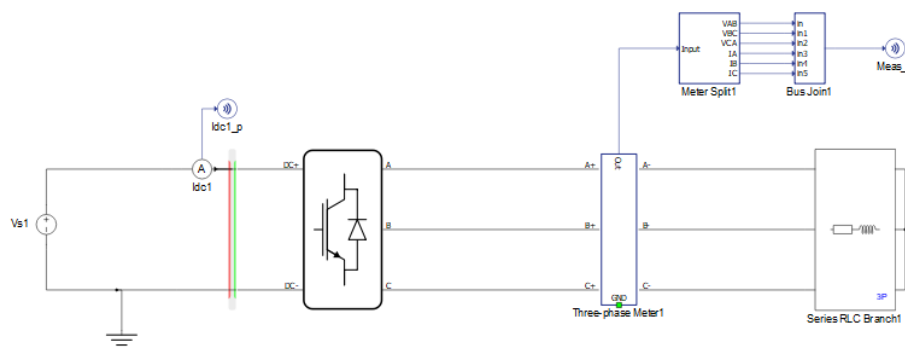


Figure 3.2-1 : Three-phase Inverter with RL load

If we expand the inverter, it consists of three different legs. It should be remembered that each leg has two IGBTs that must neither be open nor closed at the same time.

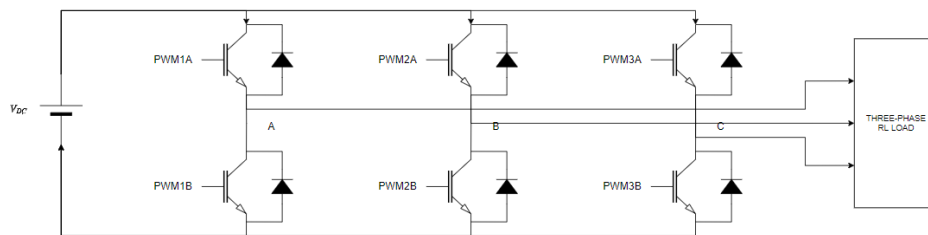


Figure 3.2-2 : Three legs for a three-phase inverter

Each leg could be controlled individually, but since we want to achieve a symmetrical, three-phase system, they will be fed by three reference signals that are  $120^\circ$  out of phase with each other. Consequently, the objective of this section becomes to supply an RL load and check whether the currents are sinusoidal and  $120^\circ$  out of phase respectively. The setup parameters are the same as before:  $V_{DC} = 750[V]$ ,  $R_S = 10[\Omega]$   $L_S = 10[mH]$   $Dead\ time = 2[\mu s]$ .

First of all, we start analysing the voltage on the three phases.

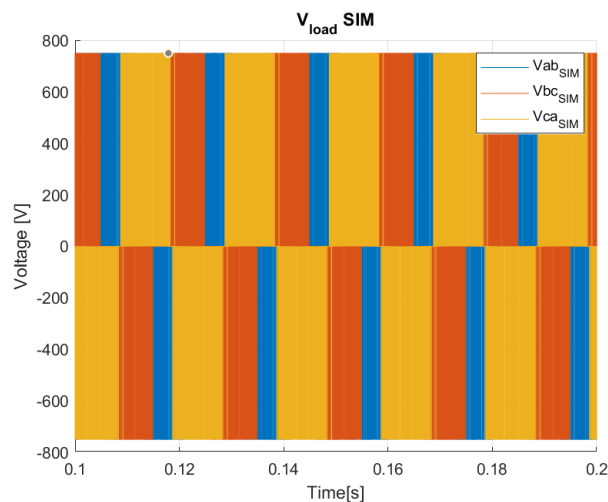


Figure 3.2-3 : Three-phase Voltage SIM

It is different from the Single leg inverter within the voltage has a positive value for half the period and a negative value for the other half. In this section, however, the three phases work synchronously, and each phase contributes  $2/3 T$  for the negative and positive half-wave. As before, waveforms must be viewed from the harmonic content in order to be better analysed.

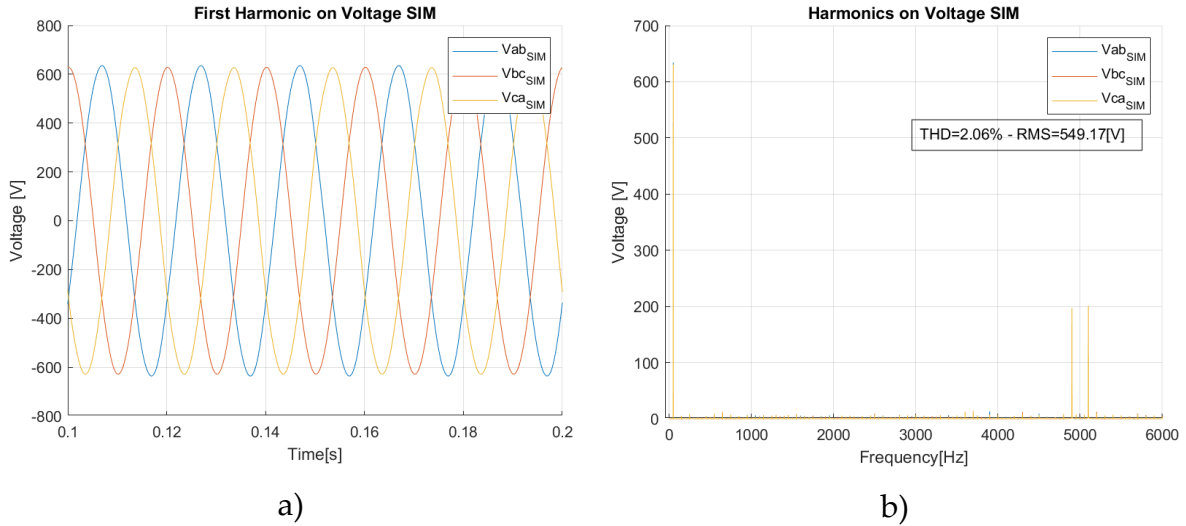


Figure 3.2-4 : Filtered Voltage and Harmonic content SIM

A most interesting observation emerges from the Figure 3.2-4. The 3rd harmonic is not present, its contribution is negligible since in a three-phase circuit the 3rd harmonic and its multiples have a homopolar character and do not contribute to the final waveform. For this reason,  $m_f$  could be chosen in multiples of three for low-power systems. In contrast, the 5th and 7th harmonics are evident. They contribute significantly to the distortion of the fundamental harmonic.

The value of the first harmonic of the concatenated voltage, theoretically should be:

$$V_{ab} = \frac{V_{dc}}{2} * m_a * \sqrt{3} \quad (\text{Eq. 3.2-1})$$

$$V_{ab} = \frac{750}{2} * 1 * \sqrt{3} \approx 650[V]$$

In reality, the first harmonic reaches a value of 630[V]. This is due to the dead time in the PWM, as it represents a hole in the voltages and causes the peak voltage to drop by approximately 3%.

A fundamental study is related to the simulation currents. We expect a reflection of the harmonics of the voltages on the currents.

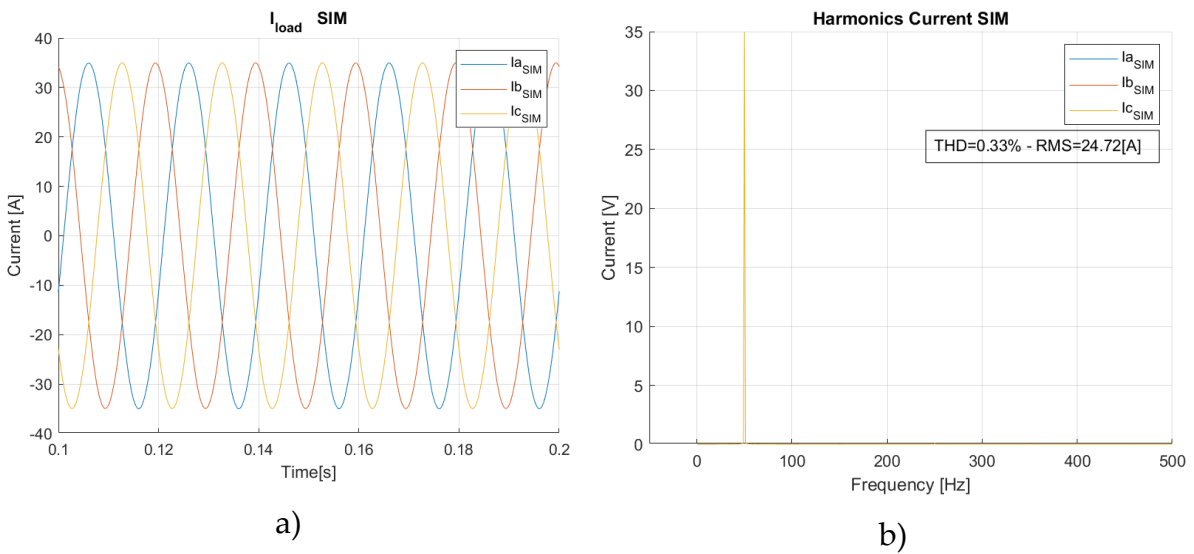


Figure 3.2-5 : Three-phase Currents(a) and Their Harmonic Content(b)

The result of the SIM mode is very promising. In fact, the THD is about 0.7% and consequently the RMS is equivalent to the amplitude of the first harmonic.  $I_{1rms} = \frac{I_1}{\sqrt{2}} = \frac{35[A]}{\sqrt{2}} = 24.74[A]$ .

We can now see the simulation results of the HIL technique.

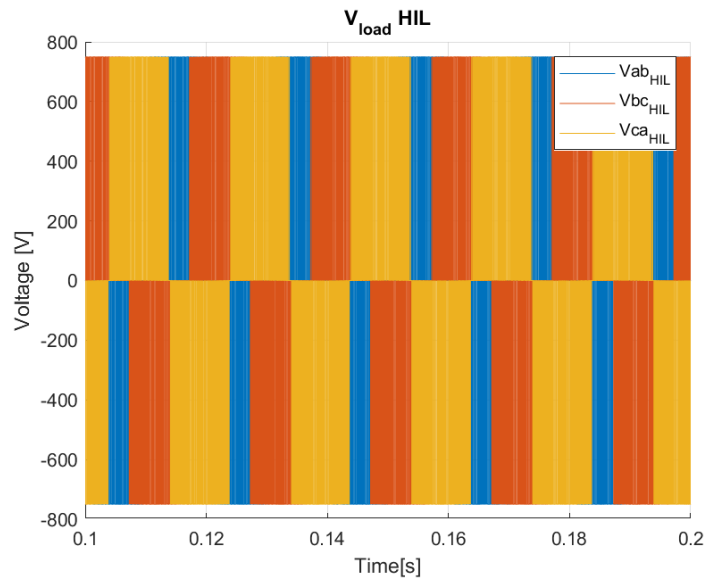


Figure 3.2-6 : Three-phase Voltage HIL

Only five period is plotted in the Figure 3.2-6. It mainly follows the assumption made earlier concerning the period of the half-wave. Each voltage has the same contribution. This can be seen in the first voltage harmonic in Figure 3.2-7.

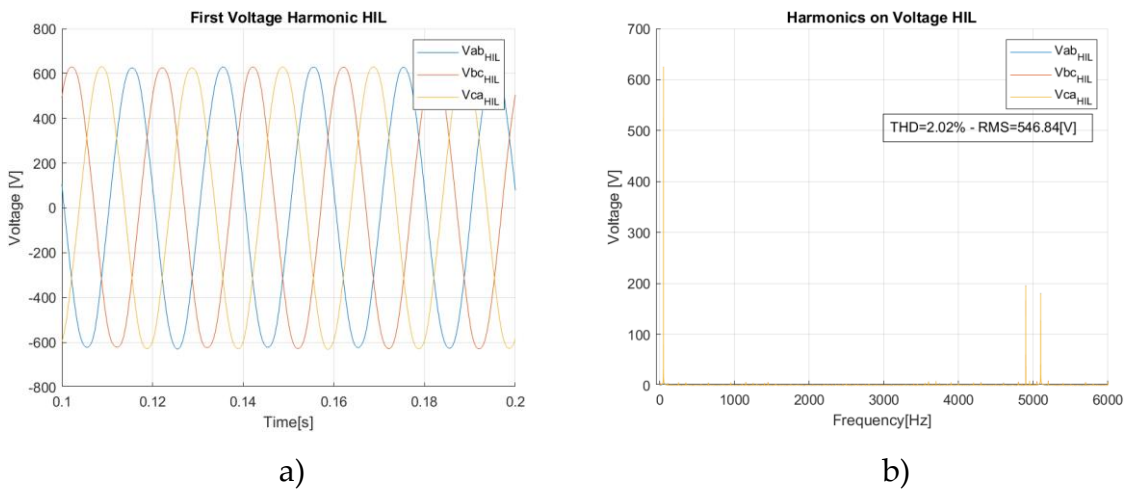


Figure 3.2-7 : Filtered Voltages Voltage(a) and Harmonic Contents(b) HIL

As we have already seen, the harmonic content of the voltage is limited to the 1st, 5th and 7th, and is also not as precise as the SIM mode but has oscillations around the main harmonic. Instead, the THD value is lower and consequently the RMS is higher. The value of the peak voltage of the first harmonic is a little bit lower than the SIM. It reaches 625[V] which represent an error of 0.8%.

Another important aspect is the currents in the HIL simulation. They are the real test to see if the inverter is working properly. Indeed, by observing them, we can validate our data and see if the PWM technique of the microcontroller is well controlled.

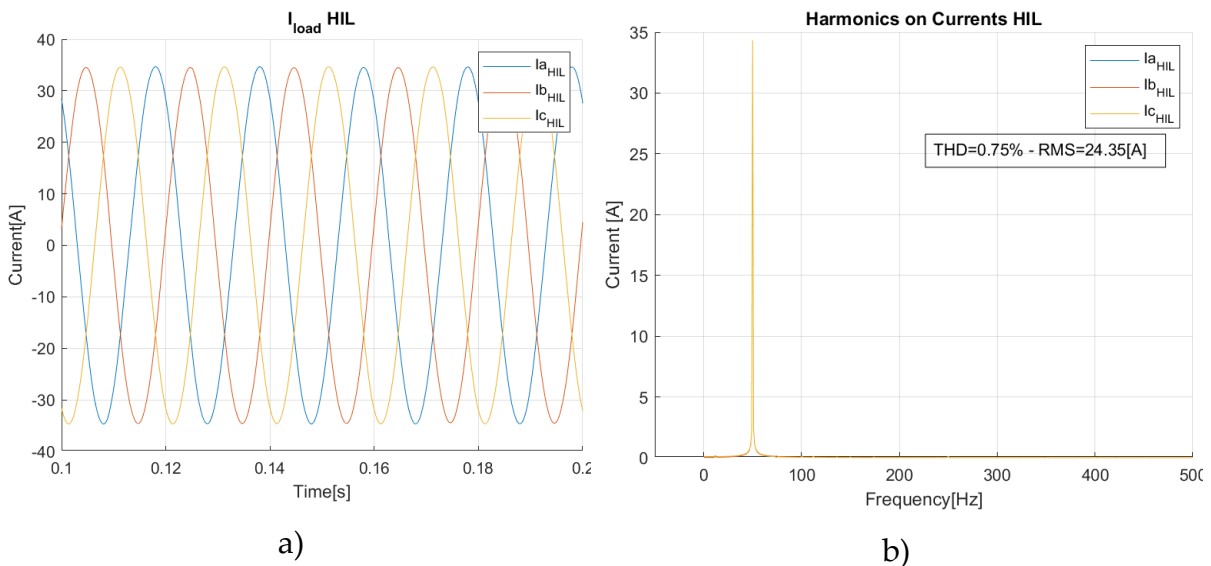


Figure 3.2-8 : Three-phase Currents(a) and Their Harmonic content (b)

The currents are sinusoidal and with a frequency of 50[Hz]. The displacement from them is fixed at 120°. Furthermore, the THD is very low which means that harmonics do not contribute a lot. These last data confirm that the HIL technique works correctly, and that the microcontroller can adequately handle the presence of more than one leg to be controlled.

### 3.3. Three-phase inverter with Induction Motor

Before considering the real case of controlling a synchronous machine, a simpler intermediate step is performed, by controlling an induction machine. Indeed, the synchronous machines control requires that the rotor angle be matched with the calculation within the microcontroller; this constraint does not occur for induction machine, resulting in a simpler control. Therefore, we will start by controlling an induction motor as load and observe its operating characteristic. In particular, we will not only focus on the steady state values but try to change certain parameters during the process and observe how the induction machine responds. It is also useful to remember the mechanical equation, since we will use the resistant torque to simulate a small load:

$$T_e - T_r = J_{eq} \frac{d}{dt} \Omega_m + \beta \Omega_m$$

For our purpose, in this case it is not necessary to choose a machine with special parameters, but it is essential to analyse the motor's inertia. If it is too low, a small change in electromagnetic torque could accelerate the machine to its maximum in a very short time period and damage it. The default value of the machine in the simulation was  $10e^{-6} [kgm^2]$ . This means that if the motor is driven with a torque of  $1 [Nm]$ , the acceleration  $\frac{d}{dt} \Omega_m$  would have to be  $10e^6 \left[ \frac{rad}{s^2} \right]$ , which is extremely high. Instead, we decided to set the inertia equivalent to  $1 [kgm^2]$ . The poles of the machine are 2. Following the proposal at the section 3.2, we create the electric scheme by only changing the load of Figure 3.2-1.

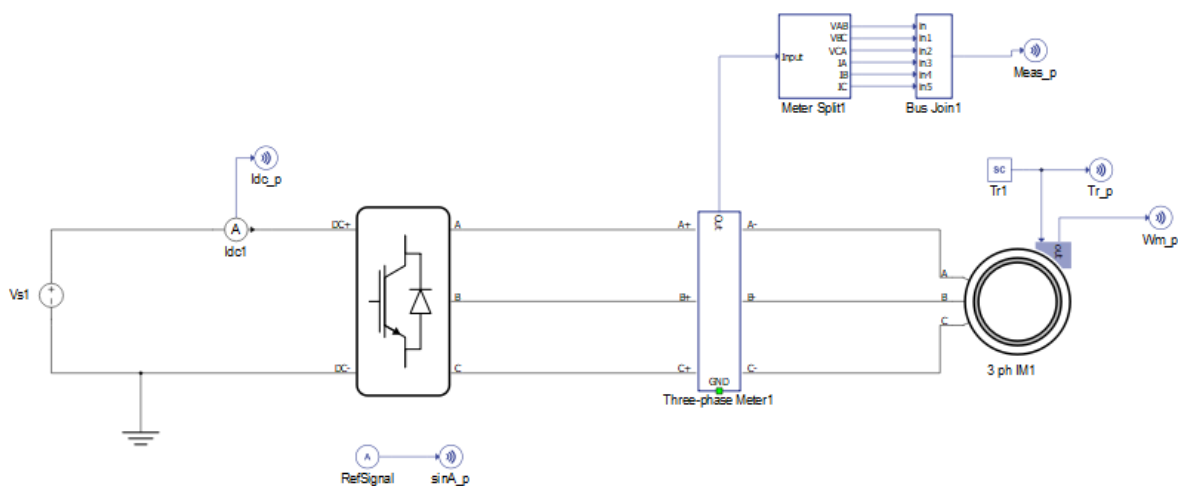


Figure 3.3-1 : Three-phase and Induction Machine Scheme

Since Typhoon HIL cannot manage more than one motor for each simultaneously, we performed two different simulations, and we used the same algorithm to control the

motor by acting on the modulation factor and the resistant torque. This algorithm was performed manually.

Algorithm 2 : Induction Motor Control

	$\Omega_m$	$m_a$	$T_r$
1:	0	0	0
2:	0	0.5	0
3:	60	0.5	5
4:	50	0.5	10
5:	30	1	10
6:	135	1	0
7:	157	1	0

After the two simulations, the first result to look is relate to the mechanical speed.

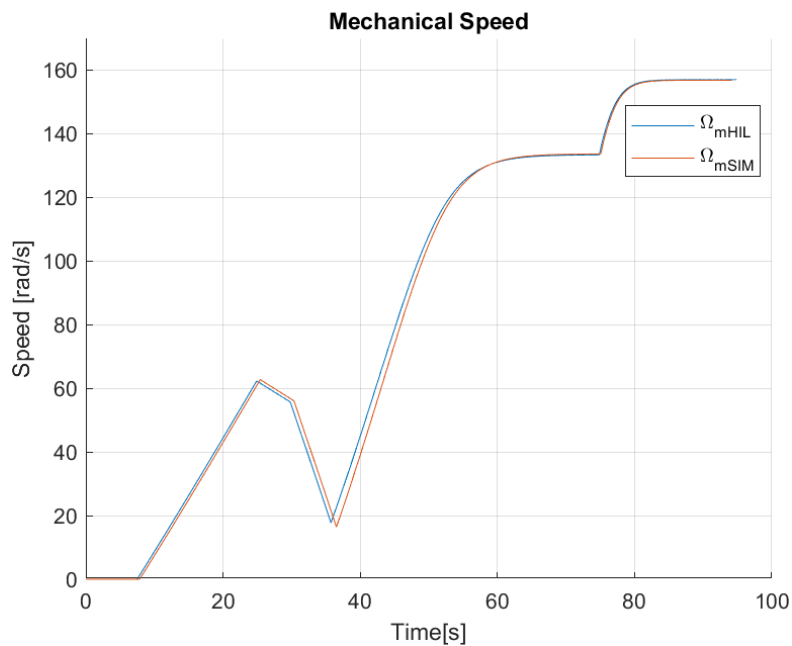


Figure 3.3-2 : Speed Profile for HIL and SIM modes

Combining this graph in Figure 3.3-2, with the algorithm, a number of assumptions can be made. Firstly, both simulations in steady state achieve the same maximum speed. In reality this is imposed by the frequency of the system, in fact at 50[Hz] corresponds an electrical speed of  $\omega_e = 2\pi * 50[Hz] = 314 \left[ \frac{rad}{s} \right]$ . Since the mechanical and electrical speed are linked by the number of poles, the maximum mechanical speed becomes  $\Omega_m = \frac{\omega_e}{n_p} = 157 \left[ \frac{rad}{s} \right]$ . In the other stages of the algorithm, we can say that they achieve roughly the same behaviour, with negligible deviation.

We will examine the currents and voltages of the two simulations. But since the voltages are not our main focus and the simulation lasts about 90[s], it is not useful to show and analyse them over the whole period of the simulation. The currents, on the



other hand, are more interesting to examine because they dynamically control the electric torque and also because the two speed profiles are very similar in terms of both speed and time between them. This means that the torque control was probably the same during the two simulations, so it is essential to study them in detail.

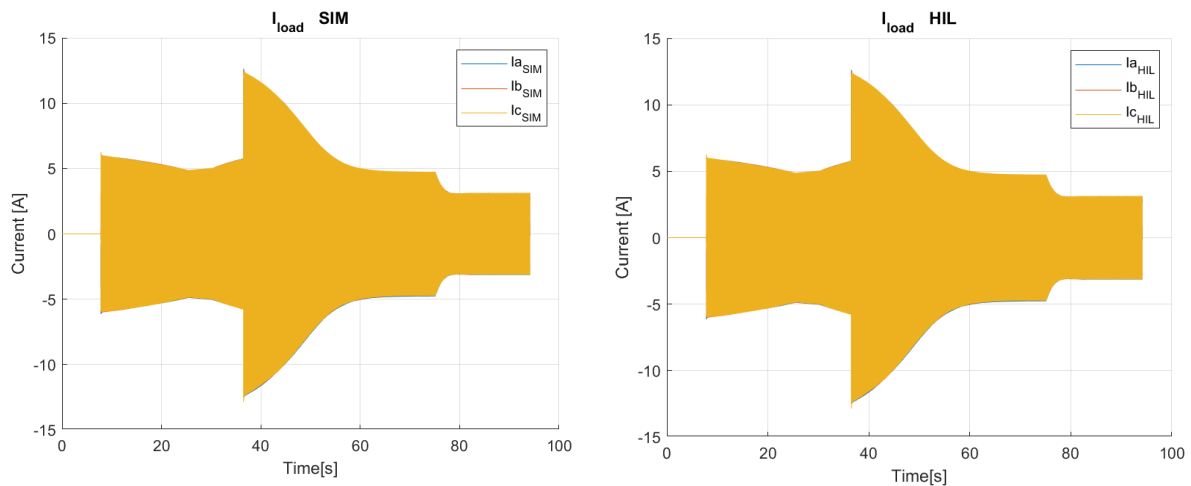


Figure 3.3-3 : Current in the Induction motor

They are similar, almost the same. During the initial acceleration phase, there is the same current of about 6[A]. Then, around 35[s], there is a peak current that reach about 12[A]. The resistant torque in fact becomes double to 10[Nm] and consequently so does the current. After this period, the current tends to return to the steady state value suitable for counteracting the resistant torque until it reaches a value of approximately 136[rad/s]. This means that the mechanical equation has found an equilibrium. It is therefore possible to calculate the power absorbed by the motor in this period:

$$P_m = T_e * \Omega_m \rightarrow \text{in steady state } T_e = T_r = 10[Nm] \quad (\text{Eq. 3.3-1})$$

$$P_m = T_r * \Omega_m = 1360[W]$$

After about 70[s], by removing the resistant torque, the motor will tend to reach its rated speed at 157[rad/s] or 50[Hz] with a lower current. As we were doing, for both voltages and currents, it might be interesting to examine the steady-state conditions under which the motor should operate, such as an RLE load. Under this assumption, we could focus on harmonics. We will take into account a period of time between 87 – 88[s].

The harmonics on the voltages are accurate, in fact both have a first harmonic at 50[Hz], the 3rd is neglected and there are the 5th and 7th that have a strong effect on THD.

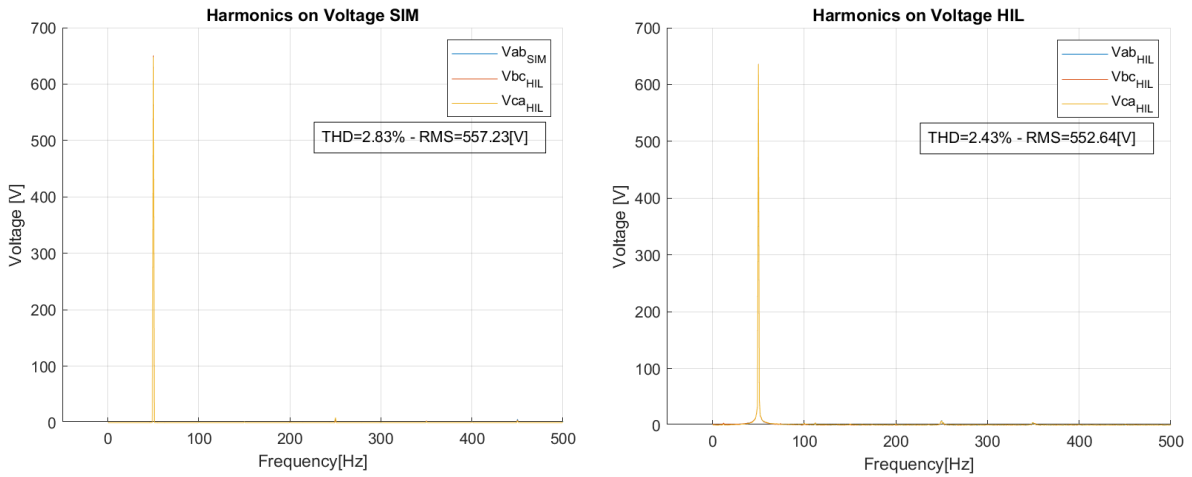


Figure 3.3-4 : Harmonic Content of the Voltage compared from SIM and HIL modes

The THD is lower in similar in both. There is a little discrepancy from the peak value of the first harmonic of about 3%.

This is a good result, but as always, the real test is related to currents. The sample taken into consideration always lasts 1[s] but in order to highlight the behaviour of the current, we focused on 5 periods.

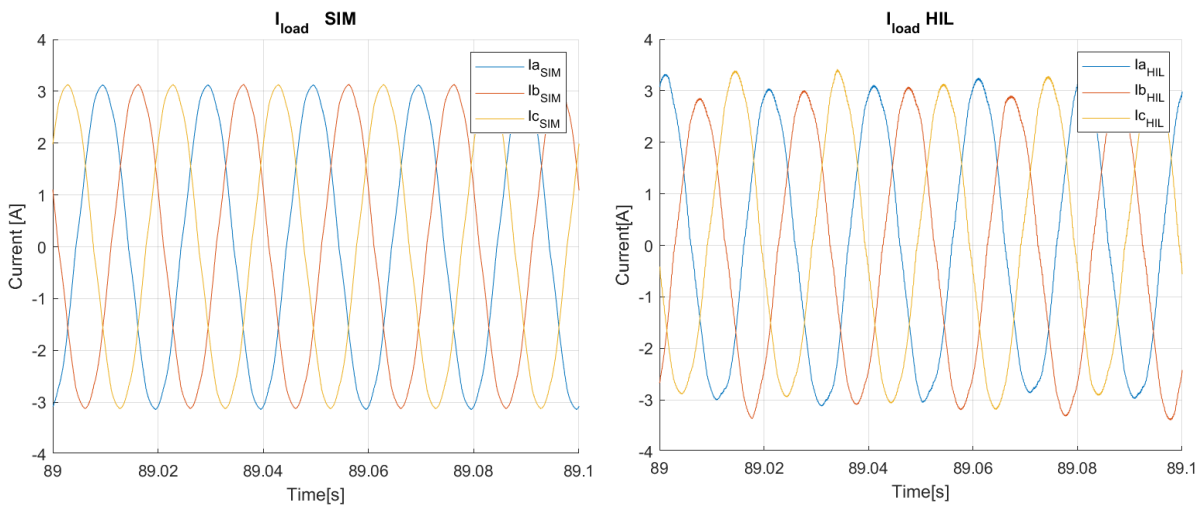


Figure 3.3-5 : Three-phase currents for SIM and HIL simulation

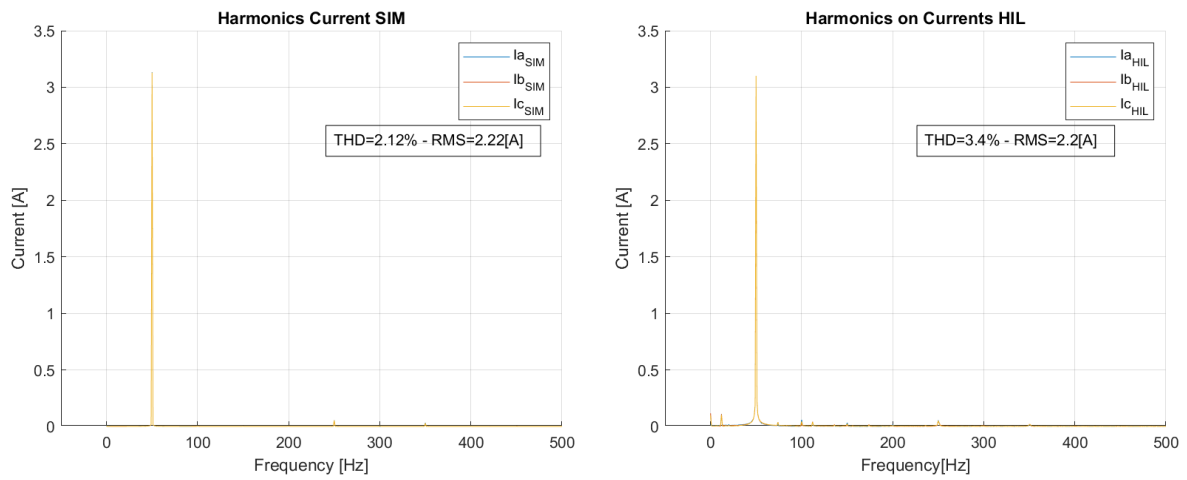


Figure 3.3-6 : Harmonic contents for Currents

The currents are amazing, they both fall at 50[HZ] and the harmonic content is very low. The THD of the HIL simulation is higher than that of the SIM and this could be expected. A few small harmonics such as subharmonics and the DC component are visible in the figure. The latter is a problem mainly because it causes power losses and thus heat but being very small it does not contribute significantly.



## 4 PMSM and FOC implementation

So far, we have discovered and studied how to feed a load with an inverter and how to handle it. We also focused on the harmonic content and verified that, from this point of view, the HIL technique allows us to validate our data with very good accuracy. In fact, all the results extracted so far were very similar to the simulation. From now on, however, we will focus on the most important part of the project, namely the PMSM and how the FOC scheme can be implemented in the microcontroller. In particular, we will look in detail at the inner and outer loop of the control scheme and how it can be used to supply the new configuration.

### 4.1. Three-phase PMSM: Matching Angle

Since our motor is a synchronous machine, it is necessary to study how to obtain the angle of the machine in order to use it in the equations and thus for its control. The first suggestion was to implement a sensor less configuration, in other words, avoid mechanical sensors. This is useful for a number of reasons, mainly to eliminate mechanical parts that could deteriorate and become damaged requiring more costly maintenance. In addition, the sensor less method must be very precise since a PMSM motor must not lose control. In the worst case, if this happens, it can completely damage the bogie of the train. For this reason, the sensors must be redundant, adding cost and maintenance. Instead, a sensor less control required only the measurement of some voltages or currents from which is possible to extract the electrical angle of the motor to use in the Clark and Park transformation and moreover also the frequency of these to know which is the rotor speed. Another crucial aspect is that we do not have to measure all the electrical parameters, as we are using a symmetrical, balanced three-phase system in which the sum of currents and voltages is zero. Therefore, if for some reason one current probe fails, it is possible to switch to another to continue operation. These suggestions require detailed study, as they need accurate measurement, require heavy implementation in the microcontroller, and consequently may take much longer to implement. For this reason, we decided in this thesis to simulate the usage of sensor and we used the value of speed  $\Omega_m$  and angle  $\theta_m$  that comes directly from the encoder implemented on the motor in the simulation. The test setup is show in the Figure 4.1-1. The mechanical sensors are the motor outputs, while the input is the resistant torque. We are interested in the currents calculated on the rotor frame, and to extract them we use a block that performs the conversion of phase currents  $i_{abc}$  to  $i_{dq}$  via Park's

transformation using the electrical angle  $\theta_e = n_p * \theta_m$ . This is necessary as it represents the position of the dq axis with respect to the reference axis. A first problem arises. The angle is not infinite but limited between  $[0 \ 2\pi]$  and it becomes necessary to add a line of code where the angle can be reset to zero if it exceeds the limit.

Practically speaking, the ADC block sends parameters such as currents and speed to the microcontroller via an analogue pin and the microcontroller read it from the internal ADC.

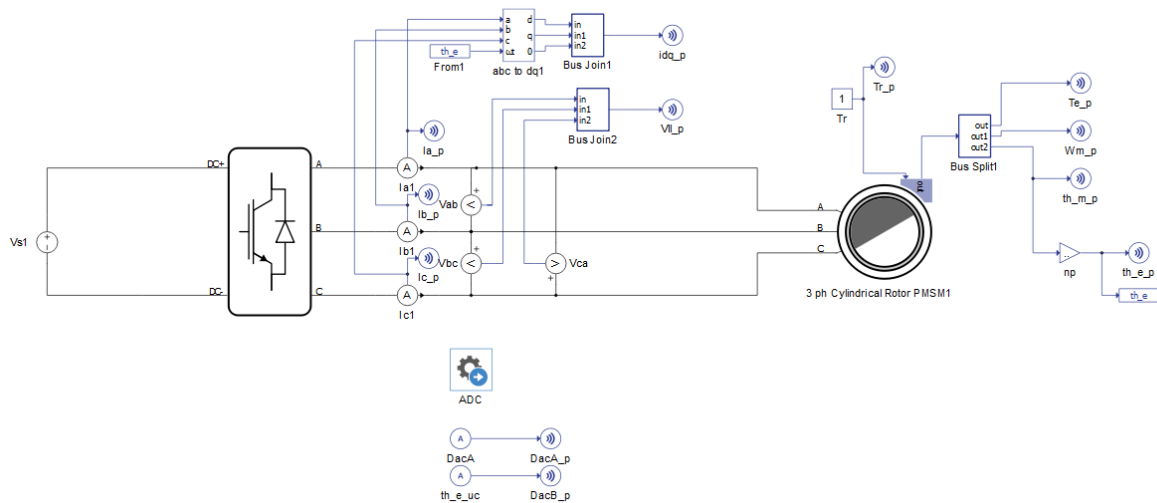


Figure 4.1-1 : Test Setup of Three-phase PMSM

These parameters are read by the microcontroller with a sampling time  $T_s = \frac{1}{f_s} = \frac{1}{10[kHz]} = 0.1[ms]$ .

If the HIL simulator and the microcontroller are not well synchronised, the calculated angle will be different from the real one, the Park transformation does not work, and the motor cannot be controlled to run as desired.

## 4.2. Three-phase PMSM: Current Control

After careful analysis of the angle match, we need to start implementing the FOC control scheme. One of the most interesting parts is the Current Control (CC), because in our scheme we have to handle four different currents. The purpose of this section will be to power the three-phase PMSM by implementing the inner loop of the FOC scheme. In particular, it will be interesting to examine the direct and quadrature current, the torque, and to confirm the relationship between these two. Figure 4.2-1 shows the setup used for the current control implemented in the microcontroller. It represents a part of the FOC diagram with some differences, such as the value of the compensation terms. As can be seen, the input of the system is the direct and quadrature current. From the motor equation, we know that the direct current does

not contribute to the torque and will be fixed at zero. Instead, the quadrature current allows the torque to be controlled directly as one derives from the other.

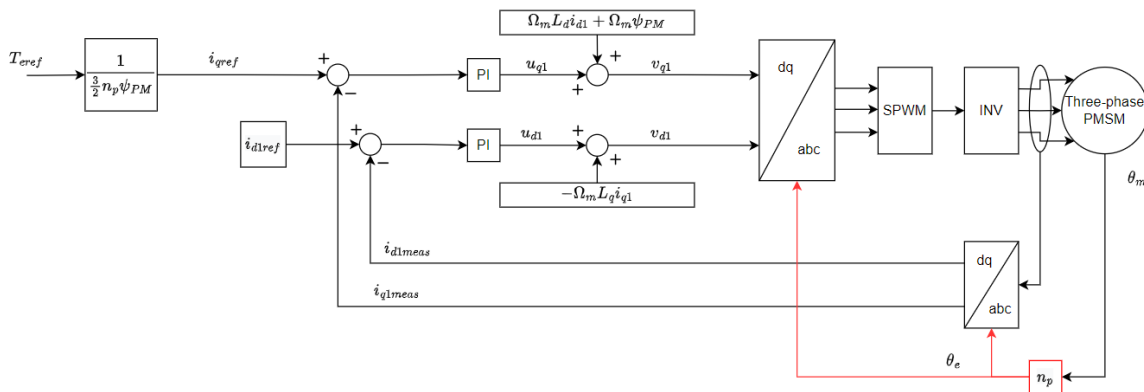


Figure 4.2-1 : Current Control for Three-phase PMSM

To realise this scheme, we will introduce an algorithm to see under different conditions what the system's response is. The scheme is reported here.

Algorithm 3 : Three-phase PMSM Current Control		
	Time[s]	$T_e$ [Nm]
1:	0	0
2:	1	3
3:	10	30
4:	20	75
5:	30	225
6:	40	450
7:	41	75

The motor parameters used in the test are the same as the one we will use for our project, but we decided to reduce the inertia to  $10[kgm^2]$  in order to increase speed responses. Moreover, to avoid an overcome of the base speed, the torque resistant is added as an input of the motor by using the Davis equation (section 2.3)

The first parameter we will focus on is the torque since it is our system input. Figure 4.2-2(a) shows the reference torque  $T_{ref}$  (Algorithm 3), the resistant torque  $T_r$ , and the actual electromagnetic torque  $T_e$ . Due to Davis equation, in the operational range the resistive torque is approximately proportional to the speed (Figure 2.3-6). The speed profile is shown in Figure 4.2-2 (b). The velocity does not follow a linear behaviour, due to the dynamics of the motor and the electrical parameters. Since the mechanical and electrical equations are differential equations of the first degree, the velocity and the current should increase exponentially with a given period called mechanical and electrical time constant equal to:

$$\tau_m = \frac{J_{eq}}{\beta} ; \tau_e = \frac{L_s}{R_s} \tag{Eq. 4.2-1}$$

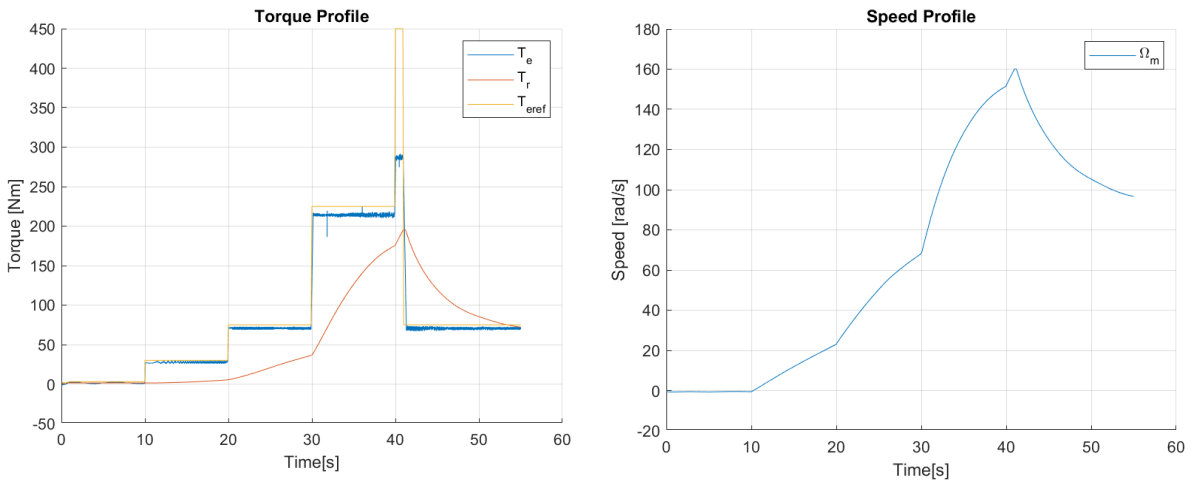


Figure 4.2-2 : Torque Profile(a) and Speed Profile(b)

The Figure 4.2-3 perfectly describes the behaviour of the currents on the rotor reference frame. As one imagines from the behaviour of the electromagnetic torque, the quadrature currents also follow the reference precisely. The direct current, on the other hand, is not so accurate: we would like it to remain zero for all conditions, but this does not happen properly. There are several hypotheses that could be made to justify it, such as the absence of the filter after the inverter, the PIs which are not well tuned since a step in the torque could cause an instability.

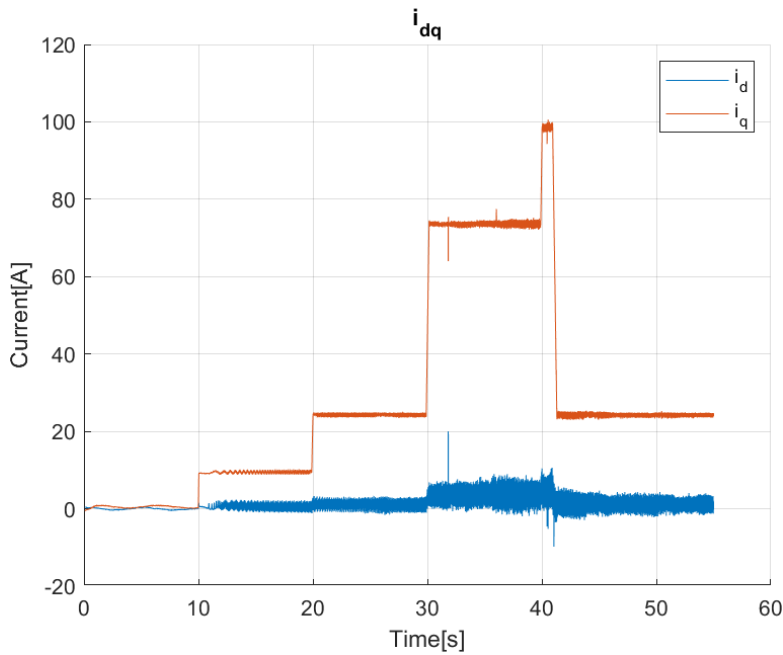


Figure 4.2-3 : Direct and Quadrature Currents Profile



As far as PI controllers are concerned, it is important to fine-tune them. The method used to calculate the gain of the P and I terms has just been presented. For both PI regulators, the values calculated from the theoretical point of view are:

$$\begin{cases} k_p = 2.86 \\ k_i = 186.11 \end{cases} \quad (\text{Eq. 4.2-2})$$

By acting on the PI parameters, the desired behaviour can be achieved because they also could work as a filter.

It is interesting to look at the phase currents to understand their actual behaviour and also to see if they are symmetrical and balanced. Figure 4.2-4 (a) shows the entire behaviour of the currents but what is interesting is the steady state condition in Figure 4.2-4(b). What we notice is that the phase currents have the same frequency, but the amplitude change a little bit during the periods. Performing several simulations, we understand that this behaviour depends by the little imprecision of the ADC in reading the currents and the angle.

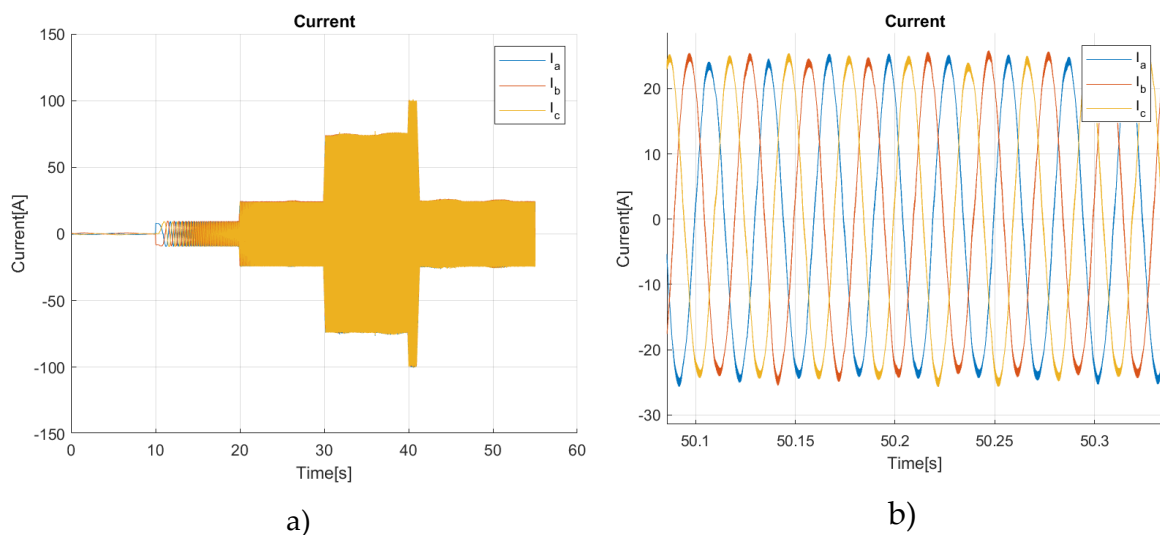


Figure 4.2-4 : Overall Current(a) and Steady State Current(b)

As done before, the quality of the current is analysed by means of harmonic analysis in the Figure 4.2-5. The frequency of the fundamental is not 50[Hz] because we did not reach the rated speed at 33[Hz] which is about  $100 \left[ \frac{rad}{s} \right]$  mechanical. As for the amplitude, it reaches approximately 23[A] during the time period considered.

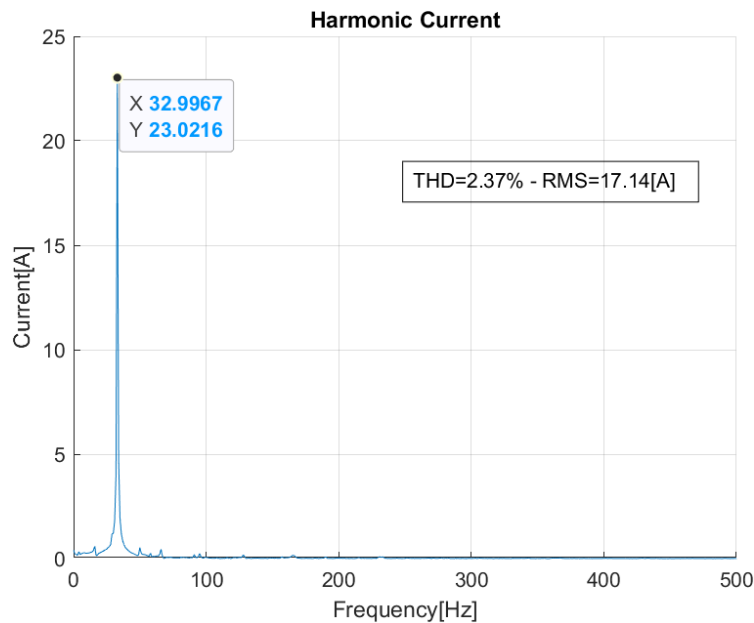


Figure 4.2-5 : Harmonic Content of the Steady State Current

### 4.3. Double Three-Phase PMSM: Current Control

In the previous section, we talked about the current control of a three-phase PMSM. Now we will perform another important step that doubles all the setup done so far. The considerations are actually the same as before, but what is different is how to control the two windings individually. Figure 4.3-1 is the current control diagram describing the operation of a DTPMSM. There are two things to remember. The first is the displacement angle between the two windings, its value is  $30^\circ$  and must be considered since both windings must be referred to the same fixed frame with the rotor. It will only be necessary to measure one angle (on the first winding) since the displacement is a fixed value. The second thing to remember is the presence of the power sharing block, which will be analysed in the power sharing chapter 5. In the coming tests, it will be set to send the same amount of current in the two circuits to perform a unique torque. This step is crucial because it contains most of the code that we will use for the end of the project, which is why the microcontroller must be checked to see if it can handle the entire effort.

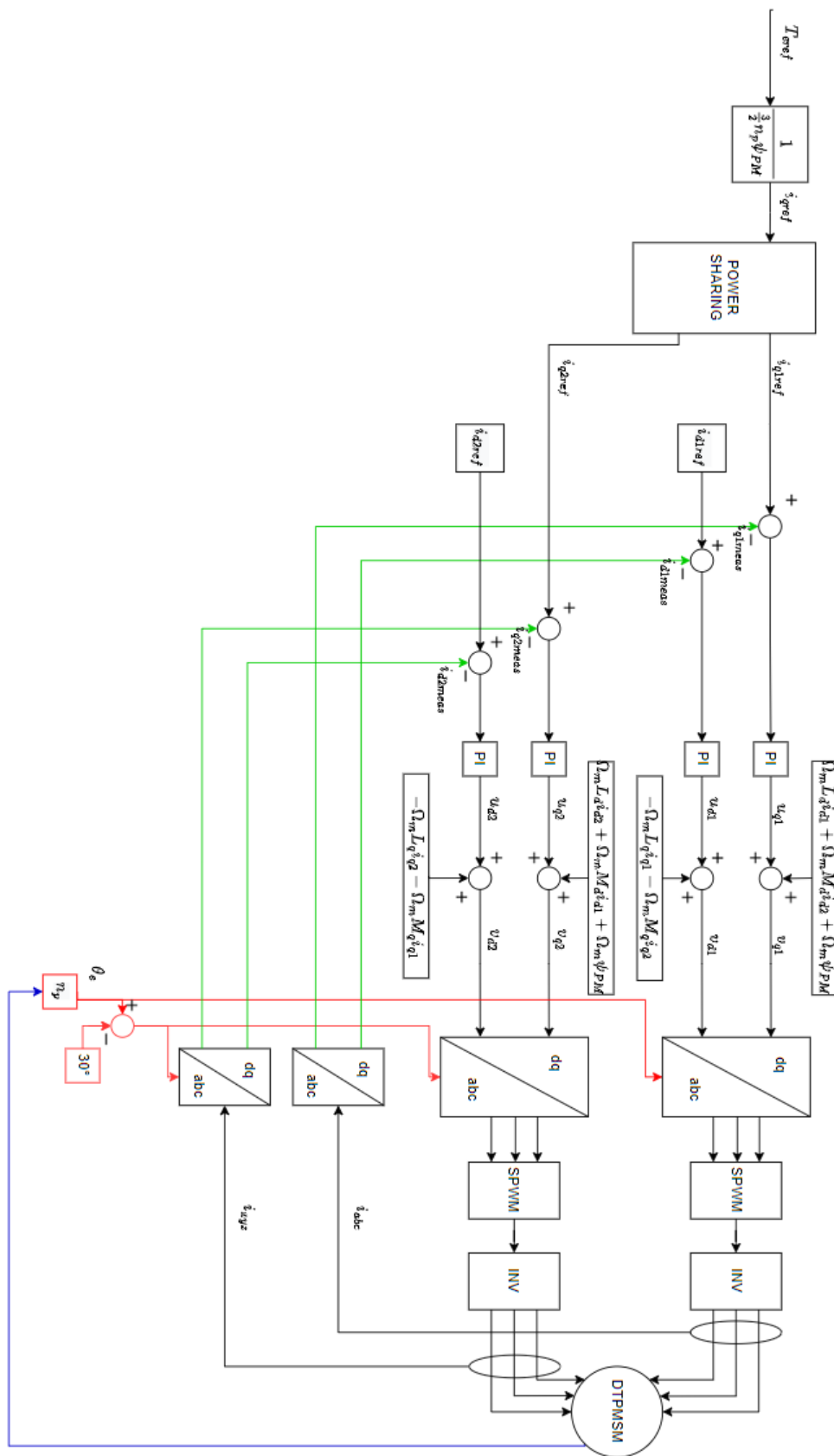


Figure 4.3-1 : Block Scheme of DTPMSM Current Control

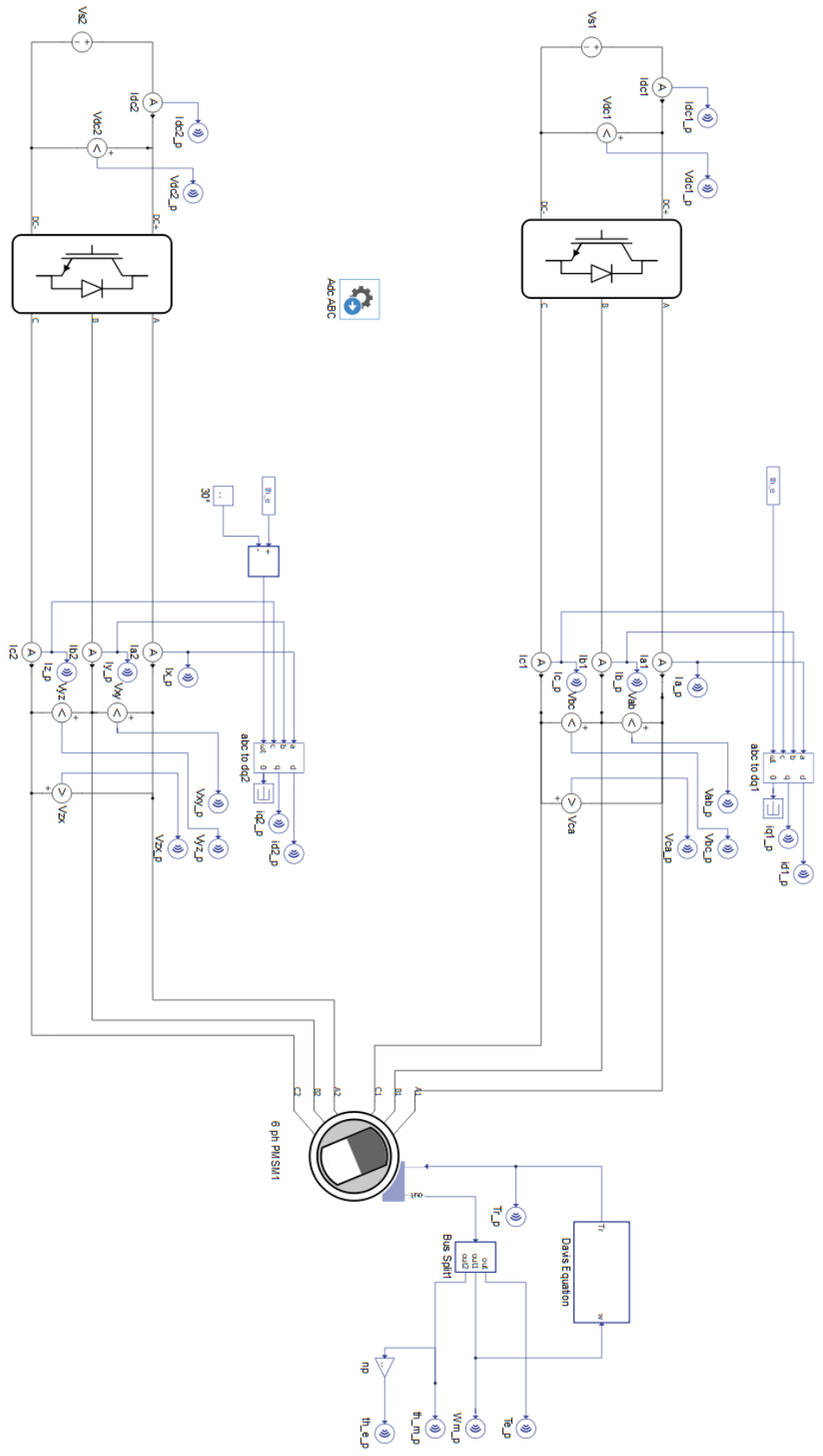


Figure 4.3-2 : Complete Setup of a DTPMSM

As there are more parameters to be tuned, it becomes more complex to monitor each one and set them correctly. The configuration we will use is very similar to that of the complete project and is shown in Figure 4.3-2. The motor inertia is set to  $1[kgm^2]$  and the other parts are the same as previously. In these tests, we will run the same simulation using Algorithm 3.

Figure 4.3-3 represents the speed (a) and torque (b) profiles obtained from the simulation. There are several points to explain. The first concerns the initial period up to 10[s] where acceleration occurs. At this point, the reference torque is 3[Nm] and the resistance increases from 1.3 to 1.9[Nm]. The problem is that the actual electromagnetic torque oscillates with a certain frequency that increases linearly with speed. In fact, focusing on the torque in Figure 4.3-4, we can take as a sample a period. The frequency is about  $2.66 [Hz] \approx 16.72 \left[ \frac{rad}{s} \right]_e$ . The speed, on the other hand, about  $8.3 \left[ \frac{rad}{s} \right]_m$ . Since the two values are related to the numbers of poles, we can say that this oscillation depends by the speed of the motor. This is also confirmed elsewhere.

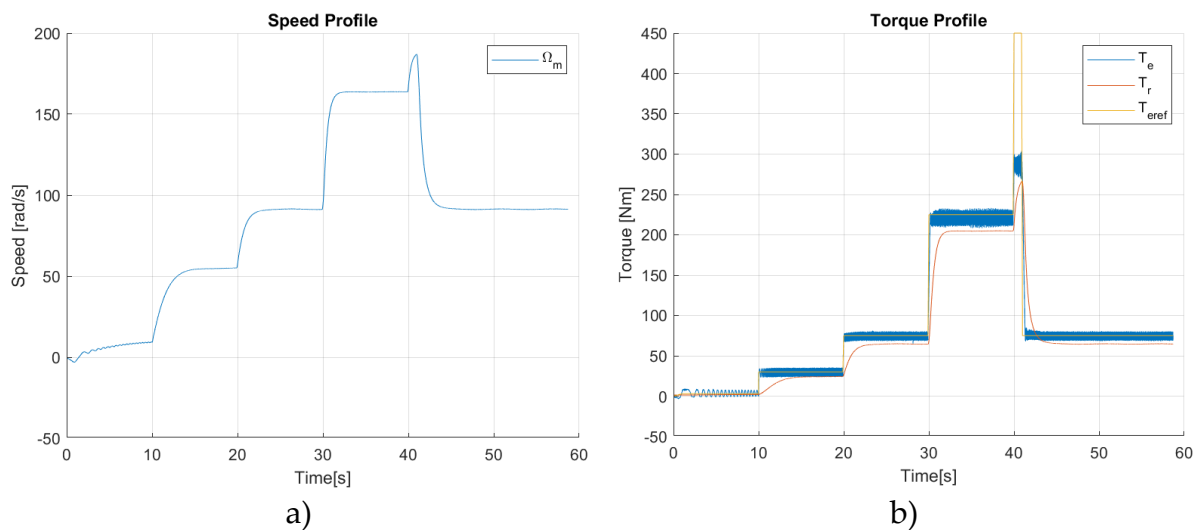


Figure 4.3-3 : Speed(a) and Torque(b) Profile DTPMSM with Algorithm 3

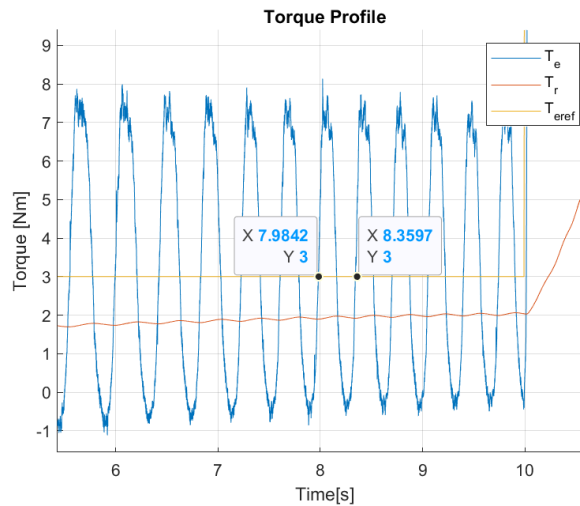


Figure 4.3-4 : Focus on the Torque before 10[s]

As we well know, torque is related to the current on the quadrature axis. In this configuration, we have to control two inverters to manage the power flowing to the motor. It may be interesting to check if the two windings can work together to reach the setpoints decided by Algorithm 3. This step is crucial because we also have to validate the possibility of managing the displacement of the phases in the microcontroller. Figure 4.3-5 show the behaviour of the currents in the two windings. It should be remembered that the power sharing is set at 50%, therefore theoretically both inverters should supply the windings with the same power, which means with the same torque and consequently the same current. In reality, this is what happens to the DTPMSM. It is powered by the same quadrature current in both windings. There are several points to focus on. Firstly, the oscillations follow the motor speed in a linear manner with respect to torque. This was expected, since the torque is proportional to the current. The problem is that direct currents also oscillate in approximately the same way. For this reason, the direct current will never be equal to zero but will make a contribution that increases with torque because the oscillations will also increase. Furthermore, between 30 and 41 [s] both direct currents suffer the same effect, losing control. The cause is that during this time the base speed is exceeded and consequently the direct currents attenuate the electromagnetic torque. As can be seen from the torque profile during this time, the electromagnetic torque tends to decrease. In this case, the effect is not so bad; under other conditions, the situation could be considerably worse.

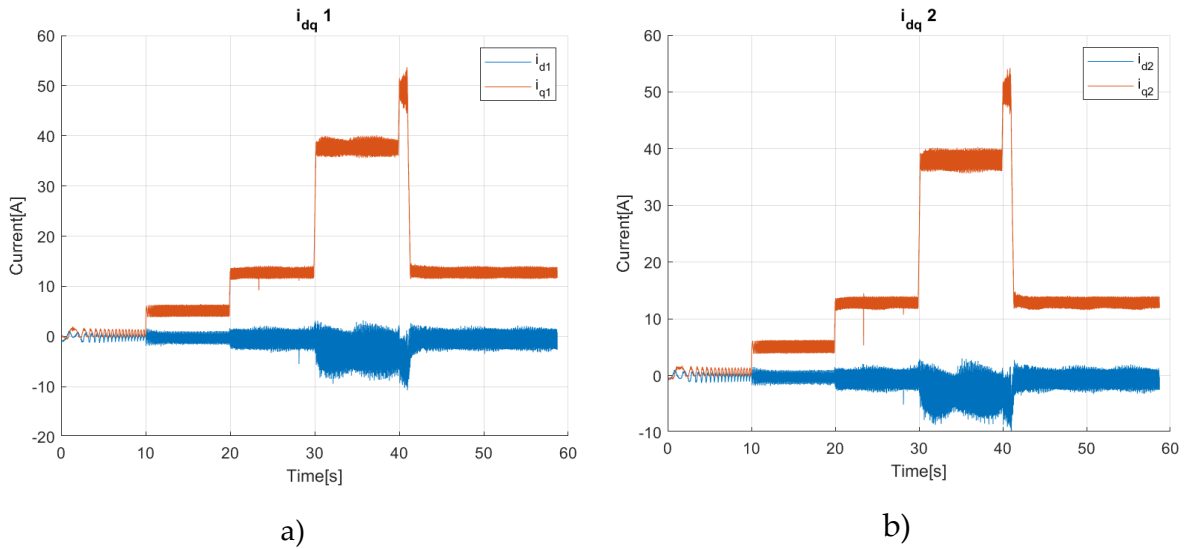


Figure 4.3-5 : Direct and Quadrature Currents on the First (a) and Second (b) windings

#### 4.4. DTPMSM: Speed Control

This section represents the conclusion of setup and control, what we are generally interested in is controlling the speed of our train during shunting operations. The speed represents the input parameter of our system which, through a PI controller, will decide the electromagnetic torque that the motor will have to impart in order to contrast that resistance and acquire a given speed. The FOC scheme is now completed and is the one of the Figure 2.4-3. The PIs for the current control are the same in (Eq. 4.2-2 ). Furthermore, we need another PI controller for the speed which links it with the torque by using the mechanical equation. The value for the gain parameters we chose are:

$$\begin{cases} k_p = 70 \\ k_i = 5 \end{cases} \quad (\text{Eq. 4.4-1})$$

The circuit diagram is the same as in Figure 4.3-2 and in the same way we will use ideal sources to power the inverters. Even in this case, we used an algorithm to handle more possibilities and see if it works in each condition.

Algorithm 4 : Three-phase PMSM Speed Control

	$Time[s]$	$\Omega_{mref} \left[ \frac{rad}{s} \right]$
1:	0	1
2:	10	10
3:	30	25
4:	60	75
5:	90	157
6:	120	25

In these simulations we set the inertial of the motor to its nominal value  $J_{eq} = 147.13[kgm^2]$ . What interests us most in this part is the speed of the system and how the torque is handled by the PI. Figure 4.4-1 shows the behaviour of the speed during this process. the yellow line is the speed reference if it is a stepped waveform. In reality, the speed reference cannot be a step, as it does not make physical sense to have a discontinuity in the kinetic energy. For this reason, we limited the increase in velocity by using a ramp with a slope of about  $4 \left[ \frac{rad}{s^2} \right]$  and in this way the red line in the figure was created, which is the true velocity reference. In the end, the blue line indicates the true speed of the motor.

The first point to focus on is the slope of the speed. Specifically, the actual velocity has the same behaviour as the reference but starts to increase about 1[s] after the reference. When it reaches the maximum set value, the speed is higher than the reference by about 1[rad/s], which corresponds to less than 1% of the error that is tolerable. This behaviour is imposed by the PI controller, in fact we can try to improve it to better follow the speed reference. Even during deceleration, the speed follows the reference closely.

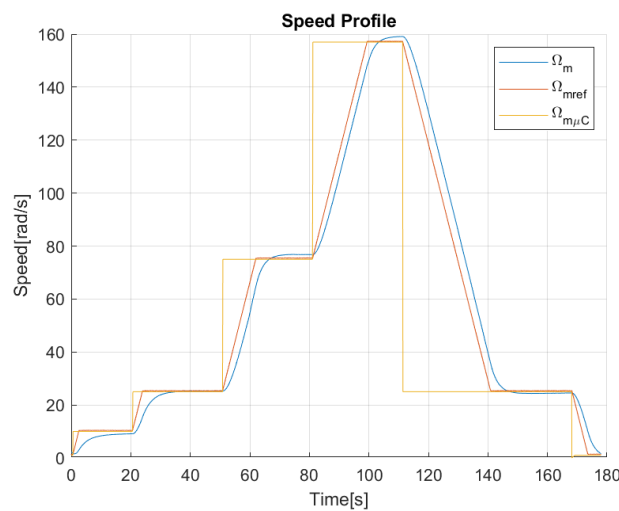


Figure 4.4-1 : Speed Profile of the Simulation with the Speed Control



We are now interested in the behaviour of torque ( Figure 4.4-2) and currents (Figure 4.4-3) which, as we know from the chapter 2.3, are linearly related by a coefficient. Here again, we have divided the reference current by a 50% share, so we expect the quadrature currents of the first and second windings to be approximately the same. Since torque is directly controlled by speed, every time there is an acceleration phase, it increases with a high slope to a maximum value at around 850[Nm] and this is what we expect since during the first moments of acceleration, we need all the power available to increase speed. Actually, if we control the slope of the reference speed, we can limit the increase in torque, but since the motor has been sized to fit these parameters, the torque has the desired profile. Furthermore, when the reference speed is reached, the torque decreases to match the resistant, since no acceleration is required.

Another interesting thing is that during the deceleration phase, the motor is powered by a negative torque that functions as the resistant torque. If we look at the value it reaches, it is about  $-650[Nm]$ , not  $-850[Nm]$ . This is due to the presence of the resistant torque of  $200[Nm]$ , in fact, performing some calculations:

$$T_e - T_r = J_{eq} * \frac{d}{dt} \Omega_m + \beta \Omega_m \tag{Eq. 4.4-2}$$

$$\frac{d}{dt} \Omega_m \approx \frac{T_e - T_r}{J_{eq}} \approx \frac{-650[Nm] - 200[Nm]}{147.135[kgm^2]} \approx -5.77 \left[ \frac{rad}{s^2} \right]$$

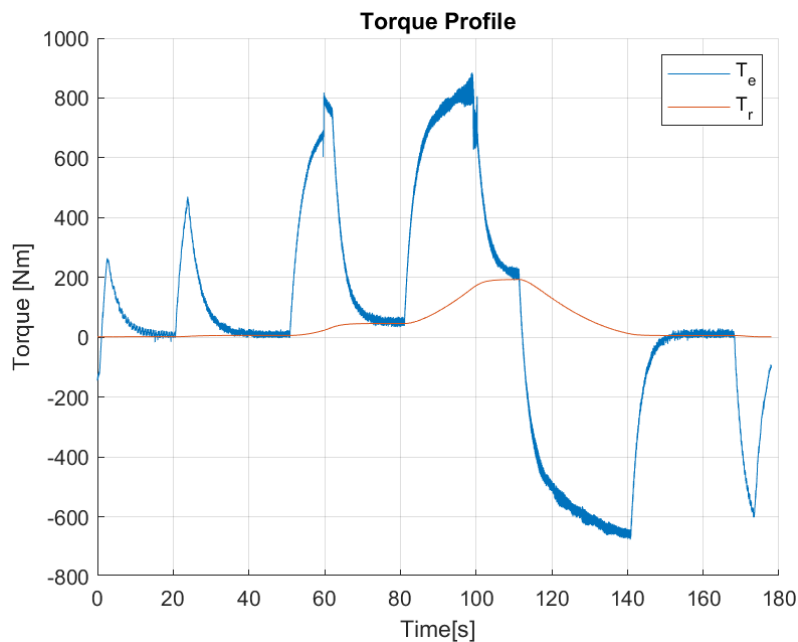


Figure 4.4-2 : Torque Profile in Speed Control

It is fundamental to look at the behaviour of quadrature currents. Since they have the same shape as the torque, we can once again confirm that the currents follow the reference with a good approximation. Furthermore, since the share is set at 50%, we

can observe the value that  $i_{q1}$  and  $i_{q2}$  reach. During the acceleration phases, they reach a maximum value of 150[A] which corresponds to a torque of approximately 430[Nm] that each winding carries out. During the coasting phases, when the speed should be constant, the currents reach a steady value that always depends on the reference torque. Another point to focus on is the behaviour of the direct currents. They remain roughly at the zero value, but at 100[s] a peak in the currents is noticeable. This is caused by the fact that the nominal speed is reached by the reference but not the actual speed. The PI therefore has some difficulty in handling this point.

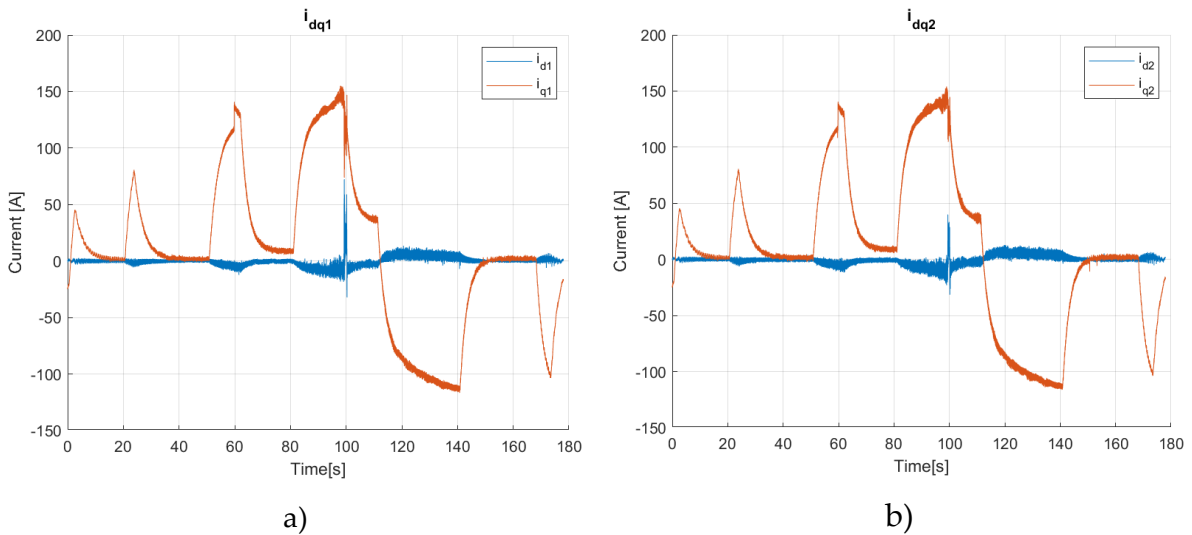


Figure 4.4-3 : Current Profile of the First(a) and Second(b) Windings

There is another interesting point to be analysed, and it concerns the phase currents. We will see two different moments, the first relating to the acceleration phase (*ACC*) between 55 – 56[s], the second during the coasting mode (*COAST*) between 76 – 77[s]. Since the behaviour of the currents in the first and second windings is the same, we will use as reference only the first one.

Tracing Figure 4.4-4, we can say that during *ACC* mode, the phase currents appear sinusoidal and increase during the process while maintaining their shape. In contrast, the *COAST* currents are very dirty and sinusoidal behaviour cannot be discerned.

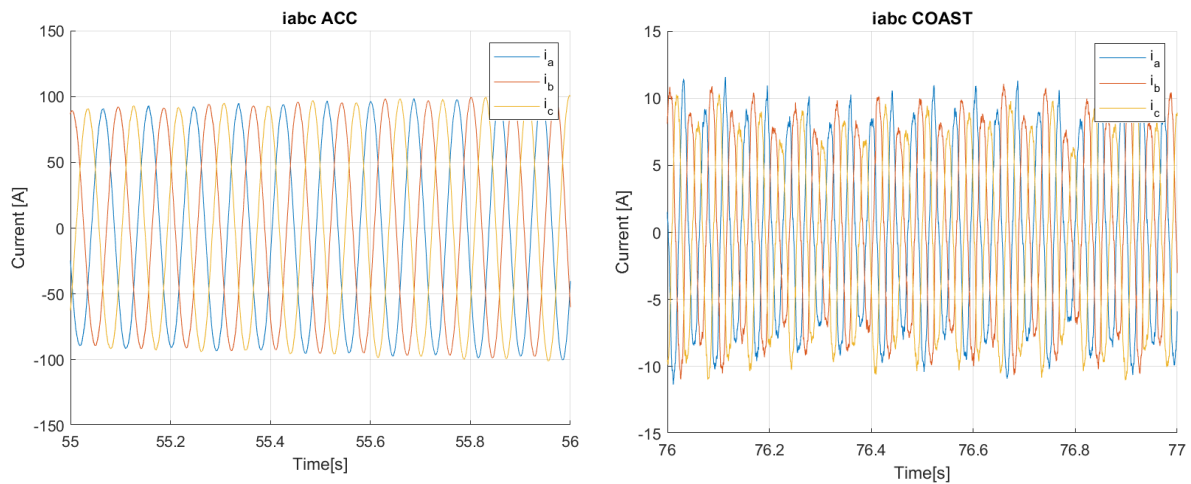


Figure 4.4-4 : Comparison between ACC and COAST mode.

To better understand the reason of this shape, we must observe the pairs in Figure 4.4-5. There are two considerations to make, the first concerns the oscillation that the torque has. In ACC mode it is regular, but in *COAST* mode its shape changes very quickly, altering its value by several tens of *Nm*. Another fact is that during coasting mode, the electromagnetic torque crosses the resistant torque several times. The speed controller reacts to this phenomenon and rapidly changes and reverses the currents. It is necessary to solve this problem, as it affects current ripples and harmonics. This step will be studied in detail during Chapter 7 where we will try to improve the values for the controllers. For now, it is useful to study these problems in order to understand how to act.

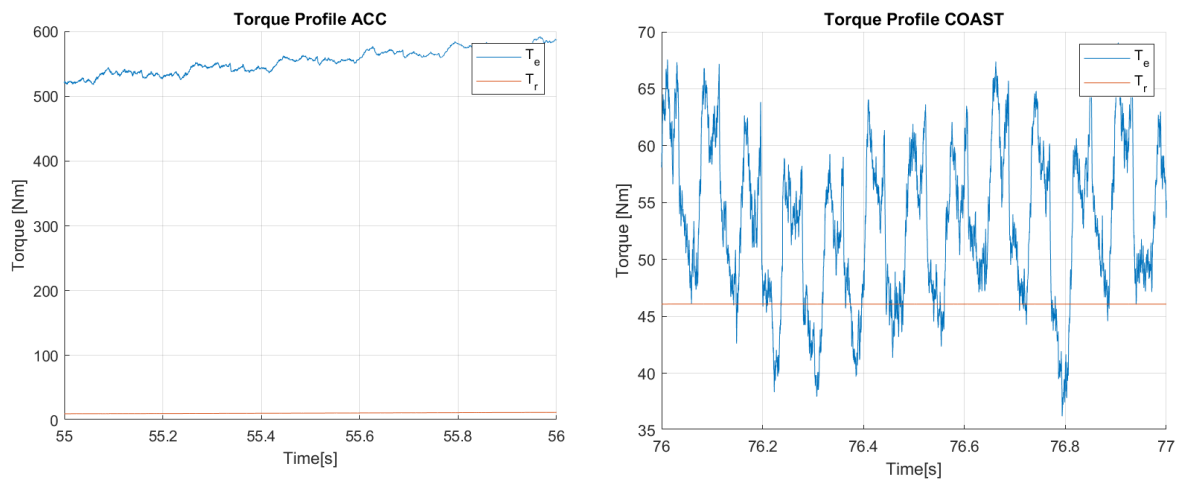


Figure 4.4-5 : Comparison of Torque for ACC and COAST mode



# 5 Power Sharing

## 5.1. Introduction and Aims

In the previous chapters, many references have been made to power sharing which represents a fundamental part of the control scheme. This section needs to be implemented since we do not have two identical sources, but FCs and batteries are different in terms of function, mainly because they are sized for opposite and complementary functions. In particular, we want to use the FCs as main sources and the batteries only to help for instance during acceleration or during a high earth gradient. For these reasons, the power they can deliver is different. The power we have decided to dedicate to a single motor is composed of 31.4[kW] from the FCs and 90[kW] from the batteries, which must be managed in order to comply with certain constraints on how to distribute power.

Once we have focused on our purpose, there are a few conditions to be examined in detail with respect to the use of sources. The first concerns the state of charge (SOC) of the batteries. This is the most important value for choosing whether they can be used.

Lithium-ion batteries have a service life that depends on several factors and their capacity decreases over time. It is influenced by the number of charge and discharge cycles. As they age, the quantity of reactants decreases as the electrolyte degrades to form inert compounds. For these reasons, batteries will be limited to between 20% and 80% of their available energy.

Since the fuel cell and batteries must work together, the current they can deliver is different and depends mainly on three phases:

- Acceleration (*ACC*)
- Coasting (*COAST*)
- Deceleration (*DEC*)

Based on these constraints, we developed a control scheme to manage source utilisation. Figure 5.1-1 shows the logic scheme implemented in the Power Sharing block. There are several things to be analysed, in particular there is a commission that must be followed, that is, the train must be powered by the FCs as the primary source and the batteries as the secondary source. The only way to charge the batteries is to use the FCs, so when the train returns to the deposit for the night, it will only be refuelled with hydrogen. If the SOC of the batteries drops to 20%, we have to charge them up to a certain SOC value before using them again. Actually, we set this value at

80%, but it could also be changed to 50% or lower, as in this case the batteries cannot help the FCs during the acceleration phases. The batteries are mainly recharged during the break phases when they can recover the power which comes directly from the motor. There are some constraints due to the batteries ability to absorb energy. Actually, we chose a 45[Ah] battery pack with an overall voltage of 750[V]. This means that the battery pack can store 33.75[kWh] of energy. Since the power is 90[kW], the  $C_{rate} = \frac{P_b}{E_b} \approx 2.6$ . This parameter is a reference value which indicates the amount of batteries we could discharge in one hour if the power output is constant. In charging mode, however, since the motor can deliver 120[kW], the  $C_{rate}$  is increased to 3.2. This means that we have more power that can be used to brake the train since we need to have a stronger control during the deceleration phases.

Let's now describe in detail the logical scheme in Figure 5.1-1. It is a loop that is performed within the microcontroller every 0.1[ms]. There are four configuration that we created to decide how much power each winding should perform.

Table 5.1-1 : Configuration

Configuration	$i_{q1}$	$i_{q2}$
1:	$i_{q1max}$	$i_{q2} = i_{qref} - i_{q1max} \geq 0$
2:	$i_{qref}$	0
3:	0	$i_{qref} \leq 0$
4:	$i_{q1max}$	$i_{q2} = i_{qref} - i_{q1max} \leq 0$

Where  $i_{qref}$  is the current that comes out from the speed controller and  $i_{q1max} = 70[A]$  is the maximum current performed from the FCs.

There are two main paths divided by the *ACH* (always charge). In this point the algorithm decides if the train can work normally ( $ACH = 0$ ) or get into the always charge mode ( $ACH = 1$ ) in which only the FCs could be used to supply the motor. In the normal mode, each step was discriminated by the difference between the speed reference and the measured one  $\Delta\Omega_m = \Omega_{mref} - \Omega_{m meas}$ . Looking at the diagram,  $\Delta\Omega_m$  is always compared with a threshold velocity  $\Omega_{mTH}$  due to the fact that the reference and the measured velocity will never be exactly the same value. Therefore, we set a threshold velocity of 0.5[rad/s] thus the error should be less than 0.5%.

During the acceleration phases (*ACC*), it is desired to push the motor as far as possible in order to reach the reference in approximately 40[s], which is why configuration 1 allows the motor to be pushed from both sources. On the other hand, during deceleration (*DEC*) only the batteries are able to recover energy, in fact the reference current of the first winding is zero and the second is negative. For *COAST* mode, however, we only need the FCs as sources but at the same time we want to charge the batteries. This means that the FCs will push as the maximum value and all the power that the motor does not need will be sent to the batteries. Of course, this is only the

case if the SOC of the battery is below 80%. If the SOC drops below 20% after acceleration, the loop enters in continuous charging mode. In this mode, the FCs always charges the batteries up to the set limit, which means that ACC and COAST modes work in the same way.

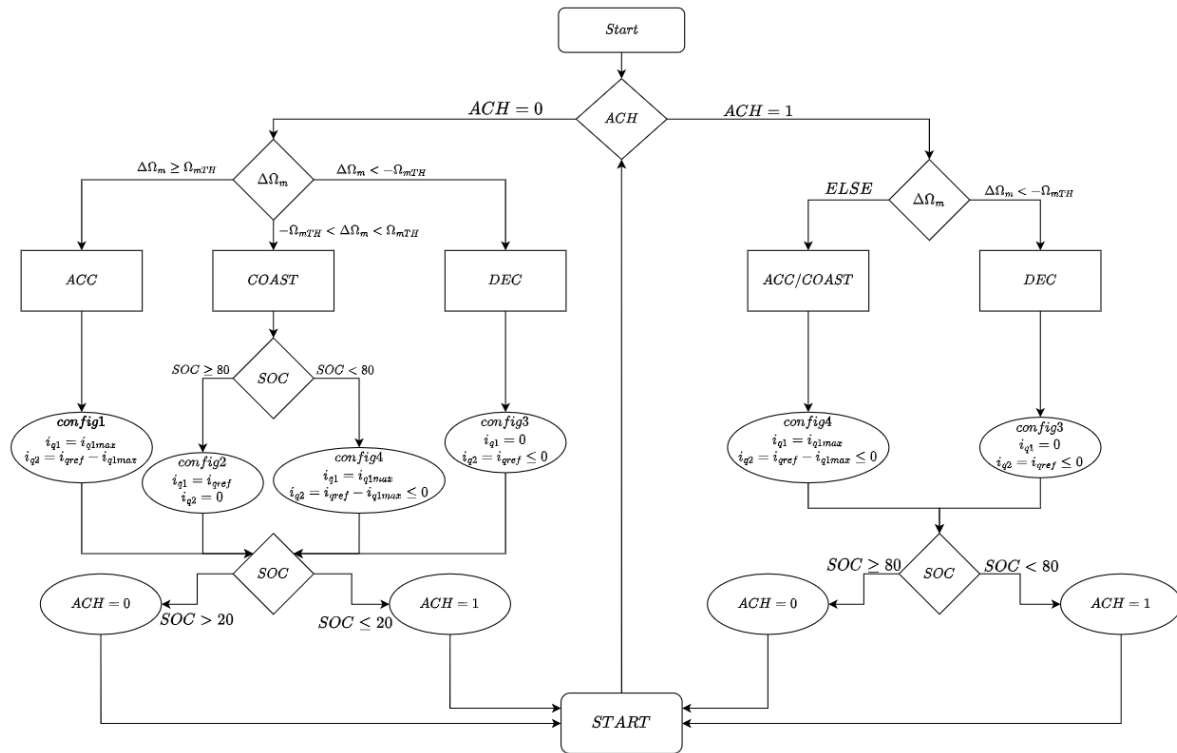


Figure 5.1-1 : Power Sharing Logical Diagram

## 5.2. Power Supply Wiring Diagram

We will implement the Power Sharing block and also the FCs and batteries in the simulation. The wiring diagram changes slightly. For FCs in particular, we will need a diode to prevent current return as shown in Figure 5.2-1. In addition, some filters are needed to limit the voltage ripple since it is strictly dependent on the current and a rapid change in the current can alter the normal behaviour of fuel cells.

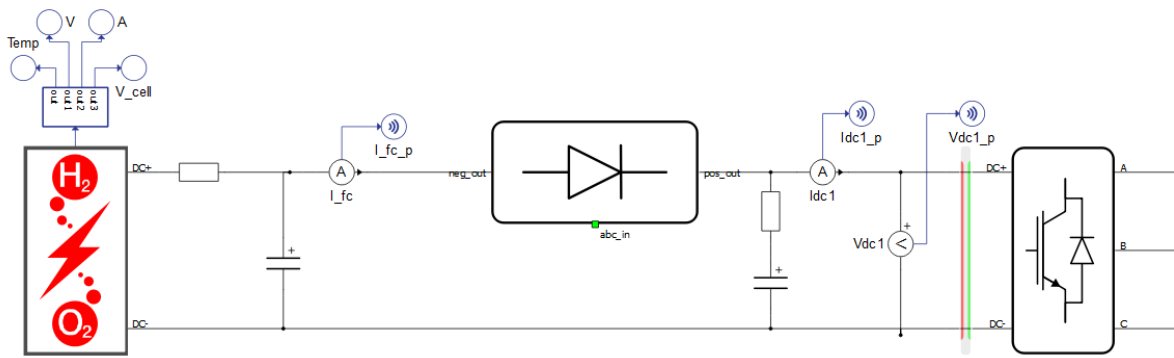


Figure 5.2-1 : Electrical Scheme of the Fuel Cell in Typhoon HIL

Figure 5.2-2 shows how batteries are implemented. Since the voltage depends on the energy contained within them, it is not as variable as that of FCs.

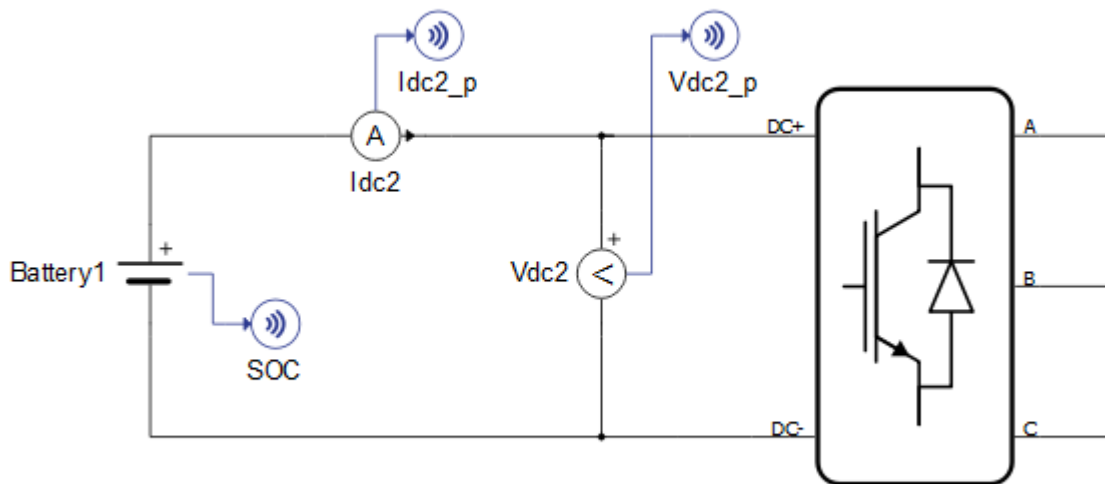


Figure 5.2-2 : Electric Scheme of Batteries in Typhoon HIL



### 5.3. Logical Scheme Diagram Tests

These tests are fundamental and took several time; indeed the entire configuration is now completed and therefore the PIs must be tuned as best as possible each time the scheme or logic is changed. This means that the adjustment of the PIs mentioned in section 2.5 is only the basic step that indicates where to start to fine-tune them.

There are some interesting conditions to take a look at and observe how the algorithm works. In particular, three different tests will be executed differentiated by the initial state of charge  $SOC_{init}$ .

Table 5.3-1 : Logic Scheme Tests

Test	Action	$SOC_{init}$
1:	$ACC \rightarrow COAST \rightarrow DEC$	50%
2:	$ACC \rightarrow COAST \rightarrow DEC$	19%
3:	$COAST$ at $10 \left[ \frac{rad}{s} \right]$	19%

The tests are carried out by imposing the parameters of the speed and current controllers. There are a few considerations to be made regarding the choice of these settings. First, the gain parameters are adapted to work with a defined setup under defined conditions. For this reason, they must be changed if the setup is altered or there are particular operating conditions. The second consideration is that all variables must give a strong response since we cannot lose control in any situation and also because we want to see what is the limiting response that can be obtained.

The PIs initially was tuned by considering the mechanical time constant  $\tau_m = 3[s]$ , the electrical  $\tau_e = 0.03[s]$  and the value used for the tests are:

$$\begin{aligned}
 & \text{Speed Regulator} \begin{cases} k_p = 60 \\ k_i = 15 \end{cases} \\
 & \text{Current Regulators} \begin{cases} k_p = 1 \\ k_i = 100 \end{cases}
 \end{aligned}
 \tag{Eq. 5.3-1}$$

Figure 5.3-1 shows the step and ramp response of the speed controller. The response of the speed controller has an overshoot, reaches the reference in the expected time and is strong enough to follow it with a very low error during the acceleration phases.

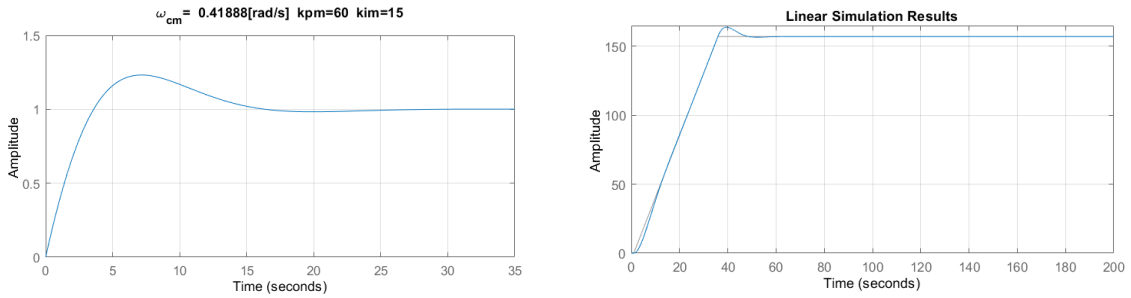


Figure 5.3-1 : Step and Ramp response of the Speed Controller

Current regulators (Figure 5.3-2) also have an overshoot. The profile is able to follow their reference in a short time, about 0.01[s], in fact it is 100 times faster than the speed controller.

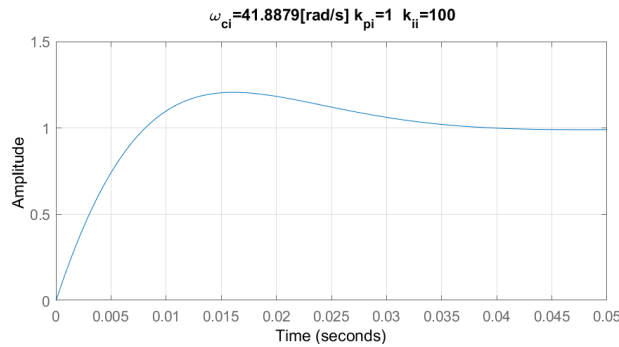


Figure 5.3-2 : Step Response of the Current Controllers

The speed and the torque profile performed by the motor by using this gain parameters are shown in Figure 5.3-3. If we look at the details, the motor speed touches and exceeds the reference several times during its operation. The reason for this is that there is a reference deviation  $\Omega_{mTH} = 0.5 \left[ \frac{\text{rad}}{\text{s}} \right]$ , which corresponds to a variation of  $0.15 \left[ \frac{\text{km}}{\text{h}} \right]$ , and because the speed controller pushes with the integral gain (mainly in the current controller) more than necessary, creating the oscillations. This fact is confirmed by observing the torque profile. It can be clearly seen that during the acceleration and deceleration phases it always oscillates in the same way without exceeding the limits. During the coasting period, the speed remains almost unchanged, but the torque has peaks from the nominal value to zero. These are very rapid and are caused by the logic diagram. Actually, the configuration changes quickly from 3 to 4 and vice versa, and it has a stronger effect on the first winding.

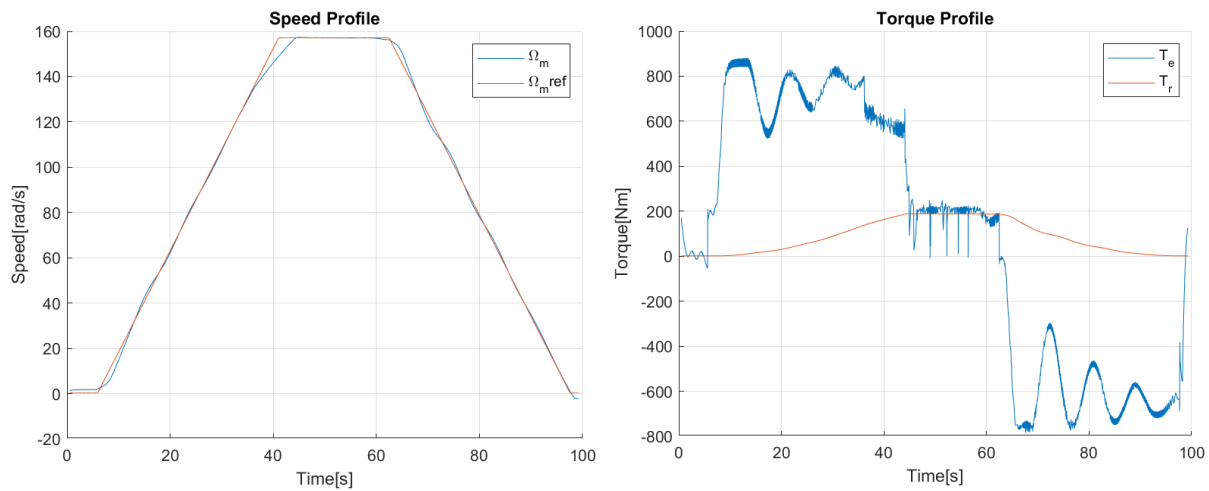


Figure 5.3-3 : Speed and Torque Profiles

Acting on the PIs parameters we want to reduce the oscillations we have seen during acceleration and deceleration and try to improve the power sharing logic by imposing a hysteresis in the change of configuration. This will result in a more linear behaviour, avoiding stresses on the engine that would lead it to damage more quickly.

As far as PI is concerned, the time constants are modified; in particular the mechanical time constant is  $\tau_m = 0.5[s]$ , the electrical one is  $\tau_e = 5[ms]$  and the new values used are:

$$\begin{aligned}
 \text{Speed Regulator} & \begin{cases} k_p = 362.488 \\ k_i = 18.2278 \end{cases} \\
 \text{Current Regulators} & \begin{cases} k_p = 1.2833 \\ k_i = 6.4524 \end{cases}
 \end{aligned}
 \tag{Eq. 5.3-2}$$

Figure 5.3-4 and Figure 5.3-5 represent the responses that PIs have with respect to a step and a ramp. We chose these parameters mainly to reduce oscillations. There are no overshoots in any of the step responses that caused violent oscillations. The current integral gain was drastically reduced, as it was the parameter that initially produced problems. In addition, we greatly increased the proportional parameter of the speed controller. It gives a strong contribution to the torque, allowing the reference to be followed with minimal error.

To reduce the rate of configuration change, we add a hysteresis function to the logic diagram that delays the decision made with respect to speed. This allows the microcontroller to estimate the condition of the motor in a more real way and decide which configuration is really needed without incurring errors that create torque fluctuations.

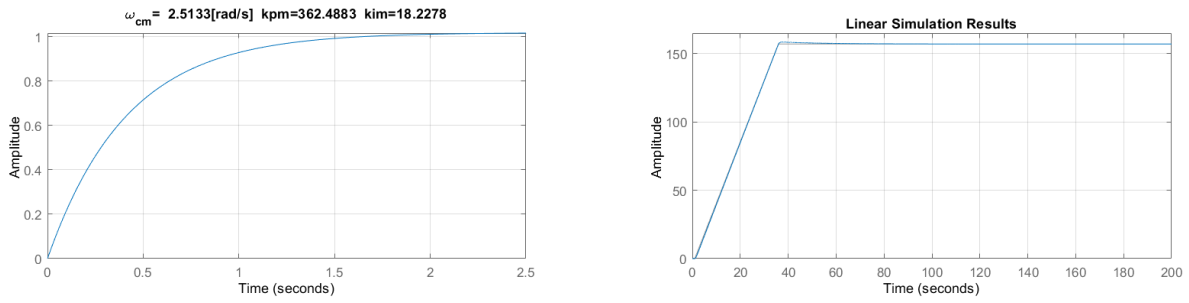


Figure 5.3-4 : Step and Ramp Response of the Speed Controller

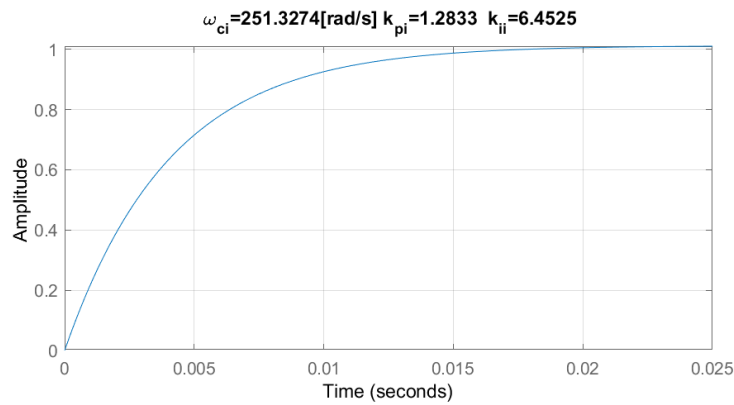


Figure 5.3-5 : Step Response of the Current Controllers

We performed tests with these latter values and the results are presented below.

### 5.3.1. Test1(T1)

In the first test is considered the normal and nominal condition in which the motor should work during its run. In particular, using the speed control, we can decide the motor target velocity. In this test, we start from zero up to nominal speed imposing an initial SOC of 50%. It is essential to remember that the resistant torque is performed by the Davis equation without considering the gradient.

Figure 5.3-6 show the main speed and torque profiles. One of the most fundamental aspects is the acceleration performed by the motor using both windings. If we extract the data from the speed, we can see that the acceleration is about  $4 \left[ \frac{rad}{s} \right]$  and the deceleration about  $4.36 \left[ \frac{rad}{s} \right]$ . This is a useful parameter indicating that the FOC and Power Sharing diagram work well together. Focusing on torque, we see that the oscillations have been drastically dampened. In addition, in both the first instants of acceleration and deceleration, the torque has initial spikes higher than the rest of the profile but always without exceeding the set limits. These peaks are due to the fact that in the first moments when the reference changes, the speed error is maximum and then

decreases as it stabilises. It is also useful to remember that the acceleration is fixed and limited, and the electromagnetic torque imposed on the motor increases with the resistant torque to keep the acceleration constant. By adding a delay in the change of the logic scheme configuration, we have greatly improved the behaviour during coasting mode by avoiding rapid torque changes and consequently decreasing oscillations.

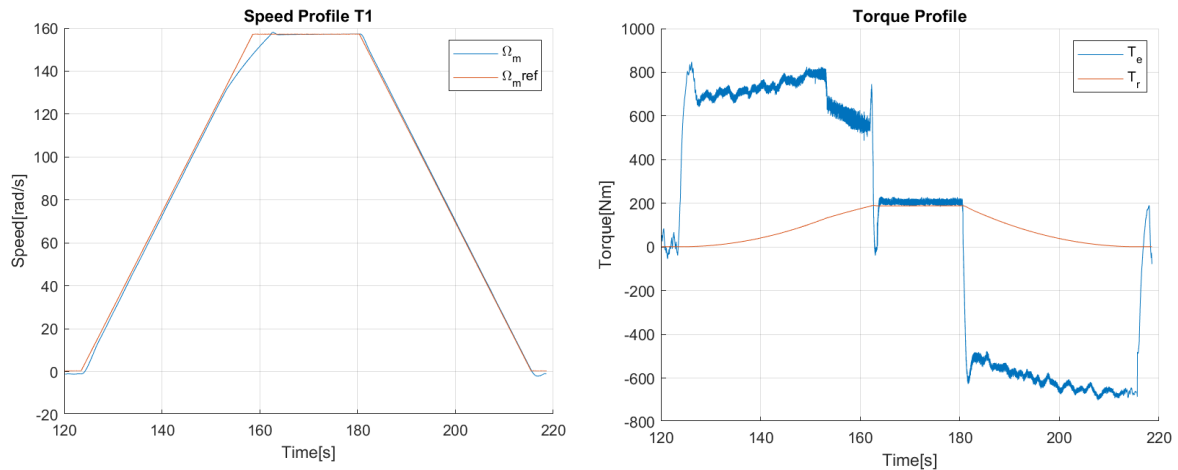


Figure 5.3-6 : Speed and Torque Profiles T1

In order to confirm the above consideration, it is necessary to observe the current profiles in Figure 5.3-7. During the acceleration and deceleration phases, the first winding has a fixed value of approximately 70[A] and 0[A] respectively, while the second winding fluctuates as the torque varies. During the coasting period, the current on the first winding remains constant at its maximum value, on the second winding it is practically zero. There are some current adjustments due to the change of configuration, but they are very limited and therefore the current profile is noticeably correct.

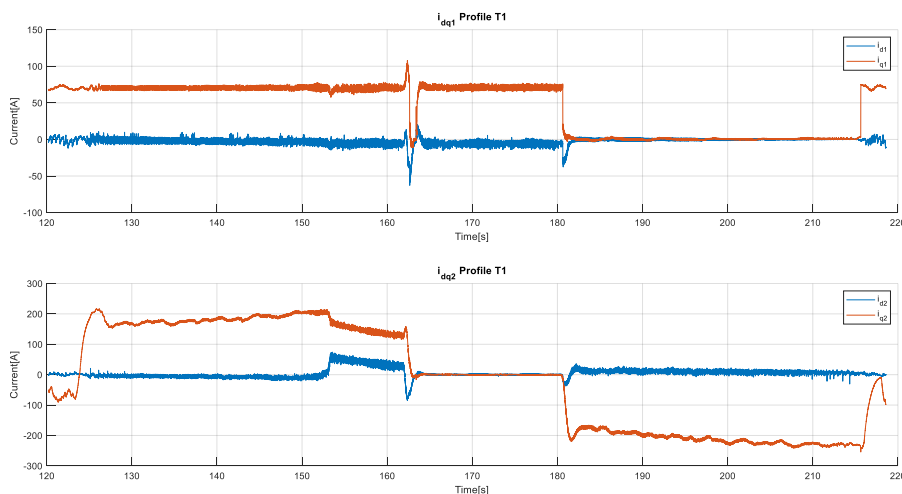


Figure 5.3-7 : Current Profile of both the Windings T1

We are now interested in the SOC profile of the battery. This can be seen in Figure 5.3-8. The initial value is 49.8%. After acceleration, it loses 1.3%, or approximately 440[Wh]. The value remains constant during the coasting period since we are in nominal conditions and the power required by the engine is the same as in FC. In the end, the SOC increases to 49.6% as a result of regenerative braking. It is crucial to note that during acceleration and deceleration, the power the battery can deliver is different from the power it can absorb. Since the battery can only be recharged by FCs or regenerative braking, the results look promising.

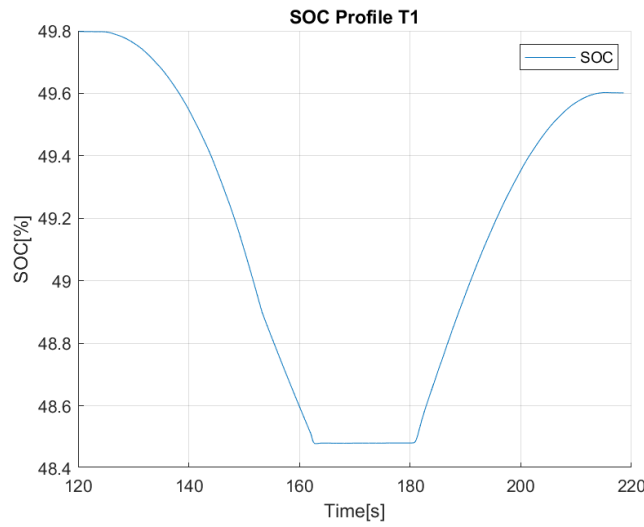


Figure 5.3-8 : SOC profile T1

### 5.3.2. Test 2(T2)

This second test was performed similarly to the first, but with one major difference: the initial SOC is below the set limit. Since it starts at 19%, the batteries cannot be used during the ride. What happens is that the FCs push as much power as possible. In fact, the electromagnetic torque during acceleration is approximately constant at 200[Nm], the resistant torque on the other hand follows the Davis equation, therefore the motor should initially accelerate at approximately  $1.3 \left[ \frac{rad}{s^2} \right]$  (the maximum is about  $4 \left[ \frac{rad}{s^2} \right]$ ) and then decrease as the resistant torque increases. Since FCs are sized to perform the nominal resistant torque, the speed will increase to the nominal value, but it will take about 400[s], which is too long. This condition should only be used if something has gone wrong.

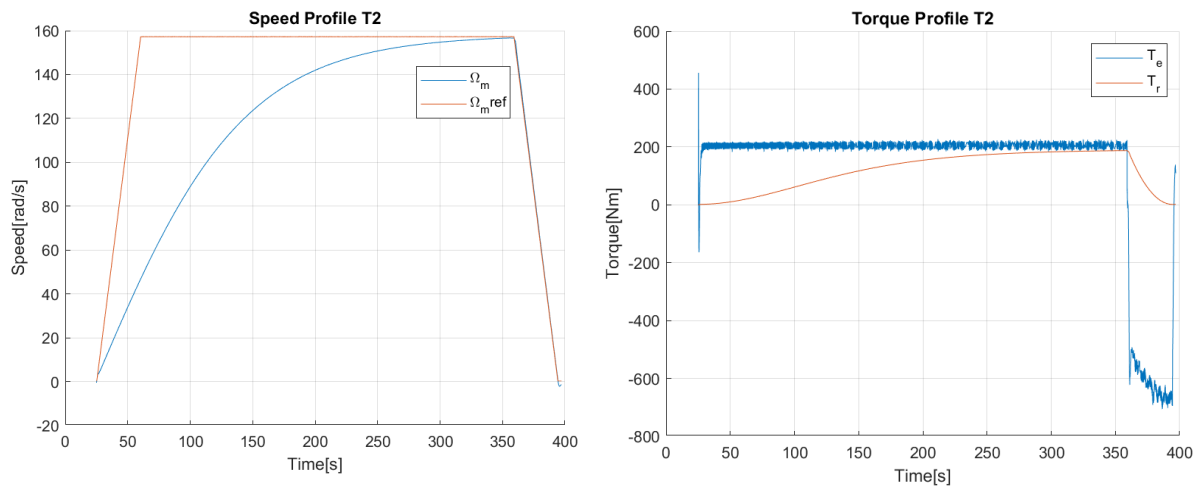


Figure 5.3-9 : Speed and Torque Profiles T2

The current profiles in Figure 5.3-10 show that the first winding works at the rated current all the time. In contrast, in the deceleration phase, the second winding is the only one to absorb power and interrupt the train in the desired time.

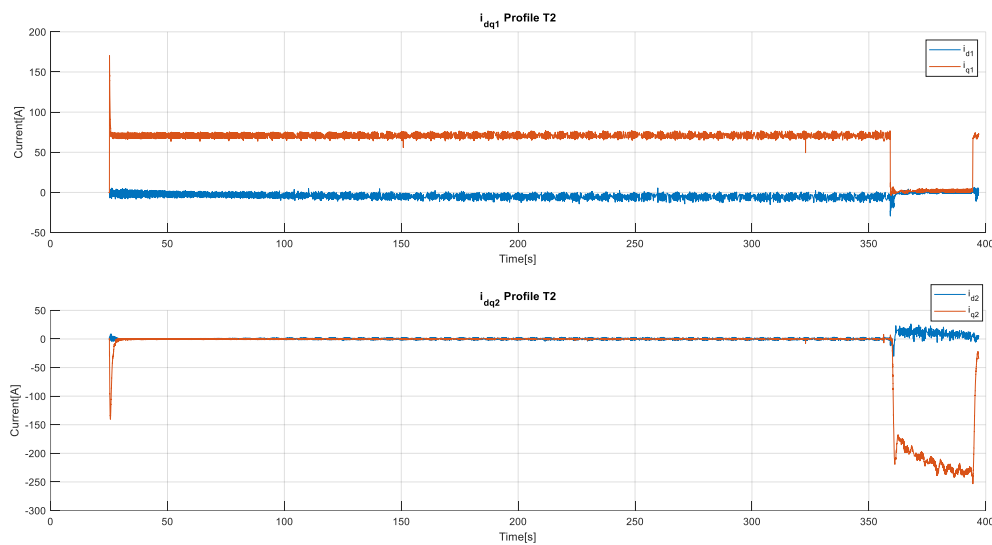


Figure 5.3-10 : Currents Profile T2

Figure 5.3-11 shows the amount of charge the batteries can achieve. In reality, it works as expected. The batteries are not able to provide energy during acceleration (before 400[s]), but the SOC increases slightly as they can absorb a very low amount of energy. In contrast, during regenerative braking, the SOC increases by about 1.2%, which corresponds to test 1.

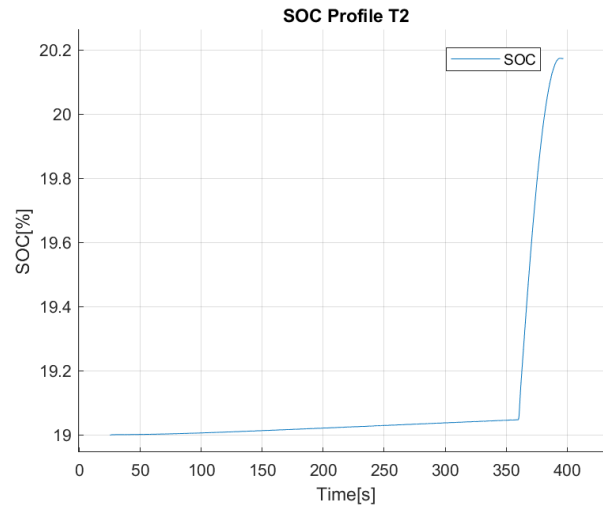


Figure 5.3-11 : SOC Profile T2

### 5.3.3. Test 3(T3)

In this last test, we try to analyse how much power FCs can send to the battery to recharge it. For this reason, the useful condition to force this process is to run the motor at a very low speed, with an initial SOC of less than 20%. Figure 5.3-12 shows the speed and torque profile of this test. We set the reference speed at  $10 \left[ \frac{\text{rad}}{\text{s}} \right]$ , the actual speed is a little higher as there is a threshold limit for omega. As for the torque, we can see that it is not constant but oscillates (with a peak respect to the nominal torque which means about 5% of error) around the resistant torque. The peak-to-peak value is about  $50[\text{Nm}]$ , that is about 7% of the rated torque  $T_n = 750[\text{Nm}]$ . The oscillation frequency equals equal to the motor speed. In fact, the electrical frequency of oscillation is approximately  $3.22[\text{Hz}]$ , while the mechanical one is about  $\frac{10 \left[ \frac{\text{rad}}{\text{s}} \right]}{2 * \pi} \approx 1.59[\text{Hz}]$  which multiplied by the number of poles  $n_p$  becomes strictly similar to the electrical parameters.



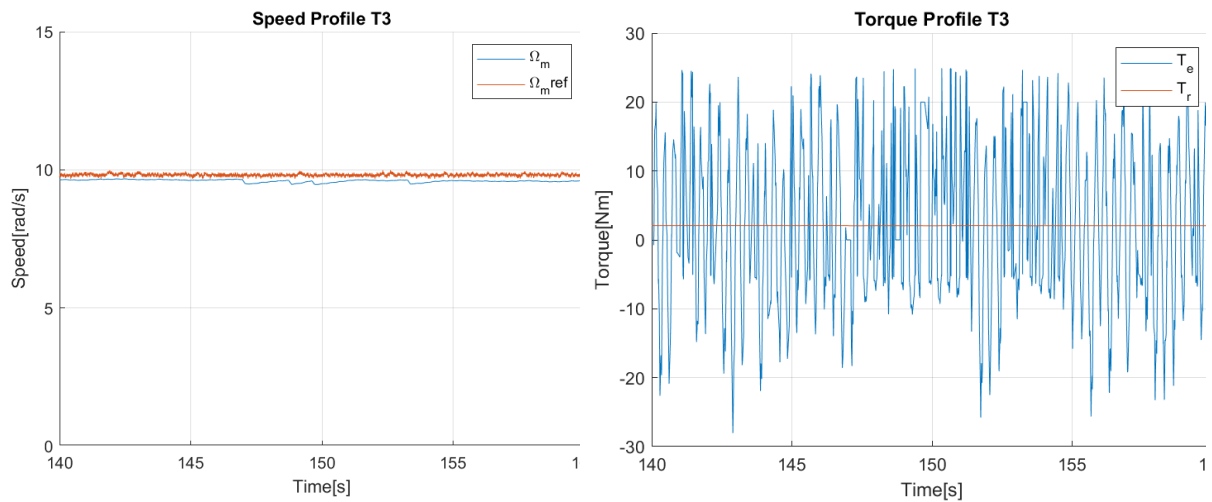


Figure 5.3-12 : Speed and Torque Profiles T3

As for the currents in Figure 5.3-13, they are as expected, the direct currents of both are approximately zero but the quadrature have the same modulus with opposite sign. In reality, the current on the first winding is a little higher because it has to push the rotor to overcome the resistive torque, and since the current on the second winding is decided according to the torque requirements, it is not perfectly opposite the current on the first winding.

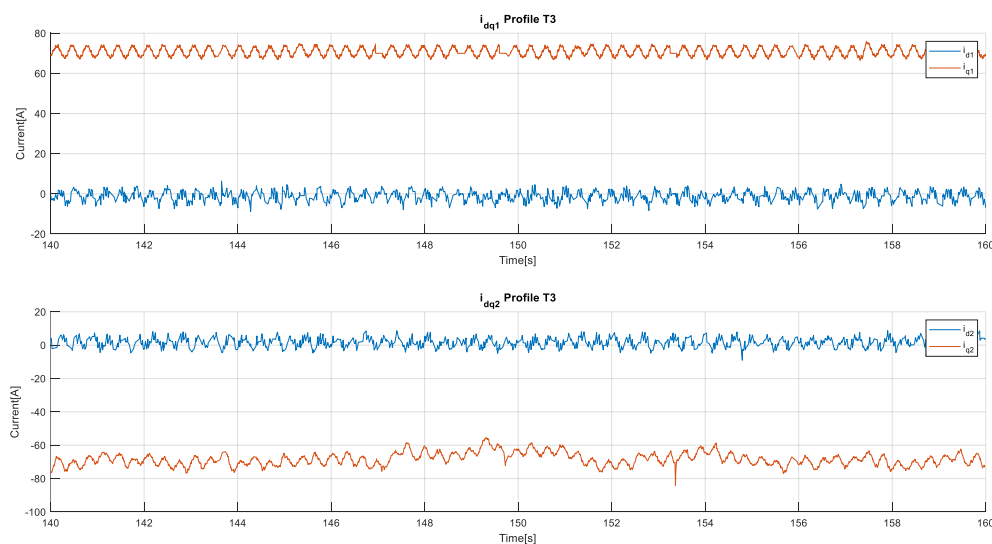


Figure 5.3-13 : Currents Profile T3

We want to know how much energy was restored from the fuel cell in this test. Figure 5.3-14 shows the SOC profile. It increases of 0.02% in about 20[s], which means about 1% in fifteen minutes. This shows that this method of recharging batteries is not very efficient, whereas the most efficient way is the recharging during the braking of the

train. Anyway, since the batteries are not designed to be charged via the electrical grid, any possible recharging method is useful.

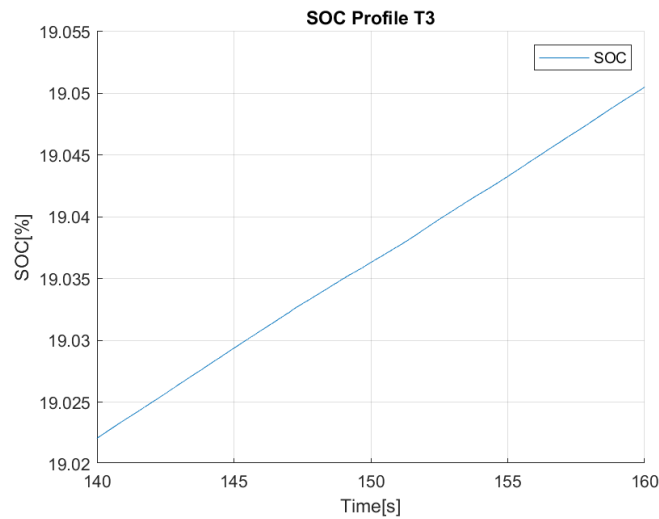


Figure 5.3-14 : SOC Profile T3

In summary, the logic scheme and FOC work well together, there is margin for improvement in performance, but we have achieved some promising results. The logic scheme is one of the key points of the project, so it might be interesting in future developments to look for a more complex logic with a different balance of battery usage, and FCs. We have however achieved our main goal; we have created a complete configuration that works under different conditions and can control the train with adequate efficiency. After these steps, we can move on to the actual test, in which we will realise a complete train journey.

## 6 Experimental Data of the Complete Setup

This chapter focuses mainly on the route described in section 1.3. It is necessary to remember that the route is divided into stations, and during the journey both the speed limit and the gradient of the terrain change, and consequently the resistant torque. For this reason, it will be interesting to understand whether the train can run as planned.

### 6.1. Gradient Contribution

Figure 6.1-1 show how the gradient vary during the path in function of the distance and the relative contribution to the toque. The formula to calculate the torque derives from the resistance force.

$$R_{grad}[N] = m_m * g * grad \quad (\text{Eq. 6.1-1})$$

$$T_{grad}[Nm] = R_{grad} * \frac{d_w/2[m]}{g_r}$$

Where *grad* is the slope in ‰.

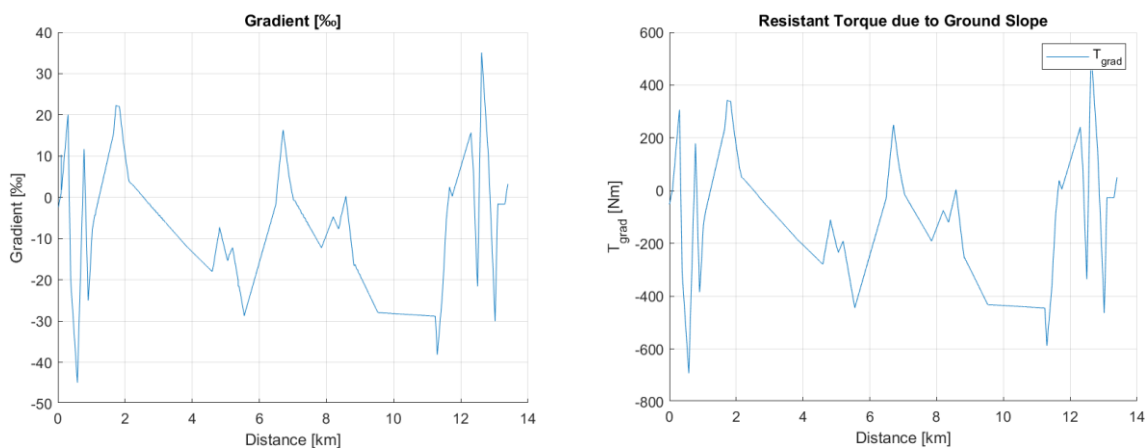


Figure 6.1-1 : Gradient profile of the Path and Related Resistant Torque

The simulation carried out considers only one engine modelled to represent the entire train. In this way, what happens to the engine can be translated to the train with a very

high degree of accuracy. This last chapter will show the speed and torque profile and focus on the issues raised in the previous sections.

## 6.2. PI Tuning

As far as the setting of the PIs controllers is concerned, we will refer to the same parameters as in the previous chapter. In fact, in chapter 5 we tried to find the best possible balance in terms of tuning with the logical scheme.

With respect to the tests in Chapter 5, the operating conditions change, since here the ground slope is taken into account. This implies that there are time intervals when the train will experience an increase in resistant torque due to the positive slope and therefore the logical scheme will take action to maintain the target speed, on the contrary, when the slope is negative, the train will tend to accelerate. Under these conditions, the use of the logic scheme is crucial to obtain a speed profile that is in accordance with the desired one. Since the slopes are very pronounced, the logic scheme will have to intervene to counteract them. In the next chapter, we will observe all the parameters involved in order to obtain the desired results.

## 6.3. Explanation of the Experimental Data

The route consists of five stations and in the simulation the train travels from St. Erth to St. Ives and come back to the initial station. During the journey, the distance travelled is 13.4[km]. The train must comply with the imposed speed limits. In addition, the resistant torque considers the Davis equation with the slope of the terrain. The speed profiles in Figure 6.3-1 represent the reference speed  $v_{mref}$  and the actual speed of the train  $v_m$ . During the acceleration and deceleration phases, the actual one follows the reference with a high degree of accuracy, but in some time intervals, a shift between the two occurs. This is due to the fact that there are many time intervals where the resistant torque exceeds the nominal one ( $T_{rn} = 200[Nm]$ ), but the only intervals where there might be a problem occur in the acceleration phases after Lelant and St. Ives. In these phases the acceleration is lower than expected. To understand why this happens, we need to examine the torque profile.

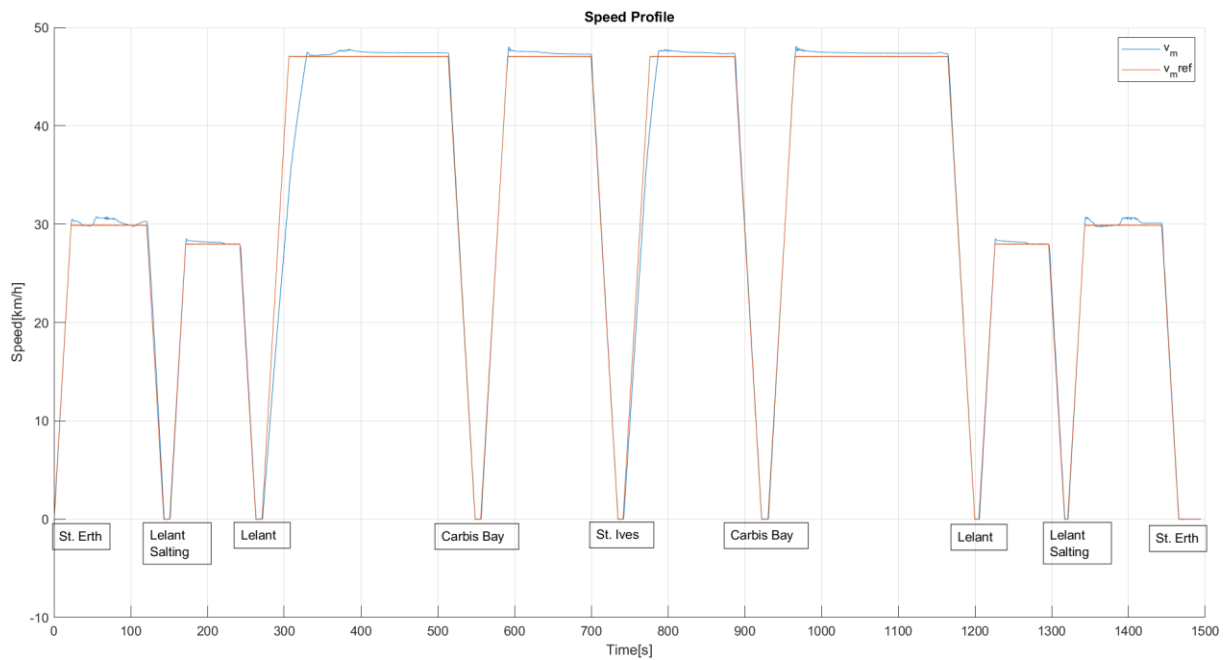


Figure 6.3-1 : Speed Profile

To analyse the torque profile, it is required to understand the contribution of the slope into the Davis equation. In particular, it is necessary to separate the contribution without and with the slope. For this reason, Figure 6.3-2 shows how it varies. In the graph, at the top we find the total profile, in the middle we find the already seen behaviour without slope, at the bottom how  $T_{grad}$  varies over time in function of the gradient. The middle one considers the resistance due to friction with the air and between wheels and rails. This resistance ranges from  $0[Nm]$  to around  $188[Nm]$ . On the other hand, the resistance due to the gradient has a very significant contribution. Its value varies drastically and, in some points, sharply. This slope behaviour makes the work more onerous as the conditions are difficult for a light train. For these reasons, in the study of the control, the gradient plays a very important role.

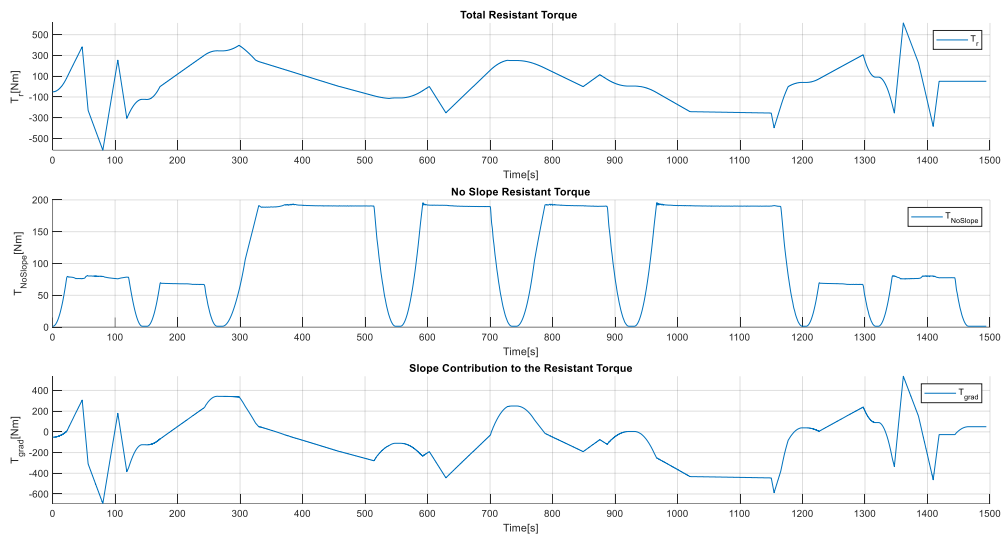


Figure 6.3-2 : Various Contribution to the Total Resistant Torque

As just said, by comparing the velocity and torque profiles (Figure 6.3-3), there are time intervals in which the resistant torque is higher than the nominal resistant one due to the gradient. For example, after Lelant at about 270[s], the  $T_{grad}$  gives the major contribution to the torque resistant since the speed is near zero and during the acceleration it starts at about 270[Nm] and goes up to 400[Nm], in other words, if the engine pushes with full power, the acceleration which could be achieved is  $a = \frac{850[Nm] - 400[Nm]}{147.135[kgm^2]} \approx 3.05 \left[ \frac{rad}{s^2} \right] \approx 0.25 \left[ \frac{m}{s^2} \right]$ , which means about 60% of the nominal one (this value can be calculated by the speed profile directly). Since the resistant torque changes and it is not always constant to 400[Nm], the represented case is the worst one. It also happens after St. Ives, but with minor effect.

In the torque profile, the acceleration and deceleration time intervals are evident. In fact, in these time intervals, the electromagnetic torque is higher or lower than the resistant torque. The maximum torque is not always reached since the resistant torque participates in both the acceleration and braking of the train. Furthermore, in the coasting phases, the resistant torque is followed by the electromagnetic torque to a good approximation.

There are some spots where the torque has steps such as the period between 360[s] – 380[s] and 780[s] – 800[s]. To understand why this occurs, we have to analyse the currents.

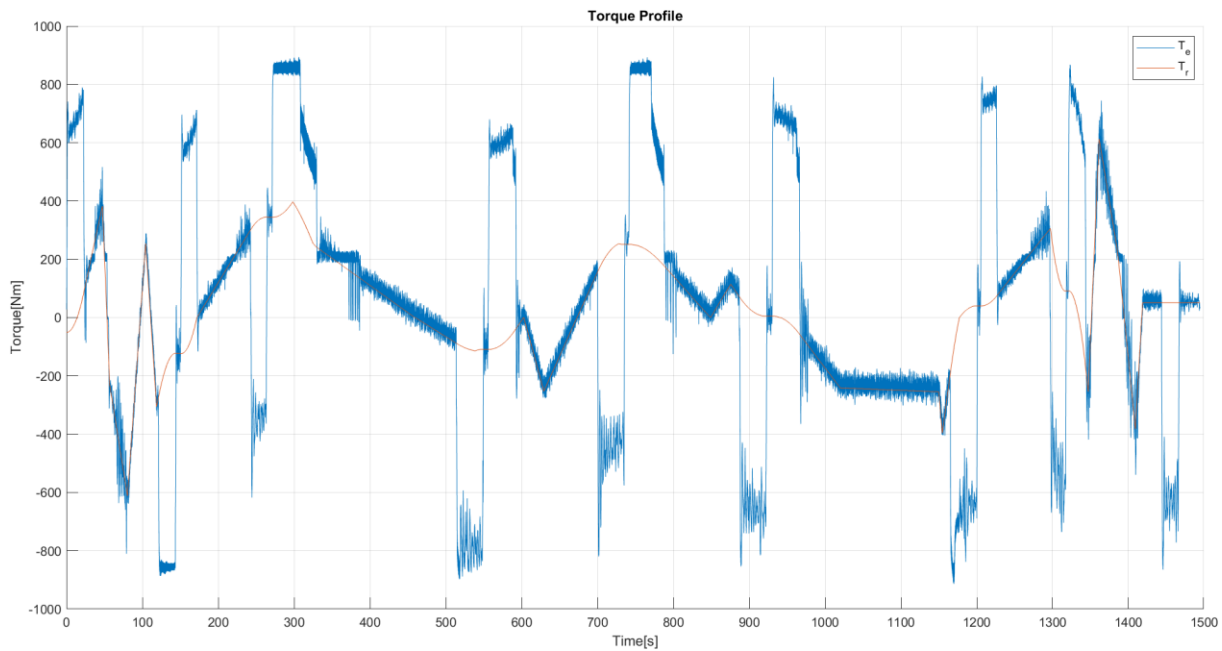


Figure 6.3-3 : Torque Profile

Figure 6.3-4 and Figure 6.3-5 show the behavior of the first and second winding currents respectively. The two quadrature currents, as well known, are different because they have a complementary function. What is interesting to note is that in the first winding, the current has two main values, in other words, it is mostly 70[A] but with some cases where it becomes zero due to the deceleration phases.

During the journey, the acceleration and deceleration time intervals alternate with coasting in which the speed must be kept constant. The slopes of the terrain are very sharp, and these conditions make controlling the train more complex. For this reason, we can see at certain times that there are limited torque steps between 0 and 200[Nm]. They occur mainly when the acceleration phase switches to coasting mode, as happens between 360[s]-380[s] and 780[s]-800[s]. This series of steps is controlled by the logic diagram which corrects the current on the first winding due to the switch of the configuration. To limit the effect of these oscillations, the hysteresis control on the logic scheme on the second winding was made more aggressive. Thanks to this, it was possible to reduce the oscillations to a limited time interval. The result obtained is shown in the current plots. However, accuracy on speed was lost.

The current on the first winding has mainly two constant values and its torque contribution will be proportional to these values. Consequently, during coasting time intervals, the second winding will have the function of supplying the torque required to obtain a total torque equal to the resistant torque, absorbing all slope differences.

As regards the direct currents, they should be zero. In reality, as seen in the previous chapters, this does not happen, or rather, they do not have a constant value and equal

to zero but oscillate with the same frequency imposed by the motor speed. This can be seen in the current of both windings. During some rapid changes in electromagnetic torque, direct currents are created with a net value opposite to those in quadrature. The reason lies in the fact that the direct currents generate a resistant torque effect that counteracts the motor torque we want to impose.

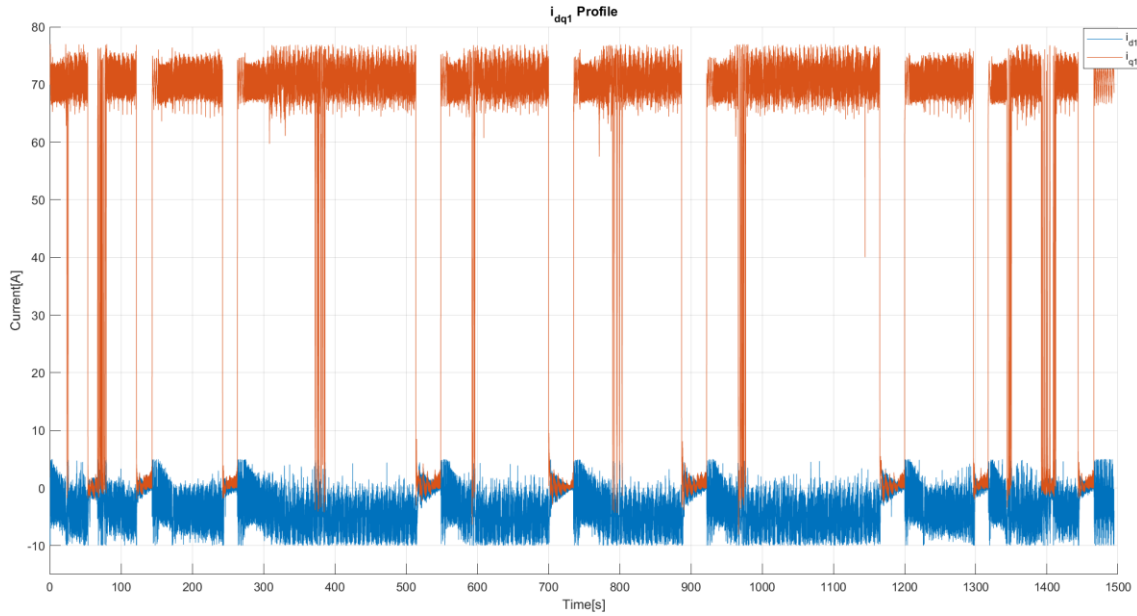


Figure 6.3-4 : Currents profile of First Winding

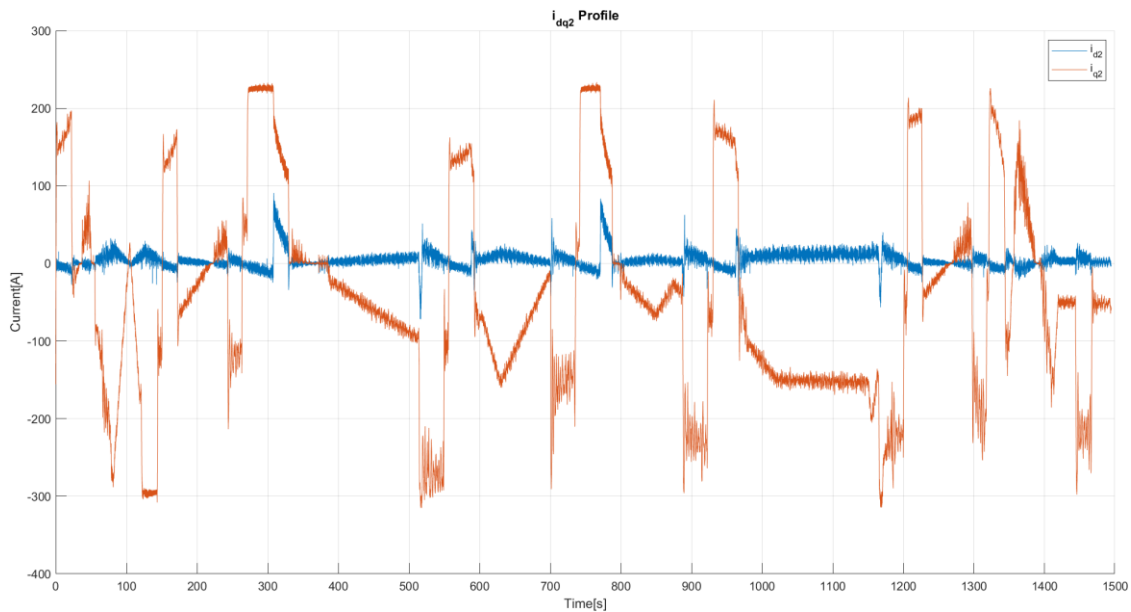


Figure 6.3-5 : Currents profile of Second Winding



Figure 6.3-6 shows the SOC profile of the batteries. It starts at 50% that is in the normal operating condition for the logic diagram, which means that the batteries are used during acceleration and recharged by the fuel cells or regenerative braking. The latter contribution is the most significant. In Section 5.3.1, we observed that during acceleration, the batteries consume 1.3% of their energy, while during braking they recover about 1%. However, there are certain conditions due to the gradient that make energy recovery much more profitable. We are referring that there are many sections where the slope is negative and the current of the first winding is maximum. Due to these two factors, if we look at the current profile of the second winding, we realise that most of the time the current is negative, in other words, the batteries absorb energy. This property of the track is interesting since it may allow us to change the logic scheme in the future and increase battery utilisation.

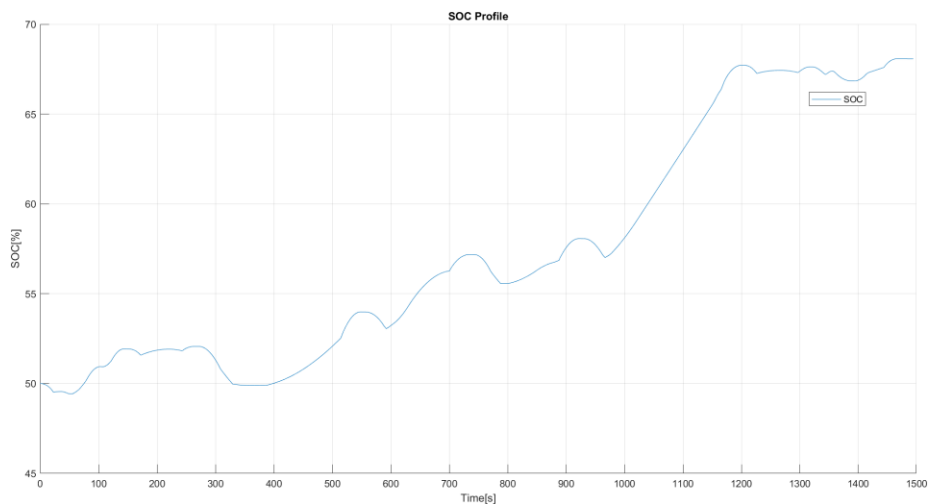


Figure 6.3-6 : SOC Profile of the Batteries

The distance travelled profile during one journey is plotted in Figure 6.3-7.

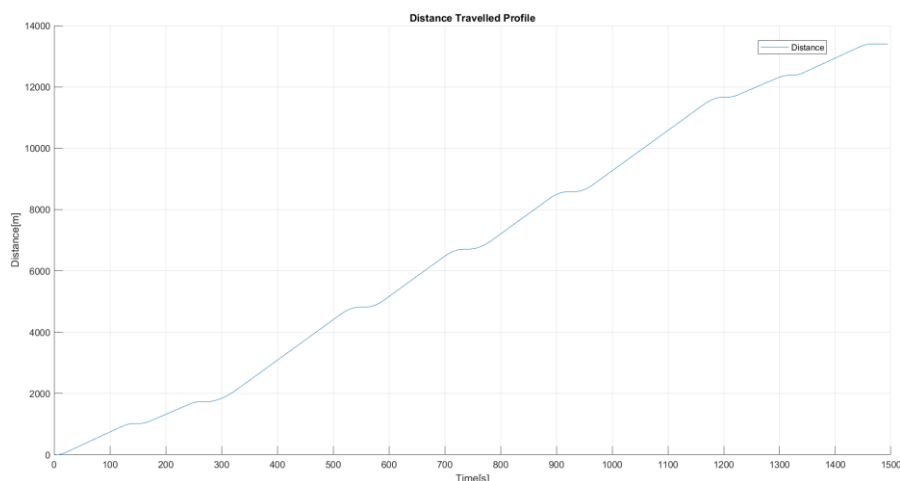


Figure 6.3-7 : Distance Profile of the Train

The last parameter to be checked is the power output of the two windings. The importance lies in the fact that these two powers have been dimensioned for an operating condition in which the FCs are to be used as the main source and the batteries as support. We can see in Figure 6.3-8 that the power of the first winding ( $P_1$ ) reaches 31.4 [kW] as an average value net of oscillations. The power of the batteries ( $P_2$ ), on the other hand, in acceleration does not exceed 75 [kW], in regeneration it reaches peaks of 130 [kW] as expected confirming the sizing of the power supplies.

These powers are calculated by:

$$P_T = T_e * \Omega_m$$

$$P_1 = \frac{3}{2} n_p \psi_{PM} i_{q1} \quad (\text{Eq. 6.3-1})$$

$$P_2 = \frac{3}{2} n_p \psi_{PM} i_{q2}$$

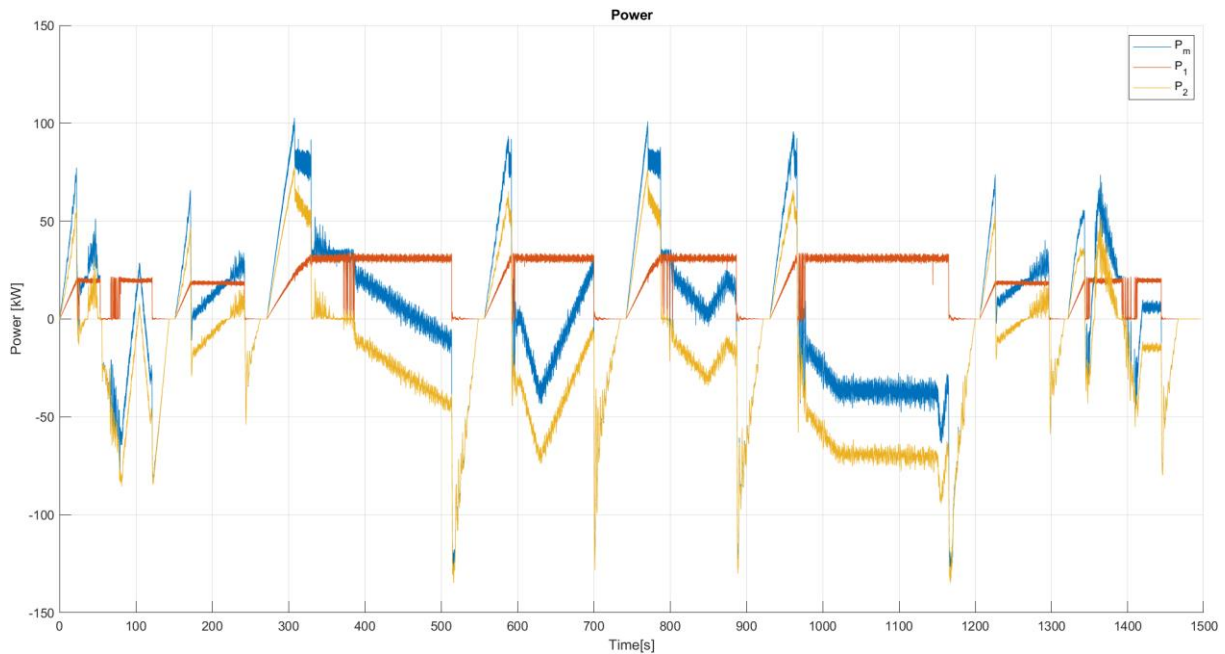


Figure 6.3-8 : Power Profiles

## 7 Conclusion and Future Updates

The project presented in this thesis consists of multiple parts. What we did in order to study it was to break it down into multiple parts and study its effects at each step thus being aware of all possible critical but also strong aspects of the project. The part we mainly focused on was the use of the hardware-in-the-loop technique associated directly with the microcontroller. We saw whether the microcontroller met our requirements by first testing it on single-phase loads and then on three-phase loads. This allowed us to define the points of greatest interest. After these initial steps, we have described and analyzed the main part that enables us to achieve what we want, we are talking about the permanent magnet synchronous motor in a dual three-phase configuration. There are a few aspects of this motor to consider. The first concerns synchronism, in fact it is necessary for the angle of the motor and the angle used in the microcontroller to be equal to obtain useful active power for operation by using the Clarke-Park transformation. Another fundamental aspect, however, is that being double three-phase allows two different electrical sources to be used as if they were two separate circuits. This implies that the standard electrical configuration of the trains used so far can be completely altered by allowing the use of separate sources. The aim of this setup is to encourage decarbonization. Accordingly, hydrogen fuel cells and batteries have been chosen as sources. The first as the main source, the second as an auxiliary to the fuel cells. The fuel cells are sized to move the train under nominal conditions. In this way, the train can reach the limit speed but in a prolonged time. The batteries provide increased power by helping the fuel cells to drastically reduce the time during acceleration and deceleration. To control the fuel cells and batteries, a logic control scheme was therefore created which, working closely with a FOC scheme, allows the required results to be achieved as seen in Chapter 6.

The required results have been excellently achieved. But they can be improved through the implementation of some algorithms and enhancements.

The first intervention could be done on the hardware. Some problems have arisen due to the lack of precision in reading the data. This is due to various factors such as the quantization of the ADCs in the microcontroller or even from different offsets in the Typhoon simulator. It is therefore advisable to implement automatic calibration systems for the ADCs where, through tests, they can be calibrated with the best possible accuracy.

A digression must be opened regarding the motor angle. In the design we have assumed that the angle is provided by the simulator directly, this does not happen in reality. We can choose for different solutions to obtain it. The first is by using a precision encoder or a hall effect sensor. However, there is another way, which consists of implementing a digital signal processing algorithm to estimate the angle and speed of the motor by reading the electrical parameters, such as the modulus and frequency of the currents, from which the motor speed can be derived. This approach has several advantages, but is difficult to implement on microcontrollers because it requires high performance and precision.

Another improvement can be made to the logic of power sharing. What we have noticed is that sometimes the configuration changes quickly due to threshold problems. This problem can be mitigated by introducing additional operating bands or through interlocks in the microcontroller logic functions.

Finally, there is one aspect we have not considered so far. This concerns the stresses on the engine. We know that the currents in the first winding are quite different from those in the second winding. This implies greater stress on the latter as it is subjected to temperature fluctuations. This can also affect the inverters. One possible solution to this problem is to mechanically exchange the windings after a certain period of time. It is possible to calculate the energy absorbed by the individual windings or the current in its RMS value and deduce from these calculations how often switch the windings.

In conclusion, the results obtained from the simulations are promising. We confirmed that the HIL technique can be used with good success to simulate an embedded system. Furthermore, it was possible to validate that the new setup can be used and further studied to be implemented in a real system. There are some aspects to be improved, but we are confident that this study can bring benefits in terms of the environment and the advancement of technology in the railway industry.





# Bibliography

- [1] Nursaid Polater, Pietro Tricoli, Stuart Hillmansen "Analysis, Development and Control of Fuel Cell Propulsion System for Light Railways"
- [2] [Online] [https://en.wikipedia.org/wiki/Hardware-in-the-loop\\_simulation](https://en.wikipedia.org/wiki/Hardware-in-the-loop_simulation)
- [3] [Online] [typhoon-hil.com](http://typhoon-hil.com)
- [4] [Online] [https://en.wikipedia.org/wiki/St\\_Ives\\_Bay\\_Line](https://en.wikipedia.org/wiki/St_Ives_Bay_Line)
- [5] Morris Brenna, Federica Foiadelli, Dario Zaninelli, Electrical Railway Transportation Systems, New Jersey: IEEE Press Wiley, 2018.
- [6] A. Vazquez-Blanco, C. Aguilar-Castillo, F. Canales-Abarca and J. Arau-Roffiel, "Two-Stage and Integrated Fuel Cell Power Conditioner: Performance Comparison," 2009 Twenty-Fourth Annual IEEE Applied Power Electronics Conference and Exposition, 2009, pp. 452-458, doi: 10.1109/APEC.2009.4802697.
- [7] H. S. Che and W. P. Hew, "Dual three-phase operation of single neutral symmetrical six-phase machine for improved performance," IECON 2015 - 41st Annual Conference of the IEEE Industrial Electronics Society, 2015, pp. 001176-001181, doi: 10.1109/IECON.2015.7392259.
- [8] R. H. Nelson and P. C. Krause, "Induction Machine Analysis for Arbitrary Displacement Between Multiple Winding Sets," IEEE Trans. Power Appar. Syst., vol. PAS-93, no. 3, pp. 841-848, 1974.
- [9] Francesco Castelli Dezza, "AC brushless", his notes from the course 2021-2022.
- [10] Paolo Bolzern, Riccardo Scattolini, Nicola Schiavoni, "Fondamenti di controlli automatici", McGraw Hill Education
- [11] Francesco Castelli Dezza, Calzoni Pietro, "Modellistica e progetto di regolatori pi e pid orientati allo sviluppo su microcontrollore"
- [12] [Online] Texas Instrument website [www.ti.com/](http://www.ti.com/)
- [13] Giovanni Maria Foglia, "Power Electronic", his notes from the course 2020-2021





# A Appendix A

$$T_1 = \begin{bmatrix} 1 & \cos\left(\frac{2\pi}{3}\right) & \cos\left(\frac{4\pi}{3}\right) & \cos\left(\frac{\pi}{6}\right) & \cos\left(\frac{5\pi}{6}\right) & \cos\left(\frac{3\pi}{2}\right) \\ \cos\left(\frac{4\pi}{3}\right) & 1 & \cos\left(\frac{2\pi}{3}\right) & \cos\left(\frac{3\pi}{2}\right) & \cos\left(\frac{\pi}{6}\right) & \cos\left(\frac{5\pi}{6}\right) \\ \cos\left(\frac{2\pi}{3}\right) & \cos\left(\frac{4\pi}{3}\right) & 1 & \cos\left(\frac{5\pi}{6}\right) & \cos\left(\frac{3\pi}{2}\right) & \cos\left(\frac{\pi}{6}\right) \\ \cos\left(\frac{\pi}{6}\right) & \cos\left(\frac{3\pi}{2}\right) & \cos\left(\frac{5\pi}{6}\right) & 1 & \cos\left(\frac{2\pi}{3}\right) & \cos\left(\frac{4\pi}{3}\right) \\ \cos\left(\frac{5\pi}{6}\right) & \cos\left(\frac{\pi}{6}\right) & \cos\left(\frac{3\pi}{2}\right) & \cos\left(\frac{4\pi}{3}\right) & 1 & \cos\left(\frac{2\pi}{3}\right) \\ \cos\left(\frac{3\pi}{2}\right) & \cos\left(\frac{5\pi}{6}\right) & \cos\left(\frac{\pi}{6}\right) & \cos\left(\frac{2\pi}{3}\right) & \cos\left(\frac{4\pi}{3}\right) & 1 \end{bmatrix} \quad \text{A.1}$$

$$T_2 = \begin{bmatrix} \cos 2\theta & \cos 2\left(\theta - \frac{\pi}{3}\right) & \cos 2\left(\theta + \frac{\pi}{3}\right) & \cos 2\left(\theta - \frac{\pi}{12}\right) & \cos 2\left(\theta - \frac{5\pi}{12}\right) & \cos 2\left(\theta + \frac{\pi}{4}\right) \\ \cos 2\left(\theta - \frac{\pi}{3}\right) & \cos 2\left(\theta + \frac{\pi}{3}\right) & \cos 2\theta & \cos 2\left(\theta - \frac{5\pi}{12}\right) & \cos 2\left(\theta + \frac{\pi}{4}\right) & \cos 2\left(\theta - \frac{\pi}{12}\right) \\ \cos 2\left(\theta + \frac{\pi}{3}\right) & \cos 2\theta & \cos 2\left(\theta - \frac{\pi}{3}\right) & \cos 2\left(\theta + \frac{\pi}{4}\right) & \cos 2\left(\theta - \frac{\pi}{12}\right) & \cos 2\left(\theta - \frac{5\pi}{12}\right) \\ \cos 2\left(\theta - \frac{\pi}{12}\right) & \cos 2\left(\theta - \frac{5\pi}{12}\right) & \cos 2\left(\theta + \frac{\pi}{4}\right) & \cos 2\left(\theta - \frac{\pi}{6}\right) & \cos 2\left(\theta - \frac{\pi}{2}\right) & \cos 2\left(\theta + \frac{\pi}{6}\right) \\ \cos 2\left(\theta - \frac{5\pi}{12}\right) & \cos 2\left(\theta + \frac{\pi}{4}\right) & \cos 2\left(\theta - \frac{\pi}{12}\right) & \cos 2\left(\theta - \frac{\pi}{2}\right) & \cos 2\left(\theta + \frac{\pi}{6}\right) & \cos 2\left(\theta - \frac{\pi}{6}\right) \\ \cos 2\left(\theta + \frac{\pi}{4}\right) & \cos 2\left(\theta - \frac{\pi}{12}\right) & \cos 2\left(\theta - \frac{5\pi}{12}\right) & \cos 2\left(\theta + \frac{\pi}{6}\right) & \cos 2\left(\theta - \frac{\pi}{6}\right) & \cos 2\left(\theta - \frac{\pi}{2}\right) \end{bmatrix} \quad \text{A.2}$$

### Clark and Park Transformation

The FOC diagram uses the d-q axes that are fixed with the rotor as references. Therefore, before the inverters and after the measurement of currents, it is necessary to convert the variables from  $dq$  to phase and vice versa. In this appendix, the calculation for the transformation used in the microcontroller will be shown, with an optimisation of the algorithm contained within it. Each conversion pass through the  $\alpha\beta$  reference

From  $X_{abc}$  to  $X_{dq}$ :

A.3

$abc \rightarrow \alpha\beta$

$$X_{\alpha} = (2X_a - X_b - X_c) * \frac{1}{3}$$

$$X_{\beta} = (X_b - X_c) * \frac{\sqrt{3}}{3}$$

$$X_z = (X_a + X_b + X_c) * \frac{1}{3}$$

$\alpha\beta \rightarrow dq$

$$X_d = X_{\alpha} \sin\theta_e - X_{\beta} \cos\theta_e$$

$$X_q = X_{\alpha} \cos\theta_e - X_{\beta} \sin\theta_e$$

From  $X_{dq}$  to  $X_{abc}$ :

A.4

$dq \rightarrow \alpha\beta$

$$X_{\alpha} = X_d \sin\theta_e + X_q \cos\theta_e$$

$$X_{\beta} = -X_d \cos\theta_e - X_q \sin\theta_e$$

$$X_z = 0$$

$\alpha\beta \rightarrow abc$

$$X_a = X_{\alpha} + X_z$$

$$X_b = -\frac{1}{2}X_{\alpha} + \frac{\sqrt{3}}{2}X_{\beta} + X_z$$

$$X_c = -\frac{1}{2}X_{\alpha} - \frac{\sqrt{3}}{2}X_{\beta} + X_z$$

## List of Figures

Figure 1.2-1 : Typhoon HIL dedicated hardware .....	6
Figure 1.2-2 : HIL TI uGrid Launchpad Interface [2] .....	7
Figure 1.2-3 : Complete Setup.....	7
Figure 1.3-1 : St Ives Bay Line branch [4] .....	8
Figure 2.1-1 : Self-Propelled Scheme for AC traction System [5] .....	12
Figure 2.1-2 : Basic diagram of a multi engine diesel locomotive [5] .....	13
Figure 2.1-3 : Diagram of Fuel Cell locomotive [5].....	13
Figure 2.1-4 : Standard configuration of a Hydrogen and Battery Supplied Train [1]	14
Figure 2.1-5 : New configuration proposed for traction vehicles using hydrogen FC and batteries .....	15
Figure 2.2-1 : Ragone chart for different storage technologies [5].....	17
Figure 2.2-2 : Hydrogen Fuel Cell working scheme [5] .....	18
Figure 2.2-3 : $v - i$ characteristic curve [3].....	19
Figure 2.2-4 : $v - Ah$ chart .....	20
Figure 2.3-1 : Stator winding arrangement for (a) asymmetrical six-phase, (b) symmetrical six-phase, and (c) dual three-phase machines. [7].....	21
Figure 2.3-2 : Disposition of the stator windings.....	22
Figure 2.3-3 : $d - q$ axes on the rotor and $\alpha - \beta$ axes on the stator respectively from winding $abc$ and $xyz$ .....	23
Figure 2.3-4 : Proposed system for each carriage [1].....	26
Figure 2.3-5 : Representation of a gradient.....	27
Figure 2.3-6 : Resistant Torque Profile .....	28
Figure 2.4-1 : Vector Diagram of the position for the voltage of the First Winding below the Base Speed (a) and at the Base Speed(b).....	31
Figure 2.4-2 : Operating region of DTPMSM for only one winding.....	32
Figure 2.4-3 : FOC scheme of a DTPMSM with a displacement of $30^\circ$ .....	33
Figure 2.5-1 : PI controller basic scheme .....	36

Figure 2.5-2 : General control scheme of a simple system [11] .....	36
Figure 2.5-3 : Considered scheme control [11] .....	37
Figure 2.5-4 : Integrator and Actuator .....	39
Figure 2.5-5 : Block scheme of the anti-windup system .....	39
Figure 2.6-1 : F28379D [13] .....	40
Figure 2.6-2 : Single Leg Inverter [13].....	41
Figure 2.6-3 : Fundamental and Carrier signals(up), PWM1A and PWM1B (middle), $v_{AO}$ and $v_{AO1}$ ( down) [13].....	42
Figure 2.6-4 : Up-Down count inside the PWM peripheral [12].....	43
Figure 2.6-5 : Duty Cycle [12] .....	43
Figure 2.6-6 : PWM signal (a) and Death Time of 2 $\mu$ s(b).....	44
Figure 2.6-7 : Sinusoidal waveform in Continuous Time(a) and in Discrete Time(b) after sampling .....	46
Figure 2.6-8 : Split $R/z$ .....	48
Figure 2.6-9 : Final configuration of PI with Anti-Windup.....	48
Figure 3.1-1 : Typhoon HIL Electric Scheme Single Leg Inverter .....	51
Figure 3.1-2 : Reference Signals Single Leg HIL vs SIM .....	52
Figure 3.1-3 : SIM Voltage on RL load.....	53
Figure 3.1-4 : Harmonics content in the SIM voltage.....	54
Figure 3.1-5 : Reference signal, first harmonic, first harmonic scaled and shifted .....	55
Figure 3.1-6 : Current in the load SIM and its harmonic content .....	56
Figure 3.1-7 : Voltage on the Load and its harmonic content HIL .....	57
Figure 3.1-8 : Reference Signals, First Harmonic and First Harmonic Scaled and Shifted .....	57
Figure 3.1-9 : Current on RL load and Harmonic content .....	58
Figure 3.2-1 : Three-phase Inverter with RL load .....	59
Figure 3.2-2 : Three legs for a three-phase inverter .....	59
Figure 3.2-3 : Three-phase Voltage SIM .....	59
Figure 3.2-4 : Filtered Voltage and Harmonic content SIM.....	60
Figure 3.2-5 : Three-phase Currents(a) and Their Harmonic Content(b).....	61
Figure 3.2-6 : Three-phase Voltage HIL .....	61

Figure 3.2-7 : Filtered Voltages Voltage(a) and Harmonic Contents(b) HIL .....	62
Figure 3.2-8 : Three-phase Currents(a) and Their Harmonic content (b).....	62
Figure 3.3-1 : Three-phase and Induction Machine Scheme .....	63
Figure 3.3-2 : Speed Profile for HIL and SIM modes.....	64
Figure 3.3-3 : Current in the Induction motor .....	65
Figure 3.3-4 : Harmonic Content of the Voltage compared from SIM and HIL modes .....	66
Figure 3.3-5 : Three-phase currents for SIM and HIL simulation .....	66
Figure 3.3-6 : Harmonic contents for Currents.....	67
Figure 4.1-1 : Test Setup of Three-phase PMSM .....	70
Figure 4.2-1 : Current Control for Three-phase PMSM.....	71
Figure 4.2-2 : Torque Profile(a) and Speed Profile(b).....	72
Figure 4.2-3 : Direct and Quadrature Currents Profile .....	72
Figure 4.2-4 : Overall Current(a) and Steady State Current(b).....	73
Figure 4.2-5 : Harmonic Content of the Steady State Current .....	74
Figure 4.3-1 : Block Scheme of DTPMSM Current Control .....	75
Figure 4.3-2 : Complete Setup of a DTPMSM.....	76
Figure 4.3-3 : Speed(a) and Torque(b) Profile DTPMSM with Algorithm 3 .....	77
Figure 4.3-4 : Focus on the Torque before 10[s] .....	78
Figure 4.3-5 : Direct and Quadrature Currents on the First (a) and Second (b) windings .....	79
Figure 4.4-1 : Speed Profile of the Simulation with the Speed Control .....	80
Figure 4.4-2 : Torque Profile in Speed Control.....	81
Figure 4.4-3 : Current Profile of the First(a) and Second(b) Windings .....	82
Figure 4.4-4 : Comparison between ACC and COAST mode .....	83
Figure 4.4-5 : Comparison of Torque for ACC and COAST mode .....	83
Figure 5.1-1 : Power Sharing Logical Diagram .....	87
Figure 5.2-1 : Electrical Scheme of the Fuel Cell in Typhoon HIL.....	88
Figure 5.2-2 : Electric Scheme of Batteries in Typhoon HIL.....	88
Figure 5.3-1 : Step and Ramp response of the Speed Controller .....	90
Figure 5.3-2 : Step Response of the Current Controllers.....	90

Figure 5.3-3 : Speed and Torque Profiles .....	91
Figure 5.3-4 : Step and Ramp Response of the Speed Controller .....	92
Figure 5.3-5 : Step Response of the Current Controllers.....	92
Figure 5.3-6 : Speed and Torque Profiles T1 .....	93
Figure 5.3-7 : Current Profile of both the Windings T1 .....	93
Figure 5.3-8 : SOC profile T1.....	94
Figure 5.3-9 : Speed and Torque Profiles T2.....	95
Figure 5.3-10 : Currents Profile T2 .....	95
Figure 5.3-11 :SOC Profile T2.....	96
Figure 5.3-12 : Speed and Torque Profiles T3.....	97
Figure 5.3-13 : Currents Profile T3 .....	97
Figure 5.3-14 : SOC Profile T3.....	98
Figure 6.1-1 : Gradient profile of the Path and Related Resistant Toque .....	99
Figure 6.3-1 : Speed Profile.....	101
Figure 6.3-2 : Various Contribution to the Total Resistant Torque .....	102
Figure 6.3-3 : Torque Profile.....	103
Figure 6.3-4 : Currents profile of First Winding.....	104
Figure 6.3-5 : Currents profile of Second Winding.....	104
Figure 6.3-6 : SOC Profile of the Batteries.....	105
Figure 6.3-7 : Distance Profile of the Train .....	105
Figure 6.3-8 : Power Profiles .....	106

## List of Tables

Table 1.3-1 : Position of stations of St. Ives Bay Line.....	9
Table 2.1-1 : Comparison between the two configurations [1] .....	15
Table 2.1-2 : Total Parameters of the comparison from Standard and Proposed Configurations .....	16
Table 2.3-1 : Motor Equation Symbols.....	22
Table 2.3-2 : Symbols of Inductances.....	23
Table 2.3-3 : Datasheet of the Proposed PM Machine .....	29
Table 5.1-1 : Configuration.....	86
Table 5.3-1 : Logic Scheme Tests .....	89





## List of Abbreviation

<b>Term</b>	<b>Description</b>
<i>PMSM</i>	Permanent magnet synchronous machine
DTPMSM	Dual-Three Phase Permanent Magnet Synchronous Machine
<i>FC</i>	Fuel Cell
<i>DC</i>	Direct Current
<i>AC</i>	Alternate Current
<i>HIL</i>	Hardware-In-the-Loop
<i>DE</i>	Diesel Engine
<i>HFC</i>	Hydrogen FC
<i>PEMFC</i>	Proton-Exchange Membrane Fuel Cell
<i>FOC</i>	Field Oriented Control
<i>FFT</i>	Fast Fourier Transform
<i>SIM</i>	Only PC simulation
<i>CC</i>	Current Control
<i>SC</i>	Speed Control
<i>SOC</i>	State of Charge

## List of Algorithms

Algorithm 1: PI with anti-windup .....	49
Algorithm 2 : Induction Motor Control .....	64
Algorithm 3 : Three-phase PMSM Current Control.....	71
Algorithm 4 : Three-phase PMSM Speed Control .....	80



## Acknowledgements

Vorrei ringraziare innanzitutto il relatore di questa tesi, il prof. Foglia, per la sua organizzazione, la sua professionalità e la sua pazienza.

Ringrazio il Dr. Tricoli per avermi permesso di sviluppare un suo progetto e con esso anche le persone che a Birmingham mi sono state vicine, Nursaid, Tabish e Jovan.

Vorrei ringraziare i miei compagni di studi e del gruppo "Delta di Dirac", avete reso gli anni di politecnico un po' meno difficili. Con essi anche i miei amici più cari di Longuelo che mi hanno incitato nel mio percorso.

Un sentito ringraziamento alla mia famiglia, ai miei genitori, le mie sorelle, mio nonno, mia zia, Luchino e Gaia per esserci sempre stati, aver supportato tutte le mie stranezze, e reso la persona che sono.

